

2009

# DYNAMIC MEASUREMENT OF THREE-DIMENSIONAL MOTION FROM SINGLE-PERSPECTIVE TWO-DIMENSIONAL RADIOGRAPHIC PROJECTIONS

Petar Seslija

Follow this and additional works at: <https://ir.lib.uwo.ca/digitizedtheses>

---

## Recommended Citation

Seslija, Petar, "DYNAMIC MEASUREMENT OF THREE-DIMENSIONAL MOTION FROM SINGLE-PERSPECTIVE TWO-DIMENSIONAL RADIOGRAPHIC PROJECTIONS" (2009). *Digitized Theses*. 3940.  
<https://ir.lib.uwo.ca/digitizedtheses/3940>

This Thesis is brought to you for free and open access by the Digitized Special Collections at Scholarship@Western. It has been accepted for inclusion in Digitized Theses by an authorized administrator of Scholarship@Western. For more information, please contact [wlsadmin@uwo.ca](mailto:wlsadmin@uwo.ca).

**DYNAMIC MEASUREMENT OF THREE-DIMENSIONAL MOTION FROM  
SINGLE-PERSPECTIVE TWO-DIMENSIONAL RADIOGRAPHIC  
PROJECTIONS**

(Spine Title: Dynamic Measurement of Motion from Single-Perspective Radiographs)

(Thesis format: Integrated-Article)

by

**Petar Seslija**

Biomedical Engineering Graduate Program

A thesis submitted in partial fulfillment  
of the requirements for the degree of  
**Master of Engineering Science**

School of Graduate and Postdoctoral Studies  
The University of Western Ontario  
London, Ontario, Canada

© Petar Seslija 2009

## Abstract

The digital evolution of the x-ray imaging modality has spurred the development of numerous clinical and research tools. This work focuses on the design, development, and validation of dynamic radiographic imaging and registration techniques to address two distinct medical applications: tracking during image-guided interventions, and the measurement of musculoskeletal joint kinematics.

Fluoroscopy is widely employed to provide intra-procedural image-guidance. However, its planar images provide limited information about the location of surgical tools and targets in three-dimensional space. To address this limitation, registration techniques, which extract three-dimensional tracking and image-guidance information from planar images, were developed and validated *in vitro*.

The ability to accurately measure joint kinematics *in vivo* is an important tool in studying both normal joint function and pathologies associated with injury and disease, however it still remains a clinical challenge. A technique to measure joint kinematics from single-perspective x-ray projections was developed and validated *in vitro*, using clinically available radiography equipment.

**Keywords:** x-ray imaging, registration, tracking, joint kinematics, dynamic measurement

## Co-authorship

Chapter 2 is an extended and modified version of the manuscript entitled "*Feasibility of three-dimensional tracking of surgical tools using two-dimensional single-plane x-ray projections*" co-authored by Petar Seslija, Damiaan F. Habets, Terry M. Peters and David W. Holdsworth, and published as a non-peer reviewed paper in Proc. SPIE 6918, 2008. Damiann F. Habets, another of David W. Holdsworth's graduate students, contributed the registration portion (3D-to-2D registration module) of the software implementation, and also provided valuable guidance and aide throughout. I was responsible for the reminder of the software implementation and integration of the contributed registration code, experimental design, image acquisition and processing, development of the visualization scripts, and manuscript preparation, all of which was supervised by both Terry M. Peters and David W. Holdsworth. All co-authors assisted in the editing of the manuscript.

Chapter 3, entitled "*Dynamic measurement of joint kinematics using single-perspective projections*", is in preparation for publication and is co-authored by Petar Seslija, Xunhua Yuan, Douglas D. Naudie, Robert B. Bourne, Steven J. MacDonald, Terry M. Peters and David W. Holdsworth. A portion of this work was presented at the

annual meeting of the Canadian Orthopaedic Research Society (CORS) in July 2009. Xunhua Yuan, a clinical collaborator at the Robarts Research Institute, assisted with all aspects of the study, including: the study concept, experimental design, image acquisition and processing. Douglas D. Naudie, Steven J. MacDonald and Robert B. Bourne, all orthopaedic surgeons at the London Health Sciences Centre, provided valuable support and guidance throughout. I was responsible for the experimental design, software implementation, image acquisition and processing, programming of the six-axis articulated robot, development of the visualization scripts, and manuscript preparation, all of which was supervised by both Terry M. Peters and David W. Holdsworth. All co-authors assisted in the editing of the manuscript.

## Dedication

This work is dedicated to everyone who has asked me any of the following questions over the past year:

*“ ... when are you going to be finished?”*

*“ ... have you graduated yet?”*

*“ ... are you done writing your thesis?”*

*... etc, etc, etc*

I now consider myself technically DONE, so you may all stop nagging me with these time-constrained questions. However, your genuine concern has been both motivating and endearing, for which I am greatly appreciative.

## Acknowledgements

I would like to express my sincere gratitude to the many people who have offered me their support and assistance throughout my academic endeavours at the Robarts Research Institute and The University of Western Ontario; without it this work would have not been possible.

First and foremost, I would like to thank my supervisors, David W. Holdsworth and Terry M. Peters, for providing me with the opportunity to pursue my research interests as a part of their labs. I feel very fortunate to have had two mentors who were so enthusiastic about my work. Their knowledge, on all subjects, and their approachability created an environment that was truly conducive towards research.

I would like to express my gratitude to both Maria Drangova and Xunhua Yuan, for all their help and guidance. Maria Drangova, whose office was just around the corner from my desk, was always available to answer my many questions and provide me with helpful advice. Xunhua Yuan, a co-author and collaborator, provided me with vital guidance and motivation, and was a pleasure to work with and learn from.

To both the Holdsworth and Peters lab groups: thank-you for all the insightful and interesting discussions, both research-related and otherwise. I am particularly indebted to Hristo Nikolov, Chris Norley, Steve Pollmann, Joseph Umoh, Chris Wedlake, John Moore, Jaques Milner, and Usaf Aladi for their technical assistance.

I would like to acknowledge all the financial support provided by The University of Western Ontario, the Ontario government, the Canadian Institutes of Health Research (Strategic Training Program and Operating Grants #77964 & #89852), and the London Health Sciences Centre that enabled this work.

To the friends I have made over these past several years during my studies, especially Chris D'Esterre, Sam Oduneye, Sean Nestor, Brandon Disher, Cristian Linte, Kayley Ma, and Katherine Fay: a heartfelt thanks for sharing both the stresses and joys of graduate student life with me. Your friendship has made my graduate experience all the more memorable and fulfilling.

Finally, I would like to thank my family, who were there for me throughout it all. Their continued support and encouragement were essential.

# Table of Contents

CERTIFICATE OF EXAMINATION .....	ii
Abstract.....	iii
Co-authorship .....	iv
Dedication.....	vi
Acknowledgements.....	vii
Table of Contents.....	ix
List of Tables .....	xii
List of Figures.....	xiii
List of Abbreviations .....	xix
 1 Introduction.....	 1
1.1 Tracking in Image-guided Interventions .....	2
1.1.1 Optical Tracking .....	2
1.1.2 Electromagnetic Tracking.....	5
1.1.3 Tracking via Medical Imaging Modalities.....	7
1.2 Techniques to Measure Joint Kinematics .....	10
1.2.1 Gait Analysis .....	10
1.2.2 Intracortical Pin Fixation .....	11
1.2.3 Magnetic Resonance Imaging.....	12
1.2.4 Computed Tomography .....	14
1.2.5 Radiostereometric Analysis .....	15
1.2.6 Biplane Radiography .....	18

1.2.7	Single-plane Radiography .....	20
1.3	Digital Radiography and Perspective X-ray Systems.....	24
1.3.1	X-ray Image Intensifiers .....	24
1.3.2	Flat Panel Detectors .....	28
1.3.3	Geometry of the Perspective Radiography System .....	31
1.3.4	Determination of Projective Parameters .....	32
1.4	Thesis Proposal .....	35
1.5	Thesis Outline .....	36
1.6	References.....	37
2	Tracking of Sparse Objects from Single-perspective Projections towards Image-guided Applications .....	47
2.1	Introduction.....	47
2.2	Methods .....	50
2.2.1	Overview of the projection-Procrustes Registration.....	50
2.2.2	Algorithm Overview .....	53
2.2.3	Phantoms.....	65
2.2.5	Assessment of Accuracy and Precision .....	66
2.2.6	Dynamic Tracking Assessment .....	70
2.2.7	Visualization .....	72
2.3	Results.....	74
2.3.1	Accuracy and Precision Assessment .....	74
2.3.2	Dynamic Tracking Assessment .....	78
2.3.3	Algorithm Performance .....	78
2.3.4	Visualization .....	79
2.4	Discussion.....	83
2.5	Conclusions.....	89
2.6	References.....	90
3	Dynamic Measurement of Joint Kinematics using Single-perspective Projections.....	94
3.1	Introduction.....	94
3.2	Methods .....	97
3.2.1	Measurement of Kinematics from Single-perspective Projections.....	97

3.2.2	Anatomical Model .....	98
3.2.3	Imaging Equipment .....	99
3.2.4	Static Assessment of Bias and Precision .....	99
3.2.5	Dynamic Assessment of Bias, Precision and Repeatability .....	101
3.2.6	Registration of CT Data to Kinematic Measurements.....	105
3.2.7	Measurement of Effective Dose .....	106
3.3	Results.....	108
3.3.1	Static Assessment of Accuracy and Precision .....	108
3.3.2	Dynamic Assessment of Accuracy and Precision.....	109
3.3.3	Repeatability of Kinematic Measurements.....	110
3.3.4	Registration of CT Data to Kinematic Measurements.....	114
3.3.5	Measurement of Effective Dose .....	115
3.4	Discussion.....	116
3.5	Conclusions.....	124
3.6	References.....	125
4	Summary and Future Directions.....	130
4.1	Summary and Conclusions .....	130
4.1.1	Sparse Object Tracking towards Image-guided Interventions.....	130
4.1.2	Measurement of Joint Kinematics .....	132
4.2	Future Directions .....	135
4.2.1	Sparse Object Tracking towards Image-guided Interventions.....	135
4.2.2	Measurement of Joint Kinematics .....	137
4.3	References.....	141
	Curriculum Vitae.....	143

## List of Tables

<b>Table 2-1:</b> Employed values of empirically set variables listed within the equations of section §2.2.2 .....	79
<b>Table 3-1:</b> Results of static assessment of bias and precision. Errors are reported as the difference between the measured and applied motion in 6 degrees of freedom (i.e 3 translations, 3 rotations). Note, that translations in the z-direction ( $t_z$ ) occurred orthogonal to the imaging plane of the radiography system. ....	108
<b>Table 3-2:</b> Results of dynamic assessment of bias and precision. Errors are reported as the deviation of measured motion from zero in 6 degrees-of-freedom (i.e 3 translations, 3 rotations). Note, that translations in the z-direction ( $t_z$ ) occurred orthogonal to the imaging plane of the radiography system.....	109

## List of Figures

- Figure 1-1:** a) Active optical tracking system (OTS) consisting of position sensor, central control unit, and active tool (Northern Digital Polaris). b) Passive position sensor capable of both emitting and detecting infrared light (Northern Digital Vicra). c) Active instruments and reference frames containing infrared light emitting diodes. d) Passive instruments and reference frames containing retro-reflective spheres. .... 4
- Figure 1-2:** a) Electromagnetic tracking system (EMTS) consisting of field generator, central control unit, and tracked probe containing field sensor (Northern Digital Aurora). b) Miniature field sensors in six degree-of-freedom (top) and five degree-of-freedom (bottom) configurations. .... 6
- Figure 1-3:** Spatial reconstruction of 3D position of tantalum markers implanted into the skeleton using radiostereometric analysis (RSA). The 3D reconstructed position of each marker ( $m_i$ ) is determined by the intersection of the rays cast between the projections of each marker in the pair of stereo images ( $c_i$ ) and its respective x-ray focus. .... 16
- Figure 1-4:** The computation of absolute motion and relative motion of rigid body 2 to rigid body 1. Absolute motion of rigid body 1 is calculated by finding the transformation  $\mathcal{S}_a(x_i) = x_i' = [R_a]^T x_i + d_a$ , which describes the motion of rigid body 1 between times 1 and 2. The inverse of this movement is then used to transform the points in rigid body 2 at time 2 from the positions  $v_i$  to positions  $\mathcal{S}_a^{-1}(v_i) = v_i' = [R]_a^T v_i - [R]_a^T d_a$ . Finally, the relative motion between the two rigid bodies can be computed such that  $\mathcal{S}_r(u_i) = v_i'$ . Adapted from Söderkvist et al.<sup>86</sup> ..... 17
- Figure 1-5:** Model-based measurement of kinematics using biplane radiography. Digitally reconstructed radiographs (DRRs) are rendered using ray-casting techniques. The intensity values of the pixels,  $I_1$  and  $I_2$ , are determined by summation of the attenuation coefficients of the voxels within model along the ray path between pixels,  $I_1$  and  $I_2$ , and their corresponding x-ray focus. .... 19

- Figure 1-6:** Technique to estimate 3D pose of joint implanted with markers from a single-perspective projection. Makers implanted into the skeleton,  $m_i$ , are fit to the projection lines cast between the marker projections,  $c_i$ , and the x-ray focus using a 3D-to-2D registration algorithm. .... 22
- Figure 1-7:** Perspective projection of CAD surface geometry on single-plane radiography system. A digitally reconstructed radiography (DRR) is rendered using ray-casting techniques..... 23
- Figure 1-8:** (a) Imaging chain of a digital image intensifier radiography system; (b) internal structure of an image intensifier; (c) input screen of an image intensifier. Adapted from Bushberg et al.<sup>113</sup> ..... 26
- Figure 1-9:** (a) Cross-section of indirect detection flat panel; (b) cross-section of direct detection flat panel; (c) schematic diagram of an active-matrix array and electronics used to control readout. Each pixel element within the active-matrix consists of either a discrete photosensitive or capacitive detector, and a switch, usually a thin field transistor (TFT) or diode. Adapted from Bushberg et al.<sup>113</sup> and Beutel et al.<sup>112</sup> ..... 30
- Figure 1-10:** Central perspective projection of object point,  $P(x,y,z)$ , onto imaging plane,  $im(i,j)$ . The geometry of a radiography system can be described by the perspective centre (x-ray focus), the principle distance (source-to-detector distance), and the principle point,  $(i_o, j_o)$ , on the imaging plane (detector). Adapted from Mikhail et al.<sup>117</sup> ..... 32
- Figure 1-11:** A calibration cage is used to determine the photogrammetric projective paramaters of a persepective x-ray system. Calibration cages usually contain two radio-transulent plates embedded with radio-opaque markers. The fiducial plane is used to determine the direct linear transformation (DLT), which transforms 2D image points into the 3D object coordinate system. The control plane is used to determine the position of the x-ray focus..... 33
- Figure 2-1:** Coordinate systems defined in projection-Procrustes registration problem. The world coordinate system,  $xyz$ , in which the perspective geometry is defined, the image coordinate system,  $uv$ , describes the image space, and the object coordinate system,  $x'y'z'$ , describes the relative positions of each marker within the sparse object..... 51
- Figure 2-2:** Optimal alignment of sparse object marker with their corresponding projection lines. In an ideal situation, where no noise or geometric distortion is present and the locations of the marker projections upon the image can be measured without error, the minimal distance between each marker and its corresponding projection line is zero.  $\mathcal{Z}\{P_i'\} = [R]^T P_i' + t$ , is the transformation that relates the postion of the markers within the local object coordinate system,  $x'y'z'$ , to their position within the three-dimensional world coordinate system,  $xyz$ , after optimal alignment..... 53

<b>Figure 2-3:</b> Flow chart of algorithm for 3D tracking of sparse objects from 2D digital radiographs .....	54
<b>Figure 2-4:</b> Flow chart of marker identification and measurement module, and example images processed. ....	58
<b>Figure 2-5:</b> Phantoms manufactured for <i>in vitro</i> experiments: a) Grid phantom, manufactured from an acrylic plate, contains hemispherical divots; b) Stylus phantom, made to mimic function of a pointer tool. ....	66
<b>Figure 2-6:</b> Experimental setup for assessment of accuracy and precision: a) Siemens Multistar C-arm equipped with x-ray image intensifier (XRII) with phantoms inside field of view (FOV). b) Close-up of phantom setup within FOV of XRII. c) GE Innova 4100 C-arm with flat-panel (FP) detector with phantoms inside the FOV. d) Close-up of phantom setup within FOV of the FP detector.....	68
<b>Figure 2-7:</b> Assessment of accuracy and precision using an optical tracking system: a) Passive optical tracking frame rigidly attached to stylus phantom. b) Stylus phantom secured in a divot of the grid phantom. The location of the stylus is measured by the optical tracking system via the passive optical tracking frame attached to the stylus. ....	69
<b>Figure 2-8:</b> Setup of dynamic tracking experiment: a) localization of point targets within the skull phantom with tool tip of stylus phantom. b) Stylus phantom with rigidly attached passive optical tracking frame. Stylus was simultaneously tracked using the single-perspective projections, and optical tracking system.....	71
<b>Figure 2-9:</b> Summary of accuracy and precision assessment performed with the optical tracking system (OTS), and single-plane tracking using x-ray image-intensifier (XRII) and flat panel (FP), with image acquisition performed in both anterior-posterior (AP) and left anterior oblique (LAO) views. The results are reported in terms of measurements made inplane and out-of-plane. a) The root-mean-square (RMS) target registration error (TRE) of the registration between the measured tool tip locations and the known geometry of divots upon the grid phantom. b) The precision of repeated measurements made using each system. The precision was quantified using the standard deviation of repeated measurements of the location of the tool tip of the stylus. ....	75
<b>Figure 2-10:</b> Statistical analysis of accuracy assessment performed on the optical tracking system (OTS), and single-plane tracking using x-ray image-intensifier (XRII) and flat panel (FP), with image acquisition performed in both anterior-posterior (AP) and left-anterior-oblique (LAO) views. Accuracy was quantified using the target registration error (TRE) of the registration between the measured tool tip locations and the known geometry of divots upon the grid phantom. a) Inplane target registration	

error (TRE); b) Out-of-plane TRE. \* represents a statistically significant difference ( $p < 0.05$ ) when compared to the OTS..... 76

**Figure 2-11:** Statistical analysis of precision assessment performed on the optical tracking system (OTS), and single-plane tracking using x-ray image-intensifier (XRII) and flat panel (FP), with image acquisition performed in both anterior-posterior (AP) and left-anterior-oblique (LAO) views. Precision was quantified using the standard deviation of repeated measurements of the location of the tool tip of the stylus. a) Inplane precision; b) Out-of-plane precision. \* represents a statistically significant difference ( $p < 0.05$ ) when compared to the OTS..... 77

**Figure 2-12:** Assessment of dynamic tracking using optical tracking system (OTS) as standard reference to validate single-plane tracking using the flat panel (FP) detector. Comparison of the tool tip trajectory during the localization of targets within the skull phantom with the tool tip of stylus in: a) X translation, b) Y translation, c) Z translation. The root-mean-square (RMS) error is reported for each translational component. The RMS error was calculated using the differences between each curve at every frame..... 80

**Figure 2-13:** Snapshots of the 3D virtual environment at various camera angles, showing the projective geometry of the perspective x-ray system, respective positions of imaging plane and x-ray source, and position of skull phantom within the x-ray field of view. Several close-up views of the surface model of the skull phantom are also presented. .... 81

**Figure 2-14:** Two-dimensional projections acquired during dynamic tracking experiment (first row), and corresponding snapshots of the 3D virtual environment (second and third rows) during target localization. .... 82

**Figure 3-1:** a) The tibio-femoral knee model used for *in vitro* experiments. Eight tantalum markers, each 1 mm in diameter, were implanted into both the distal femur and proximal tibia of the knee model. b,c) Stereo projections acquired during radiostereometric analysis (RSA) examination used to determine relative locations of the markers..... 98

**Figure 3-2:** Experimental setup during static assessment. a) Micrometer-driven positioning stage, with knee model rigidly attached, setup inside field-of-view of radiography system. b) Sample medial-lateral projection of static phantom acquired during the static assessment. .... 100

**Figure 3-3:** Experimental setup during dynamic assessment. a) Six-axis articulated robot, with knee model rigidly attached, setup inside field-of-view of the radiography system. b) A sample medial-lateral projection of the dynamic phantom acquired during the dynamic assessment. .... 102

- Figure 3-4:** Sample frames acquired during the dynamic assessment and representative of the range of motion of one cycle of the dynamic phantoms programmed movement. .... 105
- Figure 3-5:** Experimental setup during measurement of effective dose. a) Ion chamber within field-of-view (FOV) of radiography system, and digital dosimeter used to measure entrance exposure. b) Sample projection acquired during dose measurements showing knee model and ion chamber. .... 107
- Figure 3-6:** Box and whisker plots representing the distribution of errors (i.e. difference between measured and applied motion) in 6 degrees-of-freedom, obtained from static assessment of accuracy and precision. Note, that translations in the z-direction ( $t_z$ ) occurred orthogonal to the imaging plane. .... 109
- Figure 3-7:** Box and whisker plots representing the distribution of errors (i.e. deviation of measured motion from zero) in 6 degrees-of-freedom, obtained from dynamic assessment of accuracy and precision. Note, that translations in the z-direction ( $t_z$ ) occurred orthogonal to the imaging plane. .... 110
- Figure 3-8:** Kinematics of the knee model during dynamic assessment performed to assess repeatability of measurements. The kinematics measured from all six trials are plotted within the same axes, and are expressed in 6 degrees-of-freedom (i.e. 3 translations and 3 rotations). Both translations and rotations are of the femur relative to the tibia. Translations are expressed as (a) Proximal/Distal ( $t_x$ ), (b) Anterior/Posterior ( $t_y$ ), and (c) Medial/Lateral ( $t_z$ ). Rotations are expressed as (d) Abduction/Adduction ( $R_x$ ), (e) Interior/Exterior ( $R_y$ ), and (f) Flexion/Extension ( $R_z$ ). Note, that translation in the Medial/Lateral direction, (c), occurred orthogonal to the imaging plane of the radiography system (out-of-plane). .... 112
- Figure 3-9:** Repeatability of kinematic measurements vs. the number of markers used within the rigid-body to perform 3D-to-2D registration. Repeatability is expressed along each degree of freedom (i.e. 3 translations and 3 rotations). Translations, (a), are expressed as Proximal/Distal (PD or  $t_x$ ), Anterior/Posterior (AP or  $t_y$ ), and Medial/Lateral (ML or  $t_z$ ). Rotations, (b), are expressed as Abduction/Adduction (ad/ab or  $R_x$ ), Interior/Exterior (int/ex or  $R_y$ ), and Flexion/Extension (flex/ext or  $R_z$ ). Note, that \* represents a statistically significant difference ( $p < 0.05$ ). .... 113
- Figure 3-10:** Registration of three-dimensional (3D) computed tomography (CT) data to two-dimensional (2D) projections. Visualization shows reconstructed position of x-ray source, imaging plane, knee joint (implanted with tantalum markers), and world frame of reference. .... 114
- Figure 3-11:** Registration of computed tomography (CT) data with kinematic measurements. First column shows projections acquired at 0° joint flexion a), and 55° joint flexion d). Second and third columns show the corresponding surface models of the femur and tibia segments, as registered

with the kinematic measurement to reconstruct relative position of the joint. Both the anterior view b), e), and the lateral view c), f) of the joint are shown at both flexion angles. .... 115

**Figure 4-1:** Several methods can be used to characterize the relative locations of the markers implanted into the joint, including: a radiostereometric analysis (RSA) examination, acquisition of a micro-computed tomography (microCT) scan, and acquisition of a clinical CT scan. a) and b) show stereo images of a knee phantom, implanted with tantalum markers, acquired during a RSA examination. c) and d) show maximum intensity projections (MIPs) of a micro-CT and CT scan, respectively of the same knee phantom. Note the bean-like shape of the markers within the CT volume (d); an image artefact due to the anisotropic voxel spacing of the CT volume. .... 138

## List of Abbreviations

2D	Two-dimensional
3D	Three-dimensional
AC	Alternating Current
A/D	Analog-to-Digital
ANOVA	Analysis of Variance
AP	Anterior-Posterior
BB	Ball Bearing
CAD	Computer Aided Design
CCD	Charged Coupled Devices
CT	Computed Tomography
DC	Direct Current
DLT	Direct Linear Transformation
DOF	Degrees-of-Freedom
DRR	Digitally Reconstructed Radiograph
EMTS	Electromagnetic Tracking System(s)
FOV	Field of View
FP	Flat-panel

fps	frames-per-second
FRE	Fiducial Registration Error
iCT	Interventional Computed Tomography
II	Image Intensifier
iMRI	Interventional MRI
IR	Infrared
IRE	Infrared Emitting Diodes
ISO	International Standards Organization
LAO	Left-Anterior-Oblique
LoG	Laplacian of a Gaussian
MRI	Magnetic Resonance Imaging
OTS	Optical Tracking System(s)
RMS	Root-Mean-Square
RSA	Radiostereometric Analysis
RSPA	Roentgen Single-Plane Analysis
SD	Standard Deviation
TC	Tungsten Carbide
TEE	Transesophageal Echocardiography
TRE	Target Registration Error
US	Ultrasound
XRII	X-ray Image Intensifier

# 1 Introduction

Since its inception in 1895 by Wilhelm Roentgen x-ray imaging has, and continues to be a staple of medical imaging. Today, x-ray imaging modalities are employed for a wide range of medical purposes, including: diagnosis, treatment and intervention, and monitoring of disease progression. X-ray imaging has typically been the front-line medical imaging modality in the clinic for diagnosis, and monitoring of musculoskeletal disease and trauma, and is also widely used, in the form of fluoroscopy, to provide intra-procedural image-guidance during surgical interventions. Although these two applications are relatively far removed, they both rely on x-rays. The central theme of this thesis is the application of clinical x-ray imaging to image-guidance during interventional procedures, as well as the measurement of musculoskeletal joint kinematics. The following literature review is therefore divided into these two themes that are main focus of this thesis: tracking during image-guided interventions (section §1.1), and measurement of joint kinematics (section §1.2). Additionally, a review of current digital radiography detector technologies is provided, along with a description of the perspective geometry of the standard projection radiography system (section §1.3).

## 1.1 Tracking in Image-guided Interventions

Image-guidance is used during interventions in a manner similar to modern navigational techniques that are employed to guide a submarine through the depths of the ocean.<sup>1</sup> In both cases a direct view of the surrounding environment is unavailable, and navigation (or guidance) must be supplemented through indirect means to arrive at the intended destination. During surgery it is often important to know precisely where an instrument is located with respect to the surgical target at all times during the procedure. Tracking systems fulfill this requirement, and are therefore an essential component of any intra-operative image-guidance system.<sup>1</sup> The following sections review some of the current techniques used for tracking purposes during image-guided interventions. The principles behind optical and electromagnetic tracking systems are reviewed, and their strengths and limitations are listed. Additionally, several tracking techniques based directly upon intra-operative medical imaging modalities are reviewed.

### 1.1.1 Optical Tracking

Although there are numerous variants of optical tracking systems (OTS), the type most widely used in clinical applications is based on the capture of infrared (IR) light.<sup>2</sup> IR-based OTS have been used in orthopaedic, neurological, craniofacial, otolaryngologic, and numerous other general surgical procedures.<sup>3</sup> IR-based OTS use optical band-pass filters to eliminate all other forms of ambient light outside of the IR range, making the task of identifying optical markers, or fiducials, simple and reliable.<sup>2</sup> There is a distinction between the types of fiducials utilized with OTS. For active optical tracking, the fiducials are infrared-emitting diodes (IREDs), while for passive optical tracking; they

are retro-reflective spheres, reflecting IR light back towards the source. Both types of fiducials are rigidly attached to surgical instruments, intraoperative imaging equipment, and also to the patient, enabling the tracking of all components in a common coordinate system.

Active OTS consists of a position sensor that contains either two or three coplanar charged coupled device (CCD) camera units, a central control unit, and the active fiducials either attached directly to a surgical instrument, or to a rigid reference frame (**Figure 1-1a,c**). The IREDs are fired sequentially and detected by each CCD unit. The position and orientation of the fiducials is determined by triangulation, based upon the prior fiducial geometric configuration, the firing sequence of the IREDs, and the known distance between the CCD units.<sup>2</sup> A minimum of three non-collinear fiducials are required to determine the six degrees-of-freedom (DOF) pose of the instrument or rigid frame. Active OTS are capable of tracking multiple rigid bodies simultaneously, as the central control unit controls their firing sequences. Since, the IREDs are powered, active OTS are typically wired systems.

Passive OTS consist of a position sensor capable of both emitting, and detecting IR light by means of illuminators (arrays of IREDs) and CCD units (**Figure 1-1b**), respectively. The position sensor emits IR light from its illuminators, similar to the flash of a conventional camera. The IR light floods the surrounding area, reflects off the retro-reflective spheres attached to surgical instruments to be tracked (**Figure 1-1d**), and is then detected by the CCD units. As with the active systems, the pose of the instrument or reference frame is identified by triangulation. However, since each instrument or reference frame is illuminated simultaneously, their geometric configuration must be

unique to ensure unambiguous identification.<sup>2</sup> Moreover, passive OTS do not require wires between the fiducials and the positioning sensor.

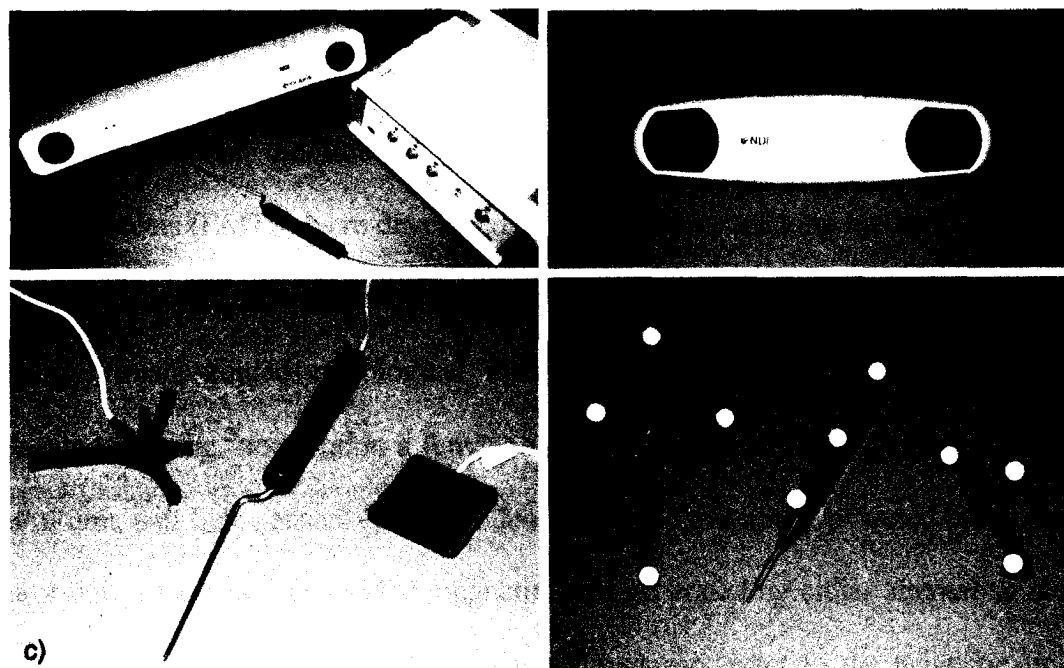


**Figure 1-1:** a) Active optical tracking system (OTS) consisting of position sensor, central control unit, and active tool (Northern Digital Polaris). b) Passive position sensor capable of both emitting and detecting infrared light (Northern Digital Vicra). c) Active instruments and reference frames containing infrared light emitting diodes. d) Passive instruments and reference frames containing retro-reflective spheres.

Numerous studies have examined the accuracy of OTS.<sup>3-5</sup> The accuracy of tracking an instrument or reference frame is dependent on a number of factors: the rigid body design, its characterization, the tracking algorithm (wired or wireless), dynamic motion, and the distance between instruments and reference frames.<sup>5</sup> In general, the accuracy of measuring the pose of an instrument or reference frame is better than 1 mm and 0.5° when design and methodological considerations are carefully taken into account.<sup>4,5</sup> This level of performance represents the main advantages of OTS, and has contributed to its success in the clinical environment. On the other hand, their main limitation is the requirement for uninterrupted line-of-sight between the optical fiducials

and the position sensor, which is often difficult to maintain in a crowded operating theatre.

### 1.1.2 Electromagnetic Tracking

To overcome the line-of-sight limitation imposed by OTS, electromagnetic tracking systems (EMTS) were developed as an alternative tracking method. EMTS have been incorporated into numerous procedures including motion detection in radiation oncology, image-guided radiological interventions, endoscopic procedures, and 3D ultrasound imaging,<sup>2</sup> to mention a few. An EMTS consist of a field generator, a central control unit, and field sensors (**Figure 1-2a**). The field generator, powered by the central control unit, produces a controlled magnetic field generated by either alternating current (AC), or pulsed direct current (DC). The field sensors react to the magnetic field to produce a signal that is dependant upon their position and orientation within the field. This signal is transmitted back to the central control unit where it is processed to determine the pose of field sensor. Field sensors come in both five DOF and six DOF configurations (**Figure 1-2b**).

The main distinction between AC-driven and DC-driven EMTS is their reactions to metallic objects that are in close proximity to either the field generator or field sensors. With AC-driven systems, eddy currents are induced within conductive materials, which in turn create an opposing magnetic field that interferes with the field created by the field generator.<sup>2</sup> This secondary field distorts the signals produced by the field sensors and leads to errors in the pose determination. With DC-driven systems the magnetic field is

pulsed on and off, allowing eddy currents to decay a sufficient amount to mitigate distortions caused by any opposing magnetic fields.

Another source of distortion that affects both AC and DC-driven systems is the presence of ferromagnetic materials. These materials become magnetic in the presence of an external magnetic field, and by a mechanism similar to that mentioned above, can distort the magnetic field created by the field generator, which negatively affects the measurement accuracy of EMTS. Additional sources of field distortions may include stray magnetic fields created by computer equipment and peripheral devices.<sup>2</sup>

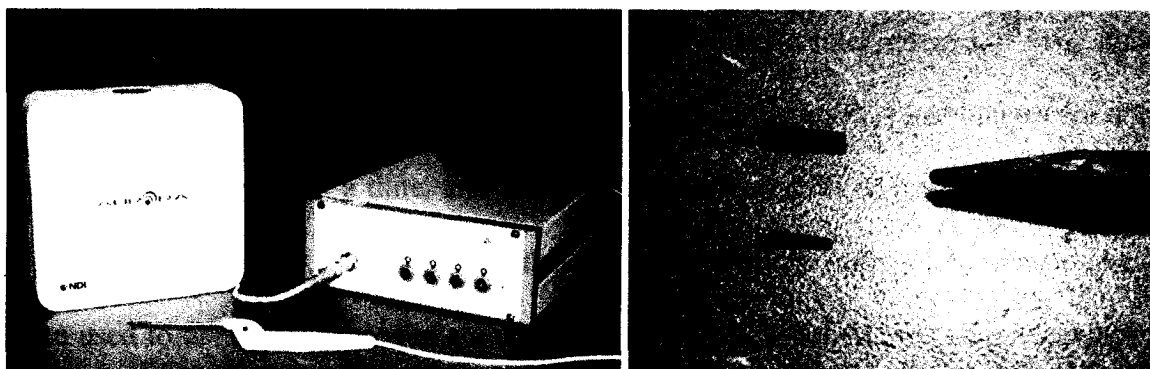


**Figure 1-2:** a) Electromagnetic tracking system (EMTS) consisting of field generator, central control unit, and tracked probe containing field sensor (Northern Digital Aurora). b) Miniature field sensors in six degree-of-freedom (top) and five degree-of-freedom (bottom) configurations.

Several studies have examined the accuracy of EMTS in both an undisturbed environment<sup>6-8</sup> (i.e. no sources of field distortions), as well as in the presence of surgical instruments and operating room equipment, as possible sources of field distortion.<sup>7-10</sup> The accuracy of EMTS was found to be dependent on the position of the field sensor with respect to the field generator. In an undisturbed environment, the accuracy of tracking the field sensor was in the range of 1 to 3 mm, and 0.5 to 1°.<sup>6</sup> When sources of field distortion are introduced into the tracking environment, they have a significant effect on the

accuracy of EMTS. Studies have reported tracking errors in the range of 1 to 20 mm, and 1 to 4°. <sup>7-10</sup> Although the accuracy of EMTS does not compete with OTS, it is relevant for numerous applications. The main advantage of EMTS is the lack of any line-of-sight limitations, and their ability to track flexible instruments such as catheters or endoscopes.

### 1.1.3 Tracking via Medical Imaging Modalities

Intra-procedural imaging via real-time medical imaging modalities is another technique that has been employed for tracking purposes. X-ray fluoroscopy has been long utilized as a means to guide instruments during percutaneous procedures, including endovascular catheter interventions and various orthopaedic interventions. <sup>1,11</sup> The main limitation of using conventional fluoroscopy for tracking purposes is that images are only available in one plane at a time, and therefore information derived from these images is typically limited to 2D. To overcome this limitation, biplane radiography systems have been used to obtain sequences of stereo projections from which 3D tracking information is derived. This technique has been used to track guide wires during endovascular interventions, <sup>12,13</sup> and also tumor motion during radiotherapy treatment of tumors. <sup>14</sup>

Ultrasound (US) has also been employed for many years as an interventional imaging modality. <sup>1</sup> Procedures that utilize ultrasound for guidance include percutaneous biopsies <sup>15</sup> and brachytherapy, <sup>16</sup> and treatment of musculoskeletal pain. <sup>17</sup> Since conventional US is constrained to a 2D fan beam, limited amounts of tracking information can be derived from its images. 3D US volumes are much better suited towards tracking and image-guidance applications. A 3D US volume can be reconstructed from a series of acquired 2D images, <sup>18</sup> or acquired directly with the use 3D

ultrasound transducers.<sup>19,20</sup> Using optimized image-processing techniques it is possible to segment, localize, and track instruments directly from 3D US datasets in real-time.<sup>21-23</sup> These tracking techniques are applicable to numerous percutaneous procedures, and also minimally invasive cardiac interventions.

Despite the real-time capability of both fluoroscopy and US, their images are often difficult to interpret for guidance purposes. This has led to the adaptation of computed tomography (CT) and magnetic resonance imaging (MRI), conventionally preoperative imaging modalities, to be incorporated into interventional suites. Interventional CT (iCT) is capable of CT fluoroscopy, which is the near real-time acquisition and display of 3D CT slices at rates of up to 8 frames-per-second (fps).<sup>24</sup> CT fluoroscopy has been utilized for guidance during numerous interventional procedures including biopsies, drainage procedures, and intracranial procedures.<sup>24</sup> In these procedures, the interventional instrument is generally a needle, which is visually tracked from updated display of CT images. The high level of radiation exposure to both the patient and interventionalist during CT fluoroscopy has limited its use to procedures short in duration (typically less than 3 min).

Several interventional MRI (iMRI) scanners have been developed for use in interventional suites, all of which increase the interventionalist's physical access (i.e. horizontal or 'double donut' bore design) to the patient compared to conventional diagnostic MRI scanners.<sup>1</sup> Advances in MRI hardware, and computing power have enabled the acquisitions of MRI slices in real-time. As a result, iMRI has been utilized for image-guidance during numerous interventions including biopsies, cryoablation, brachytherapy, neurosurgery, and numerous endovascular procedures.<sup>25-27</sup> Often

conventional surgical instruments cannot be used in an iMRI suite due to safety considerations or technical imaging issues. This has lead to the development of MR-compatible instruments that can be tracked or visualized within the acquired MR images. Two principal methods to tracking instruments directly from acquired MR images have been explored for use during interventional procedures: the use of passive or active markers.<sup>27,28</sup> Passive markers incorporate contrast agents or materials that produce a signal enhancement, void, or distortion, thereby enabling their localization directly within the MR slices. Active markers contain miniature MR receiver coils or antenna that are connected to the MRI scanner hardware. These coils produce signals during excitation by the external gradient fields, enabling their 3D localization. The majority of clinical experience with humans has been restricted to the use of passively tracked devices.<sup>29</sup> Although several actively tracked devices have been used successfully in animal studies, some safety concerns, mainly the generation of unwanted heat, have prevented their use within the clinic.

## 1.2 Techniques to Measure Joint Kinematics

Additional to its role in image-guided interventions, tracking technology has a significant impact in the measurement of joint kinematics. Measurement of joint kinematics plays an essential role in understanding normal joint function, as well as pathologies associated with musculoskeletal disorders and trauma. By gaining a deeper understanding of patient factors, the effectiveness of surgery and rehabilitation, and pathologies associated with musculoskeletal disorders it is possible to influence diagnoses and treatment, which can lead to improved patient outcome. The following section reviews several clinical techniques that can be used to measure and evaluate the skeletal kinematics of human subjects. The methodology of each technique is reviewed, and the strengths and limitations relating to its implementation are listed. Additionally, the measurement accuracy of each technique is reviewed for comparative purposes.

### 1.2.1 Gait Analysis

Gait analysis, or the study of locomotion, has numerous applications in medicine, competitive sports, and industry. It has been used extensively in the field of medicine to distinguish between pathological and normal gait.<sup>30</sup> This technique of motion capture has seen dramatic changes within the past decade mainly due to technological advances in computing power and data analysis techniques.<sup>31</sup> The current state-of-the-art gait lab contains a 3D motion capture system, comprising of up to ten infrared sensitive cameras that track and record the motion of retro reflective skin markers attached to a subject.<sup>30</sup> Current infrared cameras are capable of tracking the motion of these reflective markers at frequencies upwards to 250 Hz,<sup>31</sup> making them ideal for capturing detailed motions of a

subject during complex, dynamic activities. Ultimately, the motion and forces acting upon the skeleton can be inferred from the trajectories of the skin markers, and various pressure gauges attached to the subject using the inverse dynamics technique.<sup>32</sup>

One advantage of this technique is its ability to measure the motion of several joints simultaneously, which enables measurement of whole-body movements. The motion capture systems within a gait analysis lab have a very large operating volume, typically consisting of a 2 m wide by 10 m long walkway. This setup allows for motion measurements during a variety of both weight-bearing and non weight-bearing activities. Additionally, the technique is non-invasive and subjects are not exposed to any ionizing radiation.

On the other hand a major limitation of this technique is the estimation of skeletal kinematics from the trajectories of the skin markers. A potential for error arises due to the movement of skin and tissue relative to the underlying bone during physical activities.<sup>33</sup> Differences between joint kinematics derived from skin markers and those derived from direct skeletal measurements have been reported in the range of 10 mm<sup>34</sup> to 30 mm<sup>35</sup> for translations, and up to 15° for rotations.<sup>34</sup> Although numerous strategies and models have been developed to account for skin motion artefacts, the objective of reliable estimation of skeletal kinematics using skin markers has not yet been achieved.<sup>36</sup>

### 1.2.2 Intracortical Pin Fixation

Direct measurement of the underlying boney structures is preferred when accuracy is a necessity. One technique that directly measures skeletal motion involves the use of intracortical pins implanted directly into skeletal structures.<sup>37</sup> Novel six DOF spatial

localizer instruments,<sup>37</sup> and retro-reflective markers imaged by infrared sensitive cameras,<sup>38</sup> have been employed to measure motion. Since these instruments are rigidly attached to the skeletal structure via the intracortical pin, the skeletal kinematics derived from their measured motion provides an accurate representation of the actual bone kinematics. Ishii et al.<sup>37</sup> reported the measurement accuracy of their 6DOF spatial localizer instrument to be within 0.5 mm for translations and 0.5° for rotations. Similar accuracies have been reported with the use of optical measurement equipment.<sup>39</sup> This technique has been utilized *in vivo* to study both normal<sup>37</sup> and pathological knee kinematics, the latter arising due to anterior cruciate ligament deficiency.<sup>38</sup>

Advantages of this measurement technique include its ability to accurately measure skeletal kinematics. Despite the accuracy of the technique, the high degree of invasiveness associated with the procedure reduces its application in practice. For this procedure, subjects are required to undergo surgery to have the pins implanted into their bones. Additionally, significant pain was reportedly associated with the procedure, as the pins can unnaturally restrict the movement of soft tissue surrounding the insertion site.<sup>30</sup> This pain can be more pronounced during weight-bearing activities and as a result subjects may be limited to performing non weight-bearing activities.<sup>39</sup> Other methodological concerns for the use of intracortical pins include reports of pin deformation<sup>39</sup> and pin loosening<sup>40</sup> during dynamic activities.

### 1.2.3 Magnetic Resonance Imaging

Magnetic resonance imaging has been widely used to noninvasively measure 3D joint kinematics. Several studies have employed MRI to examine joint kinematics during

static weight-bearing, and non-weight-bearing activities. Sequential volumes of the joint are acquired in multiple static positions.<sup>41-43</sup> The observed motion between different positions can be calculated by using one of two analysis techniques. The first method involves manual identification of anatomical landmarks within each volume,<sup>43</sup> followed by point-based registration to calculate the rigid-body motion between the anatomical landmarks amongst sequential volumes, while the latter involves surface models segmented from the high-quality MRI volumes.<sup>41,44</sup> These surface models can then be registered to bone contours, identified within sequentially acquired, lower-quality volumes, using surface registration techniques to calculate motion between different multiple joint positions. The measurement accuracy of estimating 3D joint kinematics using these techniques has been reported in the range of 0.88 mm to 1.8 mm for translations, and 1.75° to 3° for rotations.<sup>41,42</sup>

MRI has also been used extensively to examine 3D joint kinematics during dynamic activities. The acquisition techniques used have been described by various names including kinematic MRI,<sup>45,46</sup> cine phase contrast MRI,<sup>47,48</sup> fast phase contrast MRI,<sup>49</sup> and motion-triggered cine MRI.<sup>50</sup> These techniques involve acquisition of MR images as a subject performs a periodic motion activity. Each MR image is acquired at a unique phase of the motion cycle. Thus, a single motion cycle can be represented using MR images acquired during multiple repetitions of the motion. Validation studies have reported accuracy of motion measurements within the range of 1 to 3 mm.<sup>47,48</sup>

There are several advantages to utilizing MRI to measure 3D joint kinematics: it is noninvasive, does not expose subjects to ionizing radiation, and has the added bonus of providing information about the soft tissues surrounding the joint. However, one of the

major limitations is the small operating volume, which is limited by the bore size of the MRI unit. As a result, activities performed inside the magnet are limited to a small range of motion, and only a single joint can be scanned at one time. Additionally, longer scan times, reported between 40 sec<sup>42</sup> and 5 min,<sup>49</sup> can make it challenging for subjects to perform weight-bearing activities, or repeatedly execute a cyclic movement.

#### 1.2.4 Computed Tomography

Computed tomography is another medical imaging modality that has been used to noninvasively measure joint kinematics.<sup>51-53</sup> Skeletal kinematics can be derived from volumetric CT images using rigid-registration techniques. Commonly, rigid registration is performed between like groups of anatomical landmarks, or surface contours identified in sequential volumes. Several studies have employed CT to examine the kinematics of the patellofemoral joint as a means to investigate causes of anterior knee pain,<sup>54-56</sup> and validated the accuracy of measuring skeletal kinematics from CT volumes in the range of 0.5 mm to 3 mm for translations, and 0.7° to 3° for rotations.<sup>57</sup>

The major limitation of using CT to measure joint kinematics is the exposure of the subject to relatively large amounts of ionizing radiation. Other limitations include the restrictive working volume of the CT bore that limits examination of a single joint at one time, and poor soft tissue contrast in CT images, which does not provide information about the soft tissues surrounding the joint. However, CT does provide excellent delineation of boney structures, making it ideal for extracting surface features and landmarks for registration and modeling purposes.

### 1.2.5 Radiostereometric Analysis

Radiostereometric analysis (RSA) is a technique to obtain accurate 3D spatial measurements from radiographs.<sup>58</sup> RSA was first introduced in 1974 by Göran Selvik as a means of studying the skeletal system *in vivo*.<sup>59</sup> Since its inception, the technique has been refined through numerous scientific contributions,<sup>60-63</sup> and seen significant advances due to the growth of digital technologies and computing power.<sup>64-66</sup> RSA is an effective clinical tool that has been utilized for numerous clinical applications in orthopaedics,<sup>67-71</sup> pediatrics,<sup>72,73</sup> odontology and plastic surgery,<sup>74</sup> rheumatology,<sup>75,76</sup> and neurology.<sup>77-79</sup> RSA has also been used extensively to study skeletal kinematics.<sup>80-84</sup>

RSA requires the implantation of at least 3 non-colinear markers, introduced into the skeletal segment under clinical examination to enable its localization in 3D space. Studies have suggested that 6 to 9 markers be utilized *in vivo* to ensure localization with a high accuracy.<sup>63</sup> Spherical tantalum markers, 0.8 mm or 1.0 mm in diameter, are commonly used in clinical studies, since tantalum possesses a high biocompatibility,<sup>85</sup> and is also fairly radio-opaque, resulting in high contrast within radiographs. The technique generates a 3D spatial model of the markers using stereographic x-ray sources that produce stereo projection images of the skeletal segment (implanted with markers) during a simultaneous radiographic exposure. A calibration cage is present during the image acquisition and allows the photogrammetric projective parameters of the x-ray systems to be determined (section §1.3.4). A 3D spatial model of the markers implanted into the skeletal segment can be calculated through the intersection of the rays cast between the image of each marker within the stereo projection images and their respective x-ray foci (**Figure 1-3**).

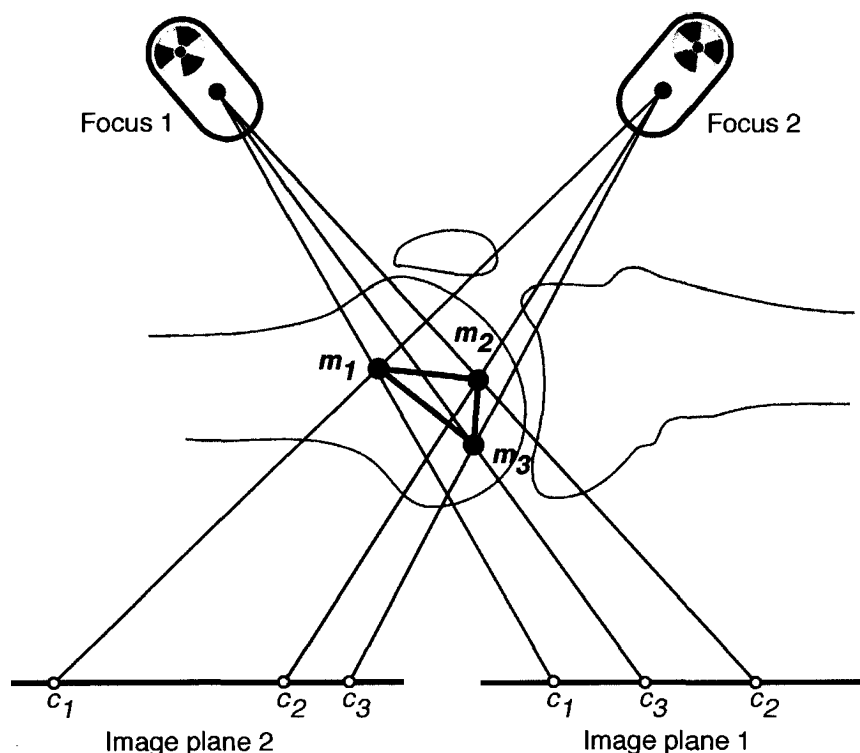


**Figure 1-3:** Spatial reconstruction of 3D position of tantalum markers implanted into the skeleton using radiostereometric analysis (RSA). The 3D reconstructed position of each marker ( $m_i$ ) is determined by the intersection of the rays cast between the projections of each marker in the pair of stereo images ( $c_i$ ) and its respective x-ray focus.

To measure joint kinematics, successive RSA examinations of the joint under investigation must be performed. The observed motion between successive examinations can be quantified by performing a rigid point-based registration between the 3D spatial models of the markers derived from each RSA examination.<sup>86</sup> In RSA motion is described in both absolute and relative terms. Absolute motion describes the movement of a single rigid-body segment during a finite time interval, while relative motion describes the movement between two rigid-body segments during a finite time interval (**Figure 1-4**). A detailed methodology of calculating absolute and relative motion using point-based registration has previously been described.<sup>86,87</sup> Motion is commonly presented in terms of translations and Euler angular-rotations, using six DOF.<sup>63</sup> The accuracy of localizing a

rigid body in 3D space using RSA has been reported in the range of 0.01 to 0.25 mm and 0.03 to 0.6°. <sup>58,88</sup>

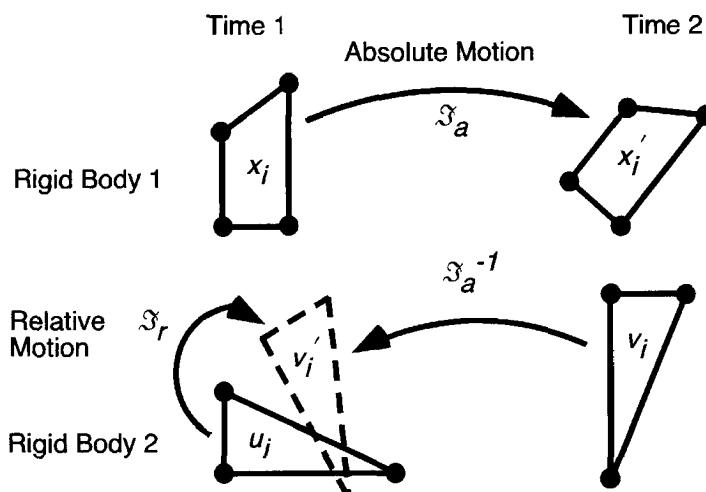


**Figure 1-4:** The computation of absolute motion and relative motion of rigid body 2 to rigid body 1. Absolute motion of rigid body 1 is calculated by finding the transformation  $\mathcal{S}_a(x_j) = x_j' = [R_a]^T x_j + d_a$ , which describes the motion of rigid body 1 between times 1 and 2. The inverse of this movement is then used to transform the points in rigid body 2 at time 2 from the positions  $v_i$  to positions  $\mathcal{S}_a^{-1}(v_i) = v_i' = [R]_a^T v_i - [R]_a^T d_a$ . Finally, the relative motion between the two rigid bodies can be computed such that  $\mathcal{S}_r(u_i) = v_i'$ . Adapted from Söderkvist et al. <sup>86</sup>

RSA is accepted as the de-facto *gold standard* for obtaining accurate 3D measurement of the skeletal system. The high measurement accuracy is the main advantage of utilizing RSA to measure joint kinematics. Disadvantages of RSA include exposure to ionizing radiation, the requirement that markers be implanted in the skeleton, and the small operating volume, which is defined by the intersection of the two x-ray beams. Because RSA relies on markers implanted into the skeleton, it is typically limited to examining subjects who have undergone corrective surgery. Implantation of skeletal markers may easily be incorporated into a preexisting surgical plan by means of a simple bead insertion instrument. <sup>89</sup> The small operation volume of RSA limits the type of activities that can be performed, and only allows for examination of a single joint at one

time. Additionally, a conventional RSA setup employs film cassettes that must be manually interchanged between examinations, preventing dynamic studies from being performed using a conventional RSA system. Although several dynamic joint studies have been performed using a specialized film exchanger apparatus that enabled frame rates of up to 4 frames per second,<sup>82,83,90</sup> this device is one-of-a-kind and therefore is not widely available.

### 1.2.6 Biplane Radiography

Because of the static nature of conventional, film-based RSA, the technique has been extended to digital radiography systems capable of real-time image acquisition. Several studies have utilized image intensifier-based, biplane radiography systems to measure joint kinematics during dynamic activities.<sup>91-94</sup> Marker-based techniques for measuring joint kinematics with biplane radiography are based on the same principles as conventional RSA (section §1.2.5). The accuracy of measuring joint kinematics using marker-based techniques with an intensifier-based radiography system has been reported in the range of 0.08 mm to 0.2 mm for translations, and 0.3° to 1.6° for rotations.<sup>92</sup>

To overcome the requirement of implanting markers into the skeleton, several model-based techniques have been developed and implemented using biplane radiography systems.<sup>91,95,96</sup> The main assumption of model-based techniques is that a properly orientated projection through a 3D volumetric model will produce an image similar to the obtained radiograph.<sup>91</sup> Therefore, model-based techniques to measure joint kinematics rely on a subject specific model of the joint under examination. This model is typically obtained by acquiring a CT scan of the joint. By reconstructing the projective

geometry of the biplane radiography system, digitally reconstructed radiographs (DRRs) can be rendered by ray-casting through the subject specific model (**Figure 1-5**),<sup>93,95</sup> or 3D texture mapped volume rendering.<sup>91</sup> In either case, the 3D pose of a joint is determined from a set of acquired stereo radiographs using an iterative search that modifies the pose of the subject specific model to optimize matching between the DRRs and the stereo radiographs. Motion is quantified by the change in the 3D pose of the model determined from subsequent pairs of stereo radiographs. Validation studies have reported the accuracy of this technique in the range of 0.4 mm to 0.8 mm for translations, and 0.8° to 2.5° for rotations.<sup>91,96</sup>

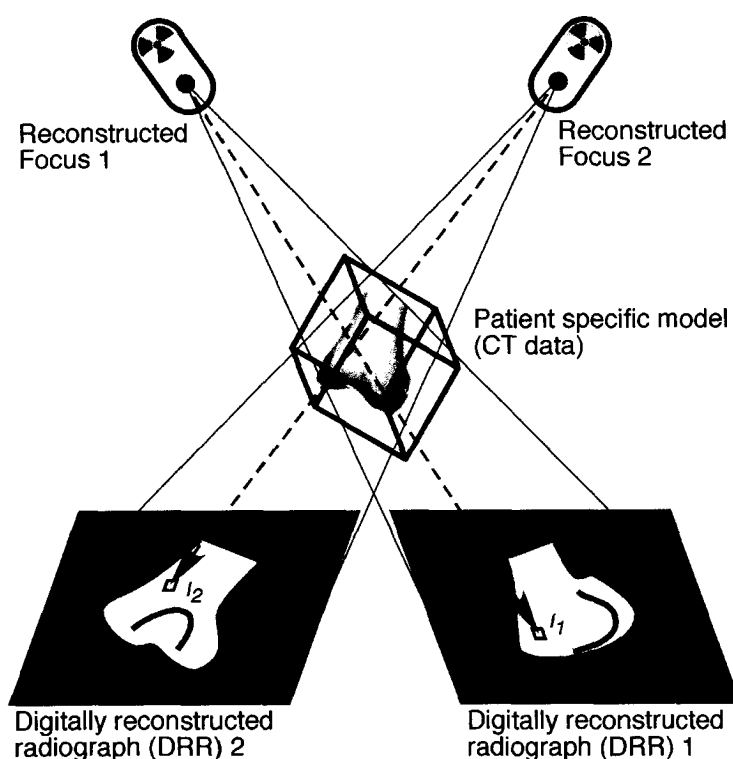


**Figure 1-5:** Model-based measurement of kinematics using biplane radiography. Digitally reconstructed radiographs (DRRs) are rendered using ray-casting techniques. The intensity values of the pixels,  $I_1$  and  $I_2$ , are determined by summation of the attenuation coefficients of the voxels within model along the ray path between pixels,  $I_1$  and  $I_2$ , and their corresponding x-ray focus.

An advantage of using biplane radiography to measure joint kinematics is the ability to acquire images in real-time, enabling dynamic analysis. In addition, both marker-based and model-based techniques can measure joint kinematics with a high degree of accuracy. Model-based techniques have the added advantage of not requiring markers implanted into the skeleton to measure its motion. Disadvantages of using biplane radiography include exposure to ionizing radiation, and its small operating volume (defined by the intersection of the x-ray beams), which limits the examination to a single joint at one time. Additionally, biplane radiography systems often have a restrictive setup, limiting the type of activities a subject can perform, and can making it technically challenging to ensure the joint under examination remains within the operating volume during a dynamic activity.<sup>94</sup>

### 1.2.7 Single-plane Radiography

Single-plane radiography is a long-standing medical imaging modality that is widely available, and employed for numerous diagnostic, therapeutic, and interventional purposes. Because of its wide availability, single-plane radiography systems have been utilized in numerous studies to examine and measure joint kinematics.<sup>97-100</sup> As with biplane radiography, there are two main distinctions in the techniques used to measure joint kinematics using single-plane radiography: marker-based techniques, similar to RSA (section §1.2.5), rely on radio-opaque markers implanted into the skeleton, and model-based techniques (section §1.2.6) rely on a subject specific volumetric model of the joint under examination.

Several marker-based techniques for measuring joint kinematics have been implemented using single-plane radiography, most notably on intensifier-based C-arm radiography systems. To compensate for the limited amount of information available from a single perspective view, the 3D spatial distribution or geometry of the implanted markers must be known *a priori*. The 3D pose of the rigid-body implanted with markers is determined by performing 3D-to-2D registration between the known 3D geometry of markers and their corresponding projections in 2D radiographs (**Figure 1-6**). Motion between subsequent 3D poses of the rigid-body containing the markers is calculated using similar point-based registration methods employed in RSA (section §1.2.5).

Validation studies have been performed to assess the accuracy of single-plane, marker-based localization, all of which found that translations occurring orthogonal to the image plane (out-of-plane) were measured with a lower accuracy than those that occurred parallel to the image plane (in-plane). The accuracy of measuring translation has been reported in the range of 0.1 mm to 1 mm in-plane, and 0.7 mm to 2.1 mm out-of-plane, while rotational accuracy was reported in the range of 0.3° to 1.7° about all axes.<sup>101-104</sup>

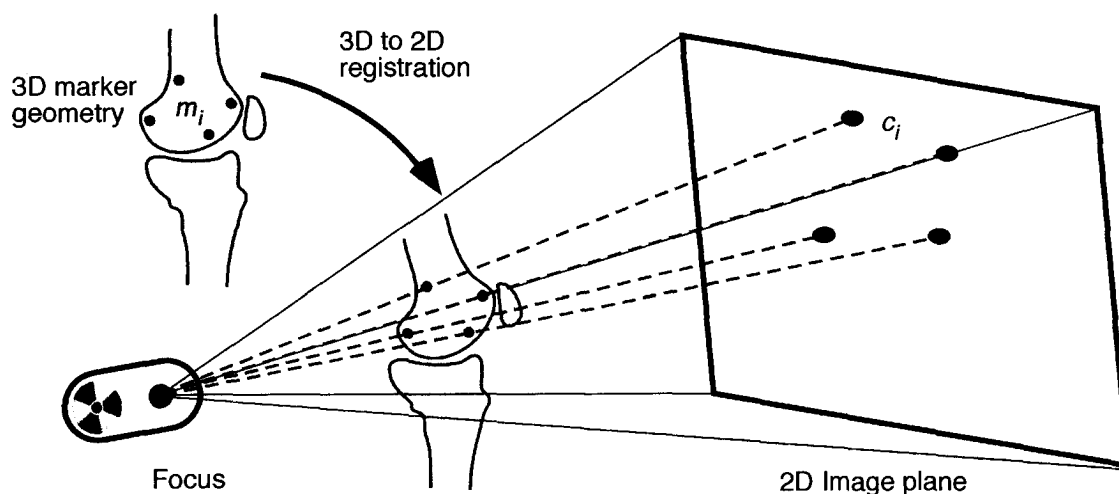


**Figure 1-6:** Technique to estimate 3D pose of joint implanted with markers from a single-perspective projection. Markers implanted into the skeleton,  $m_i$ , are fit to the projection lines cast between the marker projections,  $c_i$ , and the x-ray focus using a 3D-to-2D registration algorithm.

Model-based techniques allow joint kinematics to be measured without the need for markers implanted into the skeleton. However, there is the requirement of a patient specific model of the joint. This model can be obtained from a CT scan, or if the subject has a joint replacement, from the CAD geometry of the implant. Several studies have implemented this technique using intensifier-based C-arm radiography systems to study joint kinematics.<sup>97,102,105-107</sup> Similar, ray-casting<sup>102,108,109</sup> or graphics rendering algorithms<sup>110</sup> are used to render DRRs (section §1.2.6). Often, only the surface geometry of the joint or joint replacement is extracted from the CT volume, or CAD design,<sup>105,106,108</sup> limiting the rendering of DRRs to contours or silhouettes of the surface geometry (**Figure 1-7**). The 3D pose of the model obtained from CT or CAD geometry is modified such that a matching criterion between the DRR and the acquired single-perspective radiographs is optimized. Motion of a joint can be quantified by tracking the change in the 3D pose of the model as it is matched to a sequence of radiographs. As with the marker-based techniques, the accuracy of measuring translations in the out-of-plane direction was found

to be significantly lower than those measured in-plane. Validation studies have reported the accuracy of single-plane, model-based techniques in the range of 0.3 mm to 1.5 mm, and 1.5 mm to 5.6 mm for measuring translations in-plane and out-of-plane respectively, and in the range of  $0.4^{\circ}$  to  $2.0^{\circ}$  for measuring rotations.<sup>105,108-111</sup>

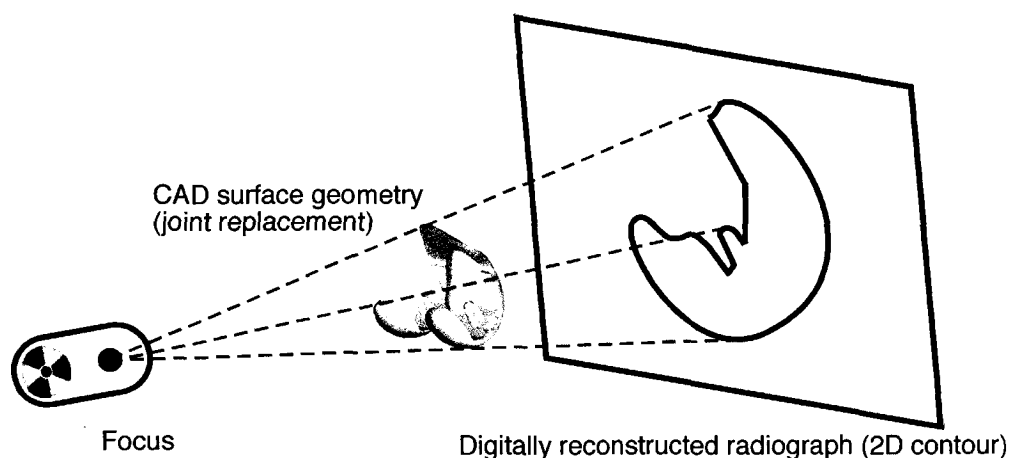


**Figure 1-7:** Perspective projection of CAD surface geometry on single-plane radiography system. A digitally reconstructed radiography (DRR) is rendered using ray-casting techniques.

The wide availability of single-plane radiography systems enables the measurement of joint kinematics in the typical hospital or research environment. In addition, the working volume spans the entire field of view of the radiography system. This volume is typically much larger than spatial region of intersection between stereoscopic x-ray sources used in RSA and biplane radiography, resulting in the ability to easily capture and measure numerous dynamic activities. The main drawback of single-plane techniques is the lower accuracy of pose estimation in the direction orthogonal to the imaging plane, compared to estimations of pose in the in-plane directions. Additionally, as with all radiology-based techniques of measuring joint kinematics, subjects are exposed to ionizing radiation.

## 1.3 Digital Radiography and Perspective X-ray Systems

With current trends towards all-digital environments, digital radiography systems are commonplace in modern hospitals. The transition to an all-digital radiology department is spurred by several advantages that digital radiography systems offer over conventional film-based radiography, including: higher patient throughput, immediate image viewing, computer aided diagnoses and intervention, and convenient storage of images on computer disks rather than in archaic film stacks.<sup>112</sup> X-ray image intensifiers (XRII) have long been a staple of digital radiography. However, with the recent widespread implementation of flat-panel (FP) detectors they are poised to eventually replace the use of XRIIs altogether.<sup>113</sup> The following section reviews the imaging chain of both image intensifiers (IIs) and FP detectors, and lists some of the advantages and limitations associated with these detector technologies. Additionally, the geometry of a typical perspective x-ray system is visited, and a common method to determining the photogrammetric projective parameters of perspective x-ray systems is briefly reviewed.

### 1.3.1 X-ray Image Intensifiers

Since their introduction in the mid 1950's XRII have seen significant technological advances in their design. Now, digital image technology is intrinsic to most modern XRII radiography systems. The imaging chain of a typical XRII radiography system, which converts incident x-rays into a digital image, is shown in **Figure 1-8a**. The II consists of four main components (**Figure 1-8b**): (a) a vacuum bottle that keeps air out, (b) an input layer that converts the incident x-ray signal to electrons, (c) electronic

lenses that focus the electrons, and (d) an output phosphor that converts the accelerated electrons into visible light.<sup>113</sup>

The input screen of the II is made up of several layers (**Figure 1-8c**), the first being the vacuum window, typically a thin 1 mm aluminum barrier that is part of the vacuum bottle, designed to minimize x-ray absorption and for mechanical strength under atmospheric pressure. After passing through the input window, x-rays are incident upon the input phosphor, which absorbs incident x-rays and converts their energy into visible light. This phosphor must be sufficiently thick to absorb the majority of incident x-rays, but thin enough to not significantly degrade spatial resolution. Therefore, virtually all modern IIs use cesium iodide (CsI) for the input phosphor. Cesium iodide has the property of forming long, needle-like crystals, which act as light pipes channeling the visible light toward the photocathode with minimal lateral diffusion.<sup>113</sup> The photocathode is a thin layer of antimony and alkali metals that emit electrons when struck by visible light.

Once x-rays have been converted to electrons within the input screen, the latter are accelerated across a high-strength electric field created between the photocathode and anode. The accelerated electrons are focused down to the size of the output phosphor by a series of electrostatic focusing electrodes. After penetrating the thin anode, the high-energy electrons strike the output phosphor causing the emission of a burst of light. The output phosphor is typically made of 4 to 8  $\mu\text{m}$  of zinc cadmium sulfide doped with silver, deposited directly on the output window of the II.<sup>113</sup> Each electron that strikes the output phosphor causes the emission of approximately 1000 light photons.

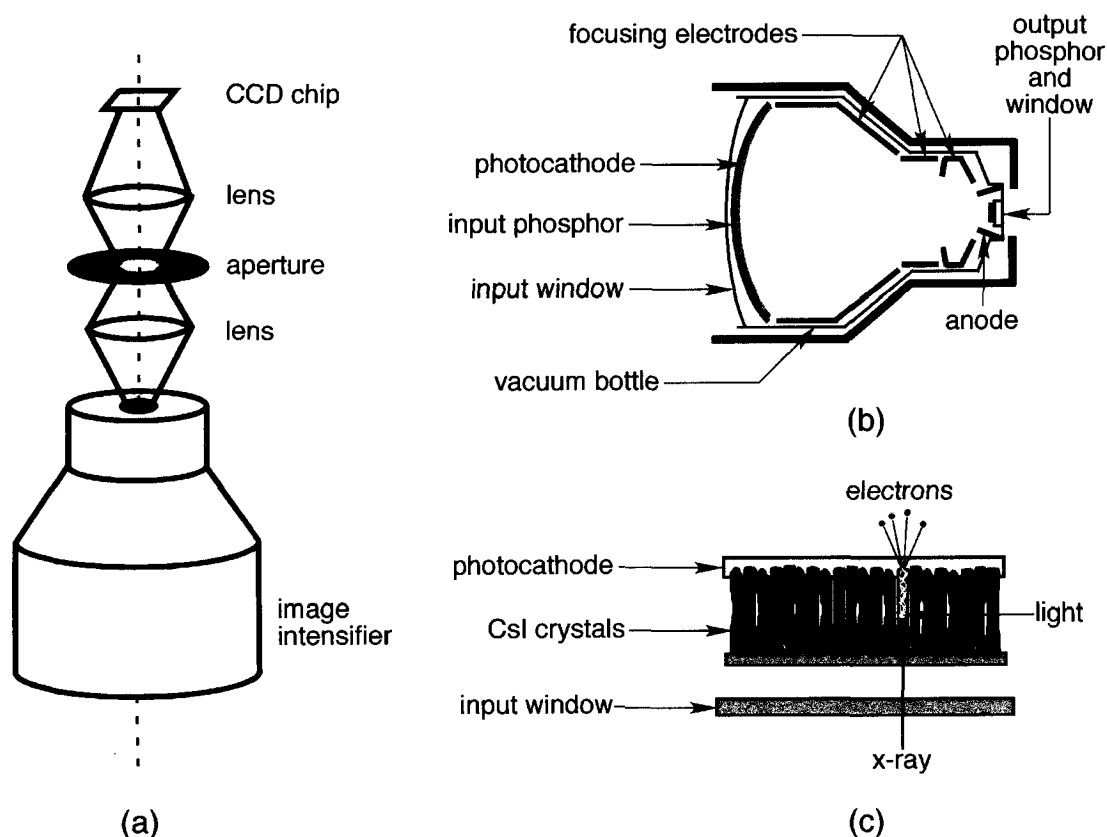


**Figure 1-8:** (a) Imaging chain of a digital image intensifier radiography system; (b) internal structure of an image intensifier; (c) input screen of an image intensifier. Adapted from Bushberg et al.<sup>113</sup>

The small analog image is focused onto a digital camera assembly to produce a digital output image. The optic assembly consists of two lenses and a variable aperture. The lenses act to focus the incoming light onto a charged coupled device (CCD) chip. The variable aperture controls the amount of light that passes through the lens assembly, similar to the iris of a human eye. Adjustment of the aperture has an important effect on the performance of the radiography system. Constricting the iris of the aperture lowers the amount of light passing through it, resulting in a higher x-ray exposure to maintain the exposure of light at the CCD, which in turn reduces noise in the digital image. Dilating the iris of the aperture allows more light to pass through, allowing a lower x-ray exposure

to maintain the light exposure at the CCD. This results in a lower dose, but also reduced image quality.

The primary feature of CCD detectors is that the CCD chip itself is an integrated circuit, with discrete pixel electronics etched into its surface.<sup>113</sup> The surface of a CDD is photosensitive; therefore as light falls on each pixel, electrons are liberated and accumulate charge within the pixel. Electron emission is proportional to the intensity of incident light. The pixel values of a digital image produced from a CCD are the quantized and encoded form of the magnitude of charge built up within each pixel of the CCD chip following exposure to light.

XRIIs have several advantages inherent to their design. First, the collection and focusing of electrons by the electrostatic field is a very efficient process and overcomes any inefficiencies of the photocathode.<sup>114</sup> Additionally, the acceleration of electrons within the II, and the minification of the image from the input phosphor to the output phosphor produce large gains, and allows for coupling of an II to external optics and electronics.

However, the bulky nature of IIs can often impede the clinician by limiting access to patient and preventing acquisition of important radiographic views.<sup>114</sup> Moreover, image contrast losses occur due to the scattering of light and x-rays within the II, also referred to as veiling glare.<sup>112</sup> Finally, XRIIs are susceptible to a number of magnetic and electric field-dependant defects. Geometric distortion of images occur due to the mapping of electrons from a concave photocathode onto a planar output screen curvature of the input phosphor, producing pincushion distortions.<sup>115</sup> In addition, the curvature of the input

screen also produces a non-uniform distribution of brightness across the image, referred to as vignetting. Also, IIs are subject to a second form of geometric distortion, known as 'S' distortion, due to the influence of extraneous magnetic field on the electrostatic field within the II.<sup>113</sup> The impact of 'S' distortion is compounded by the fact that it varies with change in orientation of the II.

### 1.3.2 Flat Panel Detectors

In recent years there has been significant research and development in the area of active-matrix arrays, which allows the deposition of semiconductors across large-area substrates in a well-controlled fashion.<sup>112</sup> The coupling of traditional x-ray detection media, such as phosphors or photoconductors, with large-area active-matrix structures (**Figure 1-9c**) forms the basis of FP x-ray detectors. There is currently a distinction between two types of FP detectors: indirect and direct detectors. Indirect FP detectors incorporate a phosphor layer that produces visible light upon detection of x-rays, whereas direct FP detectors incorporate a photoconductor that produces electrical charges upon detection of an x-ray.

In the indirect method of x-ray detection a phosphor layer is placed in close contact with an active-matrix array (**Figure 1-9a**). Common phosphors used in FP detectors include terbium-doped gadolinium oxysulfide ( $\text{Gd}_2\text{O}_2\text{S:Tb}$ ) and thallium-doped cesium iodide ( $\text{CsI:Tl}$ ).<sup>112</sup> The intensity of light emitted from the phosphor layer is directly proportional to the intensity of the x-ray beam incident upon its surface. Each pixel on the active-matrix array contains a photosensitive element that generates electrical charge whose magnitude is proportional to the intensity of light incident upon its surface.

This charge is stored within the pixel until the active-matrix is read out. The pixels of the resulting digital image contain the quantized and encoded magnitudes of the charges stored within the pixels of the active-matrix array. Since the x-rays are converted first to visible light and then finally to electrical charge (from which the image information is derived), the detection process is termed *indirect*.

In the direct detection scheme, x-rays are detected with a thick layer of photoconductor material (such as selenium)<sup>113</sup> deposited on top of the active-matrix array (**Figure 1-9b**). A negative voltage is applied to a thin electrode on the front surface of the photoconductive layer, producing an electric field across the photoconductor. Incident x-rays interact with the photoconductor liberating electrons, which migrate towards the pixels of the active-matrix array under the influence of the electric field, to create a charge at each element. Each pixel on the active-matrix array contains a capacitive storage element that accumulates the electrons incident upon its surface until the active-matrix is read out and the charge transferred to an A/D converter. The detection process is termed *direct* since x-ray photons are converted directly to an electrical charge, from which the digital image is formed, without any intermediary stage.

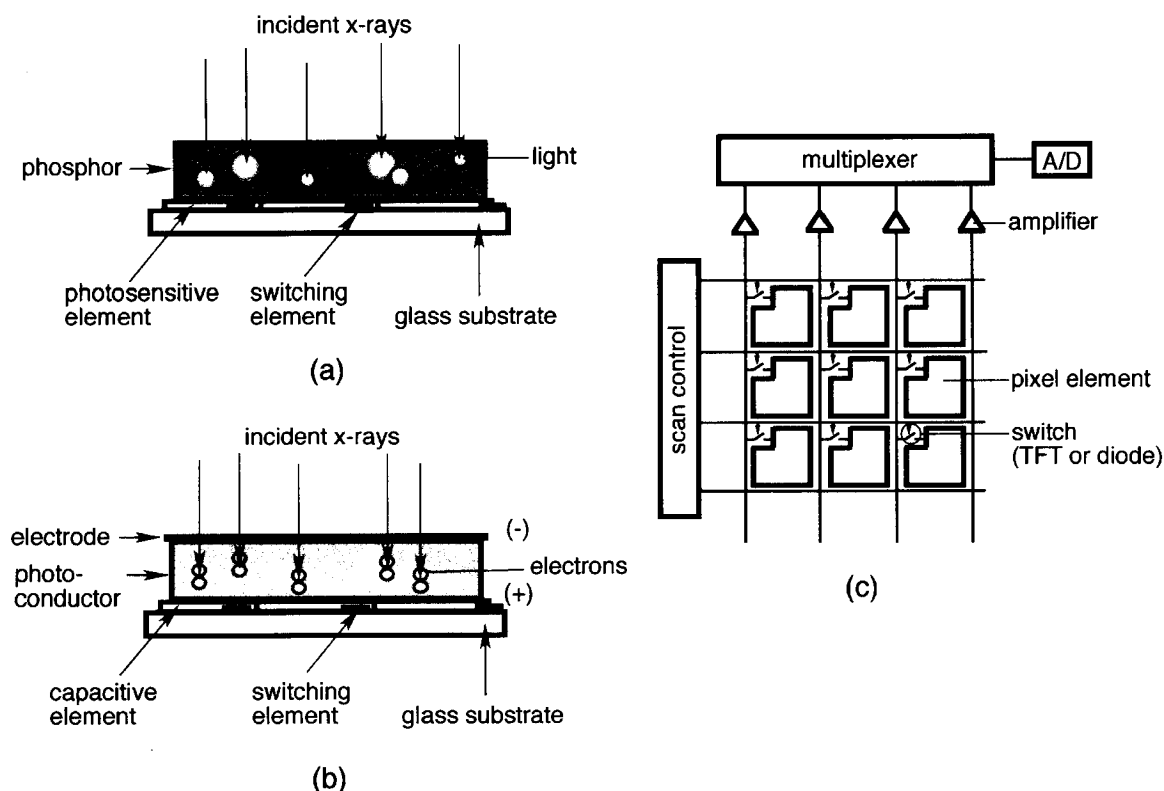


**Figure 1-9:** (a) Cross-section of indirect detection flat panel; (b) cross-section of direct detection flat panel; (c) schematic diagram of an active-matrix array and electronics used to control readout. Each pixel element within the active-matrix consists of either a discrete photosensitive or capacitive detector, and a switch, usually a thin field transistor (TFT) or diode. Adapted from Bushberg et al.<sup>113</sup> and Beutel et al.<sup>112</sup>

Flat-panel detectors overcome several of the limitations associated with XRIIs. FP detectors are significantly more compact, allowing better access to a patient. Their flat geometry frees them from veiling glare, vignetting, and geometric distortion,<sup>112</sup> which greatly facilitates quantitative image analysis, registration, and 3D reconstruction.<sup>114</sup> Additionally, unlike XRIIs, FP detectors are immune to magnetic fields, and therefore can be used within magnetic environments such as MRI suites. FP detectors however, are not flawless. They can often suffer from lag and ghosting effects (i.e. production of a spurious frozen pattern that mirrors image content produced by preceding x-ray exposures, and reflects a non-uniform variation in a detector response depending upon its

exposure history).<sup>115</sup> Lag quantifies the ability of a detector to accurately record time-varying changes, and results from the carry-over of the measured signal into succeeding frames. Most flat-panel detectors incorporate measures to minimize these effects.

### 1.3.3 Geometry of the Perspective Radiography System

Photogrammetry is concerned with obtaining 3D measurements from information contained in 2D images.<sup>116</sup> Performing photogrammetric measurements with an x-ray system requires knowledge of the projective parameters that define the geometry of the imaging system. A photogrammetric camera system consists of an imaging plane and a perspective centre.<sup>117</sup> In the radiographic context, the x-ray focus is synonymous with the perspective centre, and the image plane, the detector. A perspective projection defines the transformation of a 3D point in object space onto the 2D image plane (**Figure 1-10**). Additional parameters that describe the geometry of a perspective camera system include the principle distance and principle point. The principle point is the point on the image plane given by the intersection of the perspective centre and a line orthogonal to the image plane.<sup>117</sup> The distance between the principle point and perspective centre is termed the principle distance. Often in radiography, this distance is referred to as the source-to-detector distance.

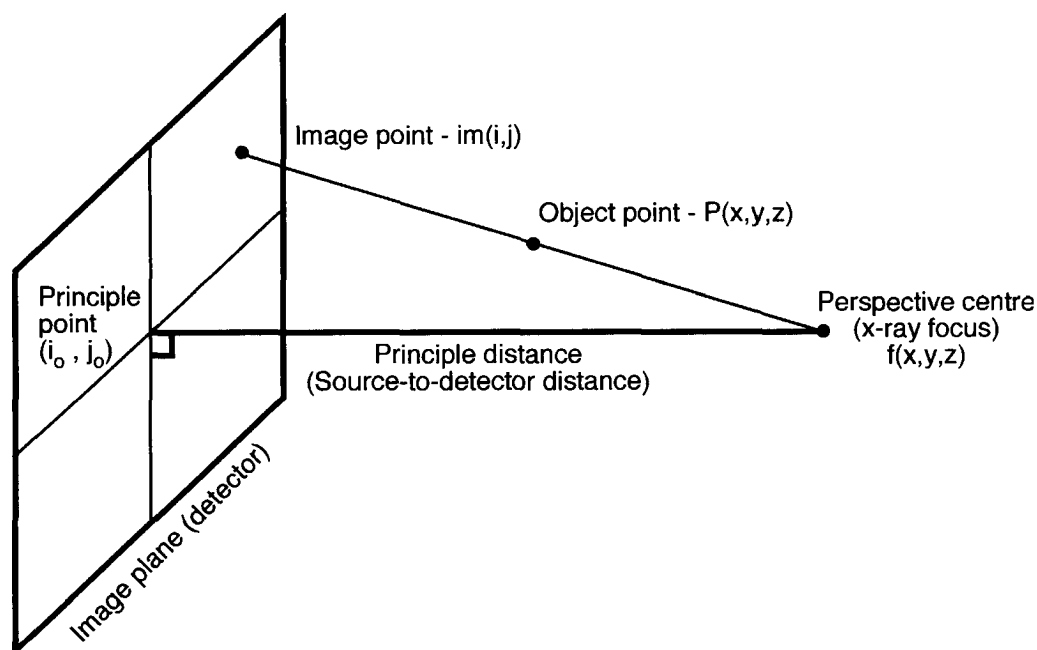


**Figure 1-10:** Central perspective projection of object point,  $P(x,y,z)$ , onto imaging plane,  $im(i,j)$ . The geometry of a radiography system can be described by the perspective centre (x-ray focus), the principle distance (source-to-detector distance), and the principle point,  $(i_o, j_o)$ , on the imaging plane (detector). Adapted from Mikhail et al.<sup>117</sup>

### 1.3.4 Determination of Projective Parameters

Determination of the perspective parameters of a radiography system often consists of acquiring radiographic projections of a calibration cage, an enclosure often comprising of two parallel, radio-translucent plates (referred to as the fiducial plane and the control plane) embedded with radio-opaque markers (**Figure 1-11**). The position of the radio-opaque markers must be well characterized in relation to the origin of the enclosure. The calibration process consists of two steps: the first determines the mathematical relationship between the 2D coordinate system of the imaging plane and the 3D coordinate system of the calibration cage, which defines the object coordinate system, while the second involves the calculation of the 3D position of the x-ray focus with respect to the calibration cage coordinate system.

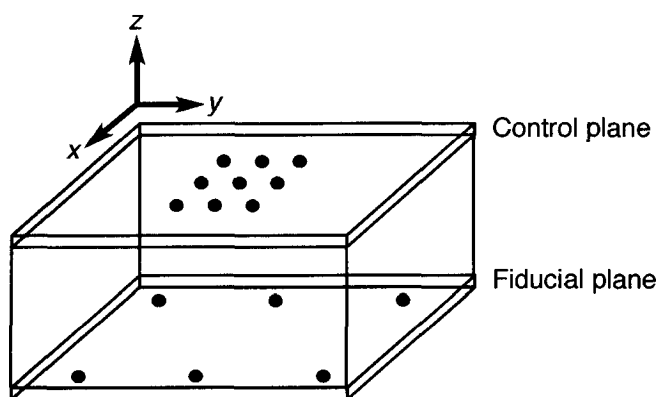


**Figure 1-11:** A calibration cage is used to determine the photogrammetric projective parameters of a perspective x-ray system. Calibration cages usually contain two radio-transparent plates embedded with radio-opaque markers. The fiducial plane is used to determine the direct linear transformation (DLT), which transforms 2D image points into the 3D object coordinate system. The control plane is used to determine the position of the x-ray focus.

The relationship between the image plane and the 3D coordinate system of the calibration cage can be described mathematically by a projective transformation,<sup>59</sup> also referred to as the direct linear transformation (DLT). The DLT describes the mapping between points within the image plane and the fiducial plane of the calibration cage within the 3D object coordinate system, and is just one way to describe the projective transformation between the image and object coordinate systems. Other mathematical formulations that describe this projective transformation have been proposed and validated, but have shown no distinct advantages over the original solution.<sup>118,119</sup>

To compute the 3D position of the x-ray focus with respect to the calibration cage, points lying on the control plane of the calibration cage are identified within the projection radiograph and mapped to the fiducial plane using the DLT. Theoretically, the x-ray focus is the intersection of the lines connecting the points on the control plane, and their projections mapped onto the fiducial plane. Realistically, these lines may not intersect, since the focus of a radiography system is of a finite size, and there are

measurement errors associated with localizing the marker projections within a radiograph. Therefore, the focus position is determined as the point with the least sum squared distance between the lines connecting the points on the control plane and their corresponding projections.<sup>59</sup>

## 1.4 Thesis Proposal

This thesis focuses on two distinct medical applications, mainly tracking for image-guided interventions and measurement of joint kinematics, using radiographic imaging and registration techniques. Previous work in these areas has laid the foundation for localizing objects in 3D space from single-perspective radiographic projections,<sup>101,120,121</sup> and optimizing radiographic acquisition parameters towards this task.<sup>121</sup> With the widespread implementation of digital radiography systems, and the recent implementation of FP detector technology, the potential to apply these techniques towards dynamics tasks, such as object tracking and measurement of joint kinematics, is well posed and highly realizable. The overall objective of this study can be subdivided into the following specific aims.

- 1) Design, test and validate a technique to track objects in 3D space from a dynamic sequence of single-perspective projections.
- 2) Quantitatively compare two generations of digital radiography systems, specifically an intensifier-based and flat panel radiography system, towards the tracking application.
- 3) Validate a technique to dynamically measure joint kinematics from single-perspective projections.
- 4) Determine the effective dose of ionizing radiation imparted to a human subject during a radiographic examination performed to measure joint kinematics.

## 1.5 Thesis Outline

The achievement of the above thesis objectives is presented in the following two chapters, which are intended for publication in peer-reviewed journals. These two chapters form the body of the thesis, followed by a summary chapter, which presents the main findings of this thesis, and isolates key areas of research for future work.

*Chapter 2* consists of a study that addresses the first two aims listed above. In this chapter a description of the software implementation, that performs the automated image measurements and the registration enabling the tracking of objects in 3D space from single-perspective projections, is provided. Subsequently, testing and validation of the technique were performed via a series of *in vitro* experiments. These experiments were performed on two clinically available digital radiography systems, to provide a quantitative comparison of the two digital detector technologies that could be utilized for application of the technique.

*Chapter 3* describes the methods used to address the final two aims listed above. A quick overview of the techniques utilized to measure the joint kinematics from single-perspective projection is provided (this is based upon the software implementation presented in Chapter 2, and previous work). Validation of the technique was performed through a series of *in vitro* experiments that utilized an anatomically relevant joint phantom. An additional *in vitro* experiment was performed to estimate the effective dose of ionizing radiation that would be associated with the measurement procedure.

## 1.6 References

1. Peters TM. 2006. Image-guidance for surgical procedures. *Phys Med Biol* 51: R505-540.
2. Peters T, Cleary K (editors). 2008. *Image-guided interventions - technology and applications* New York, NY: Springer.
3. Khadem R, Yeh CC, Sadeghi-Tehrani M, Bax MR, Johnson JA, Welch JN, Wilkinson EP, Shahidi R. 2000. Comparative tracking error analysis of five different optical tracking systems. *Comput Aided Surg* 5: 98-107.
4. West JB, Maurer CR, Jr. 2004. Designing optically tracked instruments for image-guided surgery. *IEEE Trans Med Imaging* 23: 533-545.
5. Wiles AD, Thompson DG, Frantz DD. 2004. Accuracy assessment and interpretation for optical tracking systems. In, *SPIE - Medical Imaging 2004*, pp. 421-432.
6. Frantz DD, Wiles AD, Leis SE, Kirsch SR. 2003. Accuracy assessment protocols for electromagnetic tracking systems. *Phys Med Biol* 48: 2241-2251.
7. Hummel JB, Bax MR, Figl ML, Kang Y, Maurer C, Jr., Birkfellner WW, Bergmann H, Shahidi R. 2005. Design and application of an assessment protocol for electromagnetic tracking systems. *Med Phys* 32: 2371-2379.
8. Hummel J, Figl M, Birkfellner W, Bax MR, Shahidi R, Maurer CR, Jr., Bergmann H. 2006. Evaluation of a new electromagnetic tracking system using a standardized assessment protocol. *Phys Med Biol* 51: N205-210.
9. Hummel J, Figl M, Kollmann C, Bergmann H, Birkfellner W. 2002. Evaluation of a miniature electromagnetic position tracker. *Med Phys* 29: 2205-2212.
10. Schicho K, Figl M, Donat M, Birkfellner W, Seemann R, Wagner A, Bergmann H, Ewers R. 2005. Stability of miniature electromagnetic tracking systems. *Phys Med Biol* 50: 2089-2098.
11. Kahler DM. 2004. Image guidance: fluoroscopic navigation. *Clin Orthop Relat Res*: 70-76.
12. Baert SA, van Walsum T, Niessen WJ. 2003. Endpoint localization in guide wire tracking during endovascular interventions. *Acad Radiol* 10: 1424-1432.
13. Baert SA, van de Kraats EB, van Walsum T, Viergever MA, Niessen WJ. 2003. Three-dimensional guide-wire reconstruction from biplane image sequences for integrated display in 3-D vasculature. *IEEE Trans Med Imaging* 22: 1252-1258.

14. Harada T, Shirato H, Ogura S, Oizumi S, Yamazaki K, Shimizu S, Onimaru R, Miyasaka K, Nishimura M, Dosaka-Akita H. 2002. Real-time tumor-tracking radiation therapy for lung carcinoma by the aid of insertion of a gold marker using bronchofiberscopy. *Cancer* 95: 1720-1727.
15. Middleton WD, Teefey SA, Dahiya N. 2006. Ultrasound-guided chest biopsies. *Ultrasound Q* 22: 241-252.
16. Carey B, Swift S. 2007. The current role of imaging for prostate brachytherapy. *Cancer Imaging* 7: 27-33.
17. Adler RS, Sofka CM. 2003. Percutaneous ultrasound-guided injections in the musculoskeletal system. *Ultrasound Q* 19: 3-12.
18. Fenster A, Downey DB, Cardinal HN. 2001. Three-dimensional ultrasound imaging. *Phys Med Biol* 46: R67-99.
19. Sugeng L, Coon P, Weinert L, Jolly N, Lammertin G, Bednarz JE, Thiele K, Lang RM. 2006. Use of real-time 3-dimensional transthoracic echocardiography in the evaluation of mitral valve disease. *J Am Soc Echocardiogr* 19: 413-421.
20. Ryan LP, Salgo IS, Gorman RC, Gorman JH, 3rd. 2006. The emerging role of three-dimensional echocardiography in mitral valve repair. *Semin Thorac Cardiovasc Surg* 18: 126-134.
21. Ding M, Fenster A. 2003. A real-time biopsy needle segmentation technique using Hough transform. *Med Phys* 30: 2222-2233.
22. Wei Z, Gardi L, Downey DB, Fenster A. 2005. Oblique needle segmentation and tracking for 3D TRUS guided prostate brachytherapy. *Med Phys* 32: 2928-2941.
23. Novotny PM, Stoll JA, Vasilyev NV, del Nido PJ, Dupont PE, Zickler TE, Howe RD. 2007. GPU based real-time instrument tracking with three-dimensional ultrasound. *Med Image Anal* 11: 458-464.
24. Froelich JJ, Wagner HJ. 2001. CT-fluoroscopy: Tool or gimmick? *Cardiovasc Intervent Radiol* 24: 297-305.
25. Tatli S, Morrison PR, Tuncali K, Silverman SG. 2007. Interventional MRI for oncologic applications. *Tech Vasc Interv Radiol* 10: 159-170.
26. Mittal S, Black PM. 2006. Intraoperative magnetic resonance imaging in neurosurgery: the Brigham concept. *Acta Neurochir Suppl* 98: 77-86.
27. Henk CB, Higgins CB, Saeed M. 2005. Endovascular interventional MRI. *J Magn Reson Imaging* 22: 451-460.

28. Kos S, Huegeli R, Bongartz GM, Jacob AL, Bilecen D. 2008. MR-guided endovascular interventions: a comprehensive review on techniques and applications. *Eur Radiol* 18: 645-657.
29. Ozturk C, Guttman M, McVeigh ER, Lederman RJ. 2005. Magnetic resonance imaging-guided vascular interventions. *Top Magn Reson Imaging* 16: 369-381.
30. Sutherland DH. 2002. The evolution of clinical gait analysis. Part II kinematics. *Gait Posture* 16: 159-179.
31. Chester VL, Biden EN, Tingley M. 2005. Gait analysis. *Biomed Instrum Technol* 39: 64-74.
32. Hatze H. 2002. The fundamental problem of myoskeletal inverse dynamics and its implications. *J Biomech* 35: 109-115.
33. Cappozzo A, Catani F, Leardini A, Benedetti MG, Croce UD. 1996. Position and orientation in space of bones during movement: experimental artefacts. *Clin Biomech (Bristol, Avon)* 11: 90-100.
34. Benoit DL, Ramsey DK, Lamontagne M, Xu L, Wretenberg P, Renstrom P. 2006. Effect of skin movement artifact on knee kinematics during gait and cutting motions measured in vivo. *Gait Posture* 24: 152-164.
35. Stagni R, Fantozzi S, Cappello A, Leardini A. 2005. Quantification of soft tissue artefact in motion analysis by combining 3D fluoroscopy and stereophotogrammetry: a study on two subjects. *Clin Biomech (Bristol, Avon)* 20: 320-329.
36. Leardini A, Chiari L, Della Croce U, Cappozzo A. 2005. Human movement analysis using stereophotogrammetry. Part 3. Soft tissue artifact assessment and compensation. *Gait Posture* 21: 212-225.
37. Ishii Y, Terajima K, Terashima S, Koga Y. 1997. Three-dimensional kinematics of the human knee with intracortical pin fixation. *Clin Orthop Relat Res*: 144-150.
38. Ramsey DK, Lamontagne M, Wretenberg PF, Valentin A, Engstrom B, Nemeth G. 2001. Assessment of functional knee bracing: an in vivo three-dimensional kinematic analysis of the anterior cruciate deficient knee. *Clin Biomech (Bristol, Avon)* 16: 61-70.
39. Ramsey DK, Wretenberg PF, Benoit DL, Lamontagne M, Nemeth G. 2003. Methodological concerns using intra-cortical pins to measure tibiofemoral kinematics. *Knee Surg Sports Traumatol Arthrosc* 11: 344-349.
40. Reinschmidt C, van den Bogert AJ, Nigg BM, Lundberg A, Murphy N. 1997. Effect of skin movement on the analysis of skeletal knee joint motion during running. *J Biomech* 30: 729-732.

41. Patel VV, Hall K, Ries M, Lotz J, Ozhinsky E, Lindsey C, Lu Y, Majumdar S. 2004. A three-dimensional MRI analysis of knee kinematics. *J Orthop Res* 22: 283-292.
42. Fellows RA, Hill NA, Gill HS, MacIntyre NJ, Harrison MM, Ellis RE, Wilson DR. 2005. Magnetic resonance imaging for in vivo assessment of three-dimensional patellar tracking. *J Biomech* 38: 1643-1652.
43. McPherson A, Karrholm J, Pinskerova V, Sosna A, Martelli S. 2005. Imaging knee position using MRI, RSA/CT and 3D digitisation. *J Biomech* 38: 263-268.
44. Fellows RA, Hill NA, Macintyre NJ, Harrison MM, Ellis RE, Wilson DR. 2005. Repeatability of a novel technique for in vivo measurement of three-dimensional patellar tracking using magnetic resonance imaging. *J Magn Reson Imaging* 22: 145-153.
45. Shellock FG, Mink JH, Deutsch A, Pressman BD. 1991. Kinematic magnetic resonance imaging of the joints: techniques and clinical applications. *Magn Reson Q* 7: 104-135.
46. Powers CM, Shellock FG, Pfaff M. 1998. Quantification of patellar tracking using kinematic MRI. *J Magn Reson Imaging* 8: 724-732.
47. Sheehan FT, Zajac FE, Drace JE. 1998. Using cine phase contrast magnetic resonance imaging to non-invasively study in vivo knee dynamics. *J Biomech* 31: 21-26.
48. Barrance PJ, Williams GN, Novotny JE, Buchanan TS. 2005. A method for measurement of joint kinematics in vivo by registration of 3-D geometric models with cine phase contrast magnetic resonance imaging data. *J Biomech Eng* 127: 829-837.
49. Rebmann AJ, Sheehan FT. 2003. Precise 3D skeletal kinematics using fast phase contrast magnetic resonance imaging. *J Magn Reson Imaging* 17: 206-213.
50. Melchert UH, Schroder C, Brossmann J, Muhle C. 1992. Motion-triggered cine MR imaging of active joint movement. *Magn Reson Imaging* 10: 457-460.
51. Feipel V, Rooze M. 1999. Three-dimensional motion patterns of the carpal bones: an in vivo study using three-dimensional computed tomography and clinical applications. *Surg Radiol Anat* 21: 125-131.
52. Shapeero LG, Dye SF, Lipton MJ, Gould RG, Galvin EG, Genant HK. 1988. Functional dynamics of the knee joint by ultrafast, cine-CT. *Invest Radiol* 23: 118-123.
53. Dupuy DE, Hangen DH, Zachazewski JE, Boland AL, Palmer W. 1997. Kinematic CT of the patellofemoral joint. *AJR Am J Roentgenol* 169: 211-215.

54. Pinar H, Akseki D, Karaoglan O, Genc I. 1994. Kinematic and dynamic axial computed tomography of the patello-femoral joint in patients with anterior knee pain. *Knee Surg Sports Traumatol Arthrosc* 2: 170-173.
55. Muhle C, Brossmann J, Heller M. 1999. Kinematic CT and MR imaging of the patellofemoral joint. *Eur Radiol* 9: 508-518.
56. Elias DA, White LM. 2004. Imaging of patellofemoral disorders. *Clin Radiol* 59: 543-557.
57. Neu CP, McGovern RD, Crisco JJ. 2000. Kinematic accuracy of three surface registration methods in a three-dimensional wrist bone study. *J Biomech Eng* 122: 528-533.
58. Karrholm J. 1989. Roentgen stereophotogrammetry. Review of orthopedic applications. *Acta Orthop Scand* 60: 491-503.
59. Selvik G. 1989. Roentgen stereophotogrammetry. A method for the study of the kinematics of the skeletal system. *Acta Orthop Scand Suppl* 232: 1-51.
60. Selvik G, Alberius P, Aronson AS. 1983. A roentgen stereophotogrammetric system. Construction, calibration and technical accuracy. *Acta Radiol Diagn (Stockh)* 24: 343-352.
61. Nystrom L, Soderkvist I, Wedin PA. 1994. A note on some identification problems arising in roentgen stereo photogrammetric analysis. *J Biomech* 27: 1291-1294.
62. Valstar ER, de Jong FW, Vrooman HA, Rozing PM, Reiber JH. 2001. Model-based Roentgen stereophotogrammetry of orthopaedic implants. *J Biomech* 34: 715-722.
63. Valstar ER, Gill R, Ryd L, Flivik G, Borlin N, Karrholm J. 2005. Guidelines for standardization of radiostereometry (RSA) of implants. *Acta Orthop* 76: 563-572.
64. Ostgaard SE, Gottlieb L, Toksvig-Larsen S, Lebech A, Talbot A, Lund B. 1997. Roentgen stereophotogrammetric analysis using computer-based image-analysis. *J Biomech* 30: 993-995.
65. Valstar ER, Vrooman HA, Toksvig-Larsen S, Ryd L, Nelissen RG. 2000. Digital automated RSA compared to manually operated RSA. *J Biomech* 33: 1593-1599.
66. Borlin N, Thien T, Karrholm J. 2002. The precision of radiostereometric measurements. Manual vs. digital measurements. *J Biomech* 35: 69-79.
67. Brostrom LA, Goldie I, Selvik G. 1989. Micromotion of the total knee. *Acta Orthop Scand* 60: 443-445.

68. Ahl T, Dalen N, Selvik G. 1989. Ankle fractures. A clinical and roentgenographic stereophotogrammetric study. *Clin Orthop Relat Res*: 246-255.
69. Hansson U, Toksvig-Larsen S, Jorn LP, Ryd L. 2005. Mobile vs. fixed meniscal bearing in total knee replacement: a randomised radiostereometric study. *Knee* 12: 414-418.
70. Madanat R, Moritz N, Larsson S, Aro HT. 2006. RSA applications in monitoring of fracture healing in clinical trials. *Scand J Surg* 95: 119-127.
71. Bragdon CR, Greene ME, Freiberg AA, Harris WH, Malchau H. 2007. Radiostereometric analysis comparison of wear of highly cross-linked polyethylene against 36- vs 28-mm femoral heads. *J Arthroplasty* 22: 125-129.
72. Karrholm J, Hansson LI, Selvik G. 1984. Longitudinal growth rate of the distal tibia and fibula in children. *Clin Orthop Relat Res*: 121-128.
73. Hildebrand H, Aronson S, Kullendorff CM, Selvik G. 1991. Roentgen stereophotogrammetric short-term analysis of growth rate in children operated for Crohn's disease. *Acta Paediatr Scand* 80: 917-923.
74. Rune B, Sarnas KV, Aberg M. 1999. Mandibulofacial dysostosis--variability in facial morphology and growth: a long-term profile roentgenographic and roentgen stereometric analysis of three patients. *Cleft Palate Craniofac J* 36: 110-122.
75. Nilsson KG, Karrholm J, Ekelund L, Magnusson P. 1991. Evaluation of micromotion in cemented vs uncemented knee arthroplasty in osteoarthritis and rheumatoid arthritis. Randomized study using roentgen stereophotogrammetric analysis. *J Arthroplasty* 6: 265-278.
76. van der Linde MJ, Garling EH, Valstar ER, Tonino AJ, Nelissen RG. 2006. Peripatite may not improve micromotion of knee prostheses in rheumatoid arthritis. *Clin Orthop Relat Res* 448: 122-128.
77. Johnsson R, Selvik G, Stromqvist B, Sundén G. 1990. Mobility of the lower lumbar spine after posterolateral fusion determined by roentgen stereophotogrammetric analysis. *Spine* 15: 347-350.
78. Gunnarsson G, Axelsson P, Johnsson R, Stromqvist B. 2000. A method to evaluate the in vivo behaviour of lumbar spine implants. *Eur Spine J* 9: 230-234.
79. Axelsson P, Karlsson BS. 2005. Standardized provocation of lumbar spine mobility: three methods compared by radiostereometric analysis. *Spine* 30: 792-797.
80. Karrholm J, Selvik G, Elmqvist LG, Hansson LI. 1988. Active knee motion after cruciate ligament rupture. Stereoradiography. *Acta Orthop Scand* 59: 158-164.

81. Karrholm J, Elmqvist LG, Selvik G, Hansson LI. 1989. Chronic anterolateral instability of the knee. A roentgen stereophotogrammetric evaluation. *Am J Sports Med* 17: 555-563.
82. Jonsson H, Karrholm J, Elmqvist LG. 1989. Kinematics of active knee extension after tear of the anterior cruciate ligament. *Am J Sports Med* 17: 796-802.
83. Jonsson H, Karrholm J. 1999. Three-dimensional knee kinematics and stability in patients with a posterior cruciate ligament tear. *J Orthop Res* 17: 185-191.
84. Karrholm J, Brandsson S, Freeman MA. 2000. Tibiofemoral movement 4: changes of axial tibial rotation caused by forced rotation at the weight-bearing knee studied by RSA. *J Bone Joint Surg Br* 82: 1201-1203.
85. Aronson AS, Jonsson N, Alberius P. 1985. Tantalum markers in radiography. An assessment of tissue reactions. *Skeletal Radiol* 14: 207-211.
86. Soderkvist I, Wedin PA. 1993. Determining the movements of the skeleton using well-configured markers. *J Biomech* 26: 1473-1477.
87. Yuan X, Ryd L. 2000. Accuracy analysis for RSA: a computer simulation study on 3D marker reconstruction. *J Biomech* 33: 493-498.
88. Bragdon CR, Malchau H, Yuan X, Perinchief R, Karrholm J, Borlin N, Estok DM, Harris WH. 2002. Experimental assessment of precision and accuracy of radiostereometric analysis for the determination of polyethylene wear in a total hip replacement model. *J Orthop Res* 20: 688-695.
89. Aronson AS, Hoist L, Selvik G. 1974. An instrument for insertion of radiopaque bone markers. *Radiology* 113: 733-734.
90. Brandsson S, Karlsson J, Sward L, Kartus J, Eriksson BI, Karrholm J. 2002. Kinematics and laxity of the knee joint after anterior cruciate ligament reconstruction: pre- and postoperative radiostereometric studies. *Am J Sports Med* 30: 361-367.
91. You BM, Siy P, Anderst W, Tashman S. 2001. In vivo measurement of 3-D skeletal kinematics from sequences of biplane radiographs: application to knee kinematics. *IEEE Trans Med Imaging* 20: 514-525.
92. Tashman S, Anderst W. 2003. In-vivo measurement of dynamic joint motion using high speed biplane radiography and CT: application to canine ACL deficiency. *J Biomech Eng* 125: 238-245.
93. Bey MJ, Zauel R, Brock SK, Tashman S. 2006. Validation of a new model-based tracking technique for measuring three-dimensional, in vivo glenohumeral joint kinematics. *J Biomech Eng* 128: 604-609.

94. Li G, Van de Velde SK, Bingham JT. 2008. Validation of a non-invasive fluoroscopic imaging technique for the measurement of dynamic knee joint motion. *J Biomech* 41: 1616-1622.
95. Li G, Wuerz TH, DeFrate LE. 2004. Feasibility of using orthogonal fluoroscopic images to measure in vivo joint kinematics. *J Biomech Eng* 126: 314-318.
96. Bey MJ, Kline SK, Tashman S, Zauel R. 2008. Accuracy of biplane x-ray imaging combined with model-based tracking for measuring in-vivo patellofemoral joint motion. *J Orthop Surg* 3: 38.
97. Hoff WA, Komistek RD, Dennis DA, Gabriel SM, Walker SA. 1998. Three-dimensional determination of femoral-tibial contact positions under in vivo conditions using fluoroscopy. *Clin Biomech (Bristol, Avon)* 13: 455-472.
98. Komistek RD, Allain J, Anderson DT, Dennis DA, Goutallier D. 2002. In vivo kinematics for subjects with and without an anterior cruciate ligament. *Clin Orthop Relat Res*: 315-325.
99. Zihlmann MS, Gerber H, Stacoff A, Burckhardt K, Szekely G, Stussi E. 2006. Three-dimensional kinematics and kinetics of total knee arthroplasty during level walking using single plane video-fluoroscopy and force plates: a pilot study. *Gait Posture* 24: 475-481.
100. Garling EH, Kaptein BL, Nelissen RG, Valstar ER. 2007. Limited rotation of the mobile-bearing in a rotating platform total knee prosthesis. *J Biomech* 40 Suppl 1: S25-30.
101. Yuan X, Ryd L, Tanner KE, Lidgren L. 2002. Roentgen single-plane photogrammetric analysis (RSPA.) A new approach to the study of musculoskeletal movement. *J Bone Joint Surg Br* 84: 908-914.
102. Tang TS, MacIntyre NJ, Gill HS, Fellows RA, Hill NA, Wilson DR, Ellis RE. 2004. Accurate assessment of patellar tracking using fiducial and intensity-based fluoroscopic techniques. *Med Image Anal* 8: 343-351.
103. Garling EH, Kaptein BL, Geleijns K, Nelissen RG, Valstar ER. 2005. Marker Configuration Model-Based Roentgen Fluoroscopic Analysis. *J Biomech* 38: 893-901.
104. Ioppolo J, Borlin N, Bragdon C, Li M, Price R, Wood D, Malchau H, Nivbrant B. 2007. Validation of a low-dose hybrid RSA and fluoroscopy technique: Determination of accuracy, bias and precision. *J Biomech* 40: 686-692.
105. Banks SA, Hodge WA. 1996. Accurate measurement of three-dimensional knee replacement kinematics using single-plane fluoroscopy. *IEEE Trans Biomed Eng* 43: 638-649.

106. Komistek RD, Dennis DA, Mahfouz M. 2003. In vivo fluoroscopic analysis of the normal human knee. *Clin Orthop Relat Res*: 69-81.
107. Dennis DA, Mahfouz MR, Komistek RD, Hoff W. 2005. In vivo determination of normal and anterior cruciate ligament-deficient knee kinematics. *J Biomech* 38: 241-253.
108. Zuffi S, Leardini A, Catani F, Fantozzi S, Cappello A. 1999. A model-based method for the reconstruction of total knee replacement kinematics. *IEEE Trans Med Imaging* 18: 981-991.
109. Yamazaki T, Watanabe T, Nakajima Y, Sugamoto K, Tomita T, Yoshikawa H, Tamura S. 2004. Improvement of depth position in 2-D/3-D registration of knee implants using single-plane fluoroscopy. *IEEE Trans Med Imaging* 23: 602-612.
110. Mahfouz MR, Hoff WA, Komistek RD, Dennis DA. 2003. A robust method for registration of three-dimensional knee implant models to two-dimensional fluoroscopy images. *IEEE Trans Med Imaging* 22: 1561-1574.
111. Fregly BJ, Rahman HA, Banks SA. 2005. Theoretical accuracy of model-based shape matching for measuring natural knee kinematics with single-plane fluoroscopy. *J Biomech Eng* 127: 692-699.
112. Beutel J, Kundel HL, Van Metter RL (editors). 2000. *Handbook of medical imaging - vol. 1: physics and psychophysics*. Bellingham, WA: SPIE Press.
113. Bushberg JT, Seibert JA, Leidholdt Jr. EM, Boone JM. 2002. *The essential physics of medical imaging*. Lippincott Williams & Wilkins, Philadelphia, PA.
114. Yaffe MJ, Rowlands JA. 1997. X-ray detectors for digital radiography. *Phys Med Biol* 42: 1-39.
115. Cowen AR, Davies AG, Sivananthan MU. 2008. The design and imaging characteristics of dynamic, solid-state, flat-panel x-ray image detectors for digital fluoroscopy and fluorography. *Clin Radiol* 63: 1073-1085.
116. Fryer J, Mitchell H, Chandler J (editors). 2007. *Applications of 3D measurements from images*. Dunbeath, Scotland: Whittles Publishing.
117. Mikhail EM, Bethel JS, McGlone JC. 2001. *Introduction to modern photogrammetry*. JohnWiley & Sons, Inc., Toronto, ON.
118. Choo AM, Oxland TR. 2003. Improved RSA accuracy with DLT and balanced calibration marker distributions with an assessment of initial-calibration. *J Biomech* 36: 259-264.

119. Borlin N. 2002. Comparison of resection-intersection algorithms and projection geometries in radiostereometry. *ISPRS Journal of Photogrammetry & Remote Sensing* 56: 390-400.
120. Hoffmann KR, Esthappen J. 1997. Determination of three-dimensional positions of known sparse objects from a single projection. *Med Phys* 24: 555-564.
121. Habets DF, Pollmann SI, Yuan X, Peters TM, Holdsworth DW. 2009. Error analysis of marker-based object localization using a single-plane XRII. *Med Phys* 36: 190-200.

## 2 Tracking of Sparse Objects from Single-perspective Projections towards Image-guided Applications

### 2.1 Introduction

The role of medical imaging and image guidance is rapidly increasing in all aspects of surgery and therapy, including treatment planning and follow-up of many interventions.<sup>1-3</sup> Fluoroscopy and x-ray images are utilized intra-operatively to provide guidance and target localization during many procedures,<sup>1,3,4</sup> however these imaging modalities are typically limited to a 2D context. The quality of image guidance could be greatly improved if surgical targets and tools were given a 3D context.<sup>2,5-7</sup> To overcome the limited information provided by 2D x-ray imaging, numerous technologies have been considered, including optical or magnetic tracking systems,<sup>8,9</sup> and even more complex x-ray imaging systems such as biplane x-ray or dual-source, single-detector x-ray.<sup>10-12</sup> However, these systems are accompanied by their own set of limitations.

Although, optical tracking systems are typically employed within computer-aided surgery suites, because of their robustness, reliability and accuracy, they require uninterrupted line-of-sight, which may not be practical during many intra-operative or dynamic procedures. Magnetic tracking systems do not require line-of-sight, but are

susceptible to magnetic field disturbances, caused by the presence of ferromagnetic materials and electrical equipment, which negatively affects their reliability.<sup>13-15</sup> Biplane x-ray systems and stereoscopic imaging techniques can be used to calculate 3D information<sup>16-18</sup> and have been utilized for numerous applications. However, many applications – such as measurement of joint kinematics, gait analysis, and cardiac imaging<sup>19-21</sup> – are limited to, or benefit from, image acquisition with a single x-ray projection plane. Benefits of single-plane acquisition are particularly apparent in the operating room, where two large C-arms can significantly restrict access to the patient. While single-plane stereo x-ray systems can provide 3D image guidance, provided that the imaging system geometry is known and fixed,<sup>11,12</sup> their use is limited by availability, restrictive mechanical setup, and need for re-calibration subsequent to any change in imaging parameters. A single-plane, single-source x-ray system capable of providing 3D localization would not be limited by these restrictions.

3D localization using a single-plane, single-source x-ray system is possible, provided that the tracked object is constructed with rigidly affixed, radio-opaque markers, whose relative dimensions are known.<sup>22</sup> Several 3D-to-2D registration methods have been developed to provide 3D localization from single-perspective, 2D projections. These registration methods can be grouped into basic linear solvers or iteratively refined algorithms.<sup>19,22-25</sup> An iterative, single x-ray source approach to 3D localization has been described by Hoffmann et al.,<sup>22</sup> and further expanded upon by Habets et al.<sup>25</sup> The iterative 3D-to-2D registration finds an optimized solution to the projection-Procrustes problem, which allows for the 3D position and orientation of a sparse object, with a known configuration of radio-opaque markers, to be determined from the projected locations of

these markers as registered on x-ray film. For intra-operative or dynamic applications, the use of an x-ray image intensifier (XRII) or a digital flat-panel (FP) detector required. A key component of localizing a sparse object in 3D from a single perspective projection is the measurement of the projected marker locations from the 2D projection images. A fully automated algorithm capable of identifying and localizing the position of each projected marker from projection images is therefore necessary for dynamic or real-time tracking applications.

The following study investigates the feasibility of applying the projection-Procrustes registration to track objects in 3D space during an interventional procedure. The design and implementation of the software, which performs the 3D localization and tracking of sparse objects from a sequence of projection images, is presented. The implementation includes automated means of identifying and measuring the locations of the markers of the sparse object as they appear on 2D projections, and 3D-to-2D registration by solution of the projection-Procrustes problem. Validation and testing of the technique are performed through means of *in vitro* experiments to determine the accuracy of both localizing and tracking a sparse pointer tool from single-perspective projections. The terminology recommended by the International Standards Organization (ISO) was followed in describing the accuracy of a measurement in terms of its 'trueness', sometimes referred to as bias, and its 'precision' relating to the repeatability or reproducibility of measurement.<sup>26</sup> In addition, two x-ray C-arm imaging systems are utilized for image acquisition: one equipped with an XRII, and another with a FP detector, to explore the strengths and limitations of both detector technologies with regard to the task at hand.

## 2.2 Methods

### 2.2.1 Overview of the projection-Procrustes Registration

The generalized solution of the orthogonal Procrustes registration problem is well established,<sup>27</sup> and defines the optimal transformation that aligns two corresponding 3D point sets in a least-square sense. Projection-Procrustes registration couples projection equations, derived from the perspective geometry of a single-plane radiography system, with Procrustes registration techniques to determine the 3D pose (i.e. position, and orientation) of a sparse object from a single projection view.<sup>22</sup> A sparse object is any object containing a sparse, and rigidly affixed configuration of markers. For purposes of radiography, it is important that these markers be radio-opaque in nature such that their projections have a significant amount of contrast within the radiograph (i.e. radio-opaque objects have high electron densities, which results in higher x-ray attenuation and therefore contrast within the radiograph).

The projection-Procrustes registration process differentiates between three separate coordinate systems (**Figure 2-1**): a 2D image coordinate system,  $uv$ , a 3D world coordinate system,  $xyz$ , and a 3D local object coordinate system,  $x'y'z'$ . The world coordinate system can be arbitrarily placed within the space of the imaging system. The world coordinate system is the common reference from which all others will be mapped, and is also the coordinate system in which the perspective geometry of the radiography system is defined. The local object coordinate system is relative to the sparse object itself, and describes the relative 3D locations of each marker contained within the object. The image coordinates  $(u_i, v_i)$ , of a marker projection upon the image plane, are directly

related to 3D position of the marker,  $P_i(x_i, y_i, z_i)$ , within the 3D world coordinate system by the following relationship:

$$u_i = (x_i) * D / (z_i) \quad (1)$$

$$v_i = (y_i) * D / (z_i) \quad (2)$$

where  $D$  is the focal length of the radiography system. While this relationship would be the case in an ideal imaging system (i.e. no noise or image distortion, infinitely small focal spot, etc.), in practical applications measurements of the image coordinates  $(u_i, v_i)$  of the marker projections will contain errors that arise from image noise and geometric distortion in the detector.

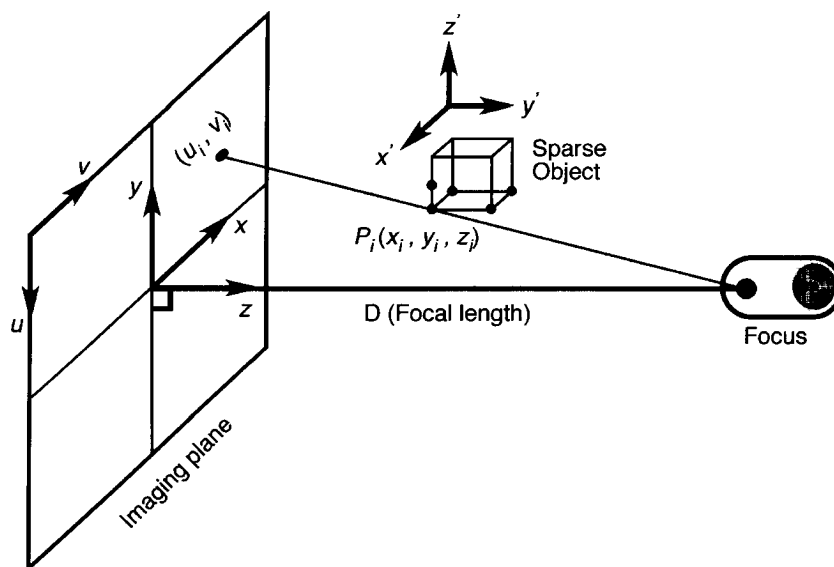


**Figure 2-1:** Coordinate systems defined in projection-Procrustes registration problem. The world coordinate system,  $xyz$ , in which the perspective geometry is defined, the image coordinate system,  $uv$ , describes the image space, and the object coordinate system,  $x'y'z'$ , describes the relative positions of each marker within the sparse object.

The projection-Procrustes registration technique maps the local object coordinate system into the world coordinate system by utilizing the 2D information derived from the projection image to constrain the registration problem. The position of a sparse object marker within the object coordinate system,  $P'_i$ , is related to its position within the imaging coordinate system,  $P_i$ , by the following transformation.

$$P_i = [R]^T P'_i + t \quad (3)$$

Where  $[R]^T$  is the transpose of the rotation matrix, and  $t$  is the translation that relates the origins of both coordinate systems. Ideally, the registration should result in a transformation that aligns the centre of each marker of the sparse object with its corresponding projection line (i.e. the line running from the centre of the marker projection within the 2D image to the focal spot of the x-ray system – **Figure 2-2**). Realistically, the markers will not align perfectly with their corresponding projection line due to errors that arise during the measurement process. Therefore, an optimization problem must be solved that finds the transformation that minimizes the alignment errors about all points used in the registration (i.e. marker centres).

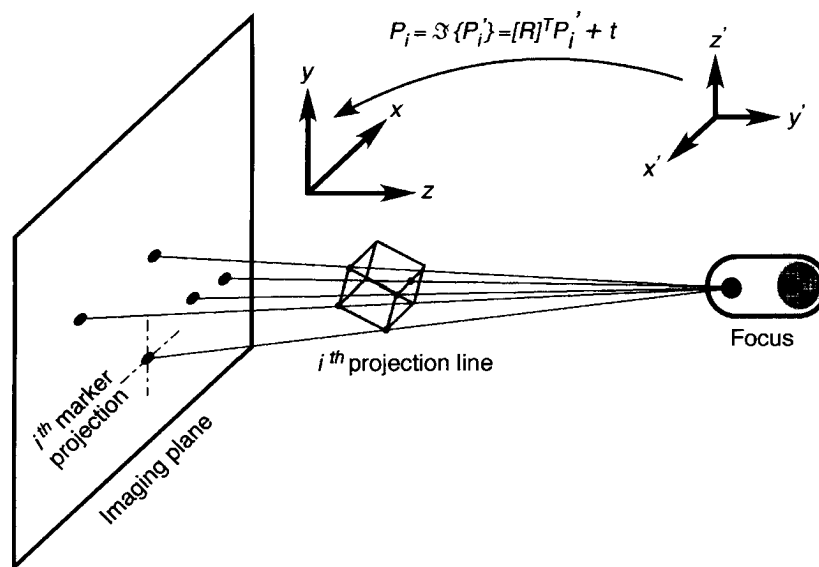


**Figure 2-2:** Optimal alignment of sparse object marker with their corresponding projection lines. In an ideal situation, where no noise or geometric distortion is present and the locations of the marker projections upon the image can be measured without error, the minimal distance between each marker and its corresponding projection line is zero.  $\mathcal{S}\{P'_i\} = [R]^T P'_i + t$ , is the transformation that relates the position of the markers within the local object coordinate system,  $x'y'z'$ , to their position within the three-dimensional world coordinate system,  $xyz$ , after optimal alignment.

### 2.2.2 Algorithm Overview

The structure of the algorithm that tracks sparse objects in 3D space from their projections in 2D digital radiographs is presented in **Figure 2-3**. The following sections summarize the function of each module, and describe the techniques used to provide functionality. The algorithm requires several inputs: a sequence of digital radiographs, parameters describing the geometry of the perspective radiography system used to acquire the digital radiographs, and the rigid-body coordinate file describing the relative 3D locations of the markers comprising the sparse object within a local coordinate system. All software was developed in C++ and ran on a personal computer equipped with a 2.0 GHz processor and 1 GB of memory.

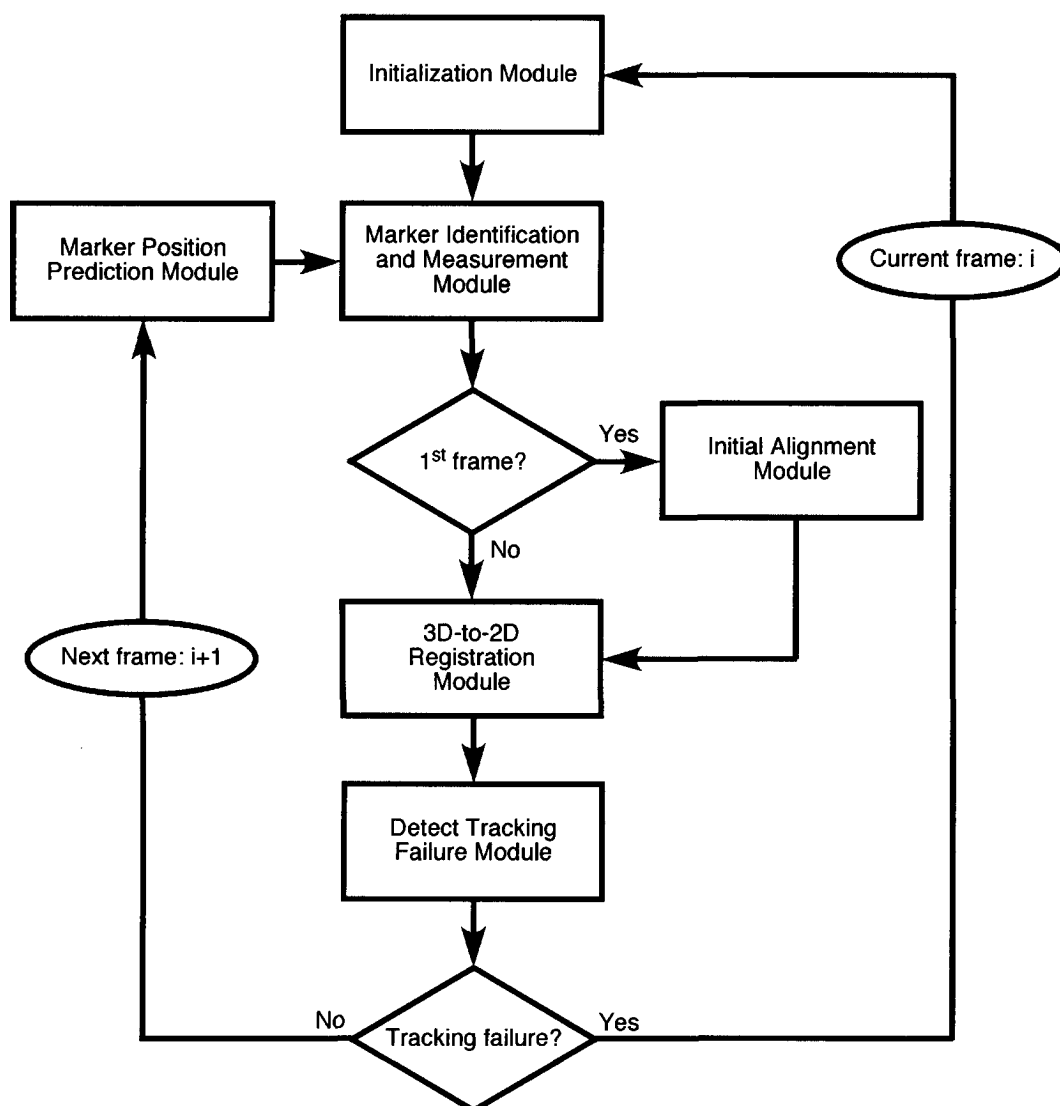


**Figure 2-3:** Flow chart of algorithm for 3D tracking of sparse objects from 2D digital radiographs

#### *Initialization Module*

The initialization module provides three functions: the first is to initialize the location of marker projections as they appear in the image frame; the second establishes correspondence between each marker described by the rigid body model and their projections within the image frame; and the third is to acquire parameters that describe the size of each marker. All of this is accomplished through user interaction. The image

frame input into the initialization module is loaded onto an interactive display (i.e. computer display and mouse). The software prompts the user to select the image location of each marker projection in the order corresponding to the list of 3D coordinates of the markers described in the rigid body file. This initializes the location of each marker projection as well as establishing correspondence between the markers in the 3D rigid body file and their respective projection within the image. The software additionally prompts the user to enter the radius of each marker. It is assumed that all markers within the sparse object are spherical in shape, and therefore a single parameter (i.e. the radius) is sufficient to describe the size of the marker. This parameter will be used in the marker identification and measurement module to aid in positive marker identification. Note, that initialization is only required for the first frame of a multi-frame image sequence, or if tracking failure is detected, in which case the algorithm has failed and must re-initialize beginning at the frame where tracking failure occurred.

#### *Marker Position Prediction Module*

The marker position prediction module serves an important function: predicting the location of each marker projection within the next frame of the image sequence from their locations in previous frames. This function is important for two reasons: it helps maintain correspondence between the 3D rigid body file and the marker projections throughout an image sequence, and it substantially reduces the search region of the marker identification and measurement module, which leads to significant savings in processing time. Even a highly optimized detection algorithm requires a significant amount of CPU time to search an entire image frame.<sup>28</sup> By using the predicted locations determined within the marker position prediction module, only a local region surrounding

the predicted location is searched in order to identify and measure the location of marker projection within the image frame.

Predicting the location of marker projections in new frames is accomplished by linearly extrapolating the 3D positions of markers determined from previous imaging frames. Linear extrapolation uses the two most recent samples to find the sparse object velocity, and predicts that it will maintain a constant velocity until the next frame.<sup>29</sup> The predicted 3D location of the markers in the world coordinate system is given by the following formula,

$$x_f = 2x_{f-1} - x_{f-2} \quad (4)$$

where  $x_{f-1}$  is the 3D position of markers within the world coordinate system determined from the previous image frame, and  $x_{f-2}$  is the 3D position of markers within the world coordinate determined from second past image frame. The predicted 3D location of the markers,  $x_f$ , must then be projected onto the imaging plane using a perspective projection, based upon the known geometry of the perspective radiography system.

Although there are numerous techniques to predict motion,<sup>29</sup> linear extrapolation was chosen due its simple implementation, and some assumptions made regarding the imaging modality and the intended applications. It was assumed that a high temporal resolution (i.e. 15 or 30 fps) would be employed during acquisition of the images, and that although the velocity of the sparse object may not be constant throughout the entire acquisition, its acceleration during a small time interval (encompassing several imaging frames) would be minimal. The assumption of constant velocity was therefore deemed to be adequate for providing a robust prediction result.

### *Marker Identification and Measurement Module*

The marker identification and measurement module finds all possible marker projections within each local search region, identifies that corresponding to the actual marker projection, and measures its location within the image frame. The structure of the module is presented in **Figure 2-4**. A square search window of size  $s \times s$  pixels, where  $s$  is set empirically, is centered at the predicted marker position determined in the previous module. In the case where the previous module was the initialization module, each search window is centered about the locations selected by the user.

The search window is convolved with an inverted Laplacian of a Gaussian (LoG) convolution kernel, also referred to as a Mexican hat convolution kernel, that performs both edge enhancement and image smoothing when convolved with an image. The implementation of the inverted LoG kernel is based upon the implementation of the LoG within Matlab (The Mathworks Inc., MA, USA). The implementation of the LoG kernel in Matlab is described by the following function,

$$h_g(i, j) = e^{-(i^2 + j^2)/(2\sigma^2)} \quad (5)$$

$$h(i, j) = \frac{(i^2 + j^2 - 2\sigma^2)h_g(i, j)}{2\pi\sigma^6 \sum_i \sum_j h_g} \quad (6)$$

and produces a normalized LoG convolution kernel (i.e. the summation of all elements within the kernel is equal to one). The variables  $i$  and  $j$  refer to the rows and columns of the convolution kernel respectively. The variable  $\sigma$  is the Gaussian standard deviation.

The dimensions of the inverted LoG kernel are set to be proportionate to the radius of the marker to be identified within the search window, and value for  $\sigma$  is set empirically.

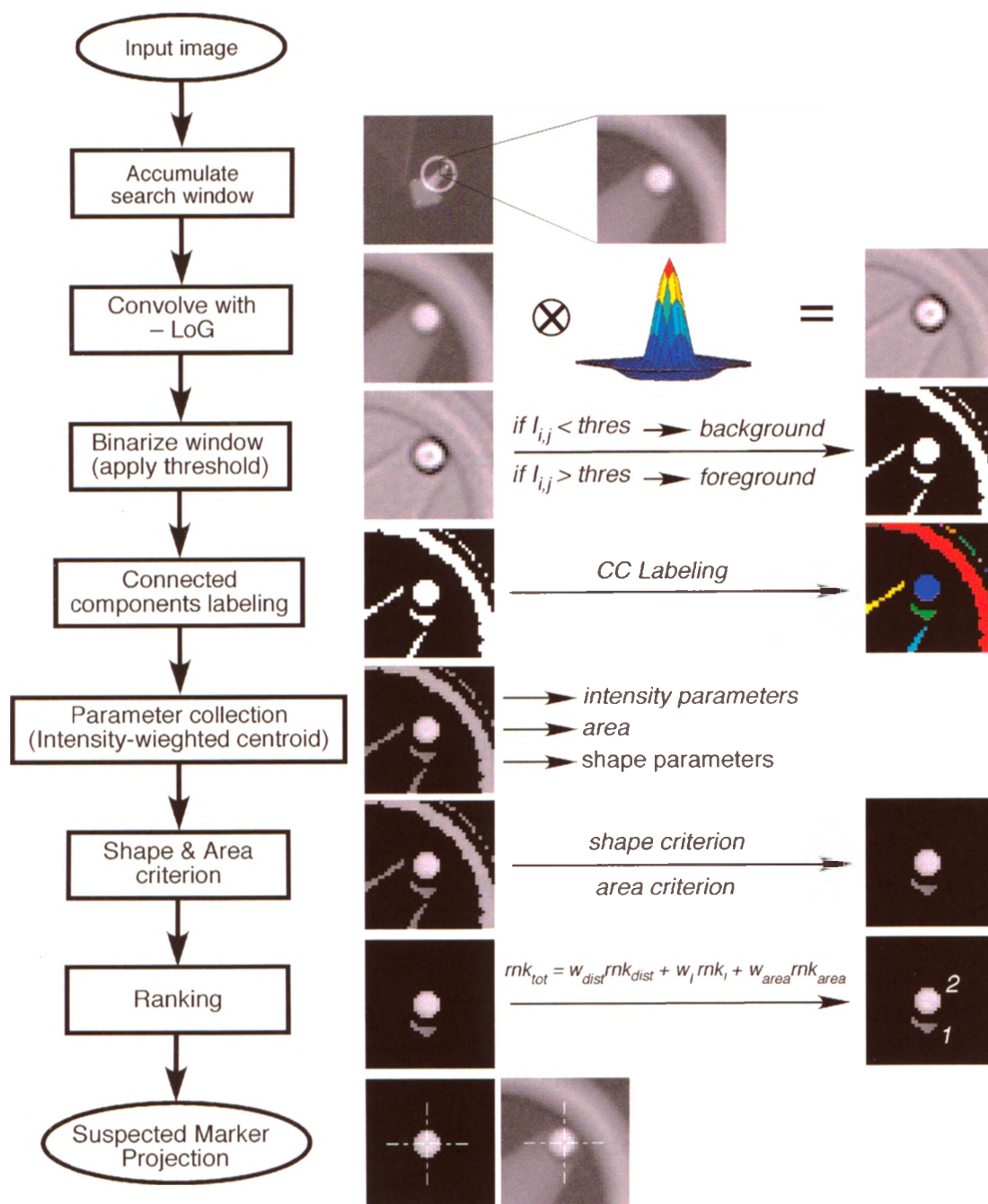


Figure 2-4: Flow chart of marker identification and measurement module, and example images processed.

After LoG convolution, the search window is binarized using a threshold calculated from the intensity values of the convolved search window. The maximum gray level ( $gl_{\max}$ ) within the search window is located. The pixels in an area approximately equal to the magnified cross sectional area of the sparse object markers, and centered about the  $gl_{\max}$ , are visited to find a local minimum gray level ( $gl_{\min}$ ). A threshold for the search window is calculated as follows

$$thres = gl_{\min} + \gamma(gl_{\max} - gl_{\min}) \quad (7)$$

where the parameter  $\gamma$  is set empirically. Pixels within the search window that have an intensity higher than the threshold are set to the foreground, while those with lower intensities are assigned to the background level. It is assumed that the markers of the sparse object will be made from a radio-opaque material; therefore their projections within a digital radiograph will be bright.

The foreground pixels of the resulting binarized search window are partitioned into connected components using an efficient connected components labeling algorithm.<sup>30</sup> The algorithm differs from the classical approach by handling equivalences during the first scan through the image (or in our case the search window) by merging equivalent classes as soon as a new equivalence is found. The connected components labeling algorithm implemented within the marker identification and measurement module uses 4-connectivity. Further details regarding the connected components labeling algorithm can be found in Di Stefano et al.<sup>30</sup>

Each component labeled within the search window is considered as a possible marker projection. Several parameters describing each component are gathered including

its area in pixels, the outermost  $i$  and  $j$  dimensions of the component, and several intensity-based parameters. The intensity-weighted centroid of each component is calculated using the pixel intensities of the original image as follows:<sup>31</sup>

$$i_c = \frac{\sum_{i,j} i \times I_{i,j}}{\sum_{i,j} I_{i,j}} \quad (8)$$

$$j_c = \frac{\sum_{i,j} j \times I_{i,j}}{\sum_{i,j} I_{i,j}} \quad (9)$$

The intensity-weighted centroid is calculated over all pixels within a component, where  $i$  and  $j$  are the coordinates of the pixels in the component, and  $I_{i,j}$  is the intensity of pixel  $i,j$ .

Once the parameters describing each labeled component within the search window have been gathered, each possible marker projection (i.e. labeled component) is subject to area and shape criteria. The area criterion is based upon the known cross-sectional area of the marker (calculated from the radius or each marker input during initialization), the pixel spacing of the image, and the approximated geometric magnification. If the area occupied by a component is outside a specified range, then it is discarded as a possible marker projection. The shape criterion is based upon the known spherical shaped of each marker and its radius. The distance from the calculated intensity-based centroid to the outermost pixels of the component is determined and compared to the magnified radius of the marker. If any of these distances is greater than the magnified radius, then that component is discarded as a possible marker projection.

The remaining components that have satisfied both the area and shape criterion are subjected to a weighted-ranking to determine which has the highest probability of being the actual marker projection.<sup>28</sup>

$$rnk_{tot} = w_{dist}rnk_{dist} + w_I rnk_I + w_{area}rnk_{area} \quad (10)$$

The total rank,  $rnk_{tot}$ , of a possible marker projection is based upon its several sub-rankings. These sub-rankings are calculated as follows.

i) Distance rank -  $rnk_{dist}$ : is based on the distance of each component to the predicted marker location (determined in the marker position prediction module). The component that is closest the predicted location receives the highest distance ranking.

ii) Intensity similarity rank -  $rnk_I$ : is based on the closeness in average intensity between a possible marker projection and the corresponding marker projection successfully identified in the previous image frame. The component with the average intensity closest to the corresponding maker successfully identified in the previous frame, receives the highest similarity ranking.

iii) Area similarity rank -  $rnk_{area}$ : is based on the closeness in area (i.e. number of pixels) between a possible marker projection and the corresponding marker projection successfully identified in the previous image frame. The components with an area closest to the corresponding maker successfully identified in the previous frame, receives the highest area similarity ranking.

The variables  $w_{dist}$ ,  $w_I$ , and  $w_{area}$  are the weighting factors assigned to each respective sub-ranking. The weighing factors are assigned empirically such that their sum is equal

to one. The component within the search window that has the highest total rank,  $rnk_{tot}$ , is identified as the actual marker projection belonging to its corresponding marker within the 3D rigid body model. Its intensity-based centroid and other parameters collected during the module are retained for future use.

### *Initial Alignment Module*

This module automatically provides an initial estimate of the six degree-of-freedom (DOF) pose of the sparse object for the first frame of an image sequence, as a starting point for the 3D-to-2D registration. Translations occurring parallel to the image plane (i.e. in-plane, x-y-direction) are initialized using the mean position of the measured centres of the marker projections (intensity-weighted centroids determine in previous module). The translation orthogonal to the image plane (i.e. out-of-plane, z-direction) is determined by estimating the magnification of the sparse object from the image. Rotations are initialized by iteratively rotating the rigid body model of the sparse object in  $90^\circ$  increments to find the orientation that minimizes the distance between the measured centres of the marker projections, and position of the points of rigid body model projected onto the imaging plane after the applied transformation. Note, that the initial alignment module is only executed for the very first image in a sequence. The starting point for all subsequence image frames is set using the final six DOF pose determined from the 3D-to-2D registration performed upon the previous image frame in the sequence.

### *3D-to-2D Registration Module*

The 3D-to-2D registration module is an iterative and optimized solution to the projection-Procrustes registration problem. The implementation of the registration

algorithm has previously been described by Hoffmann et al.,<sup>22</sup> and Habets et al.<sup>25</sup> The algorithm requires three sets of points: the rigid body file that describes the 3D location of each marker within its local coordinate system, the corresponding locations of the 2D marker projection centroids mapped into the 3D world coordinate system, and the 3D position of the x-ray focal spot within the 3D world coordinate system. Projection lines are defined between each of the 2D marker projection centroids and the 3D x-ray focus. The 3D pose of the rigid body points is iteratively modified until an optimized alignment between each point and its corresponding projection line is achieved. The criterion used to optimize the alignment is the minimization of the perpendicular distance between each marker and its corresponding projection line. This distance is defined as

$$d_i = |P_i - (P_i)_p| \quad (11)$$

where  $(P_i)_p$  is the projection of the  $i$ th point of rigid body,  $P_i$ , onto its corresponding projection line. This projection is given by

$$(P_i)_p = [P_i \cdot \hat{l}_i] \hat{l}_i \quad (12)$$

where  $\hat{l}_i$  is the unit vector that defines the direction from the  $i$ th 2D centroid to the x-ray focus. Best fit is achieved when the difference between the 3D poses of subsequent iterations is below a predefined threshold, or a maximum number of iterations is performed. Further details regarding the projection-Procrustes registration algorithm can be found in Hoffmann et al.,<sup>22</sup> and Habets et al.<sup>25</sup>

### *Tracking Failure Detection Module*

This module detects whether a tracking failure has occurred, and if so it notifies the user, and re-initiates the tracking process beginning at the failed image frame. If any one of the following conditions is not met, then it is deemed that tracking failure has occurred.

i) The number of marker projections successfully identified must be greater than or equal to four. If less than four marker projections are successfully identified then it is not possible to find a unique solution to the 3D-to-2D registration problem.

ii) The registration error, resulting from the 3D-to-2D registration, must be less than a predefined threshold. The registration error is calculated as the difference between the 3D points of the rigid body file, re-projected onto the image plane after the iterative registration process, and the measured centres of the marker projections within the image. If the registration error is unreasonably large (i.e. above the threshold) then registration process achieved sub-optimal results.

iii) The absolute motion of the sparse object between subsequent frames must be less than a calculated threshold. Since, the temporal resolution of the image acquisition is known, and the velocity of the sparse object can be approximated, it is possible to estimate the extent of movement of the sparse object between subsequent frames. If the absolute motion of the sparse object between subsequent frames is above the calculated threshold, then this is an indication that the registration results are erroneous.

### 2.2.3 Phantoms

The validation and testing of the above-presented tracking technique was performed through a series of *in vitro* experiments. Two phantoms were fabricated for the *in vitro* experiments: an acrylic plate containing a regularly spaced grid of hemispherical divots on its surface, and a stylus-like phantom used to mimic the function of a pointer tool (**Figure 2-5**). The divots on the grid phantom, machined on a numerical mill with a ball-end cutter, have a diameter 3.18 mm and are spaced at  $20 \pm 0.050$  mm intervals. The stylus phantom is a sparse object comprising of two rigidly attached components: an acrylic cube with five implanted tungsten-carbide (TC) ball bearings (BB), each with a diameter of 1.59 mm; and an acrylic pointer, 85 mm in length with a 3.18 mm in diameter, stainless steel BB rigidly attached to its end, which acts as a tool tip. The BB's in the acrylic cube are arranged in a known manner. Four of the BB's are situated at the lower vertices of the  $20 \times 20 \times 20 \text{ mm}^3$  cube and the fifth is offset 10 mm from one vertex. TC BB's were used within the phantom to maximize the contrast between the markers and the background, while being compact and symmetric to maintain x-ray flux independent of marker orientation relative to the x-ray source. The stylus phantom was scanned on a GE Explore Locus Ultra micro-CT scanner at 120 kVp, 20 mA, and an isotropic voxel spacing of  $150 \text{ }\mu\text{m}$  to geometrically characterize the locations of each BB (i.e. to generate the rigid-body file required for algorithm input). The centroid of each BB was determined to sub-voxel accuracy using the semi-automatic centroiding algorithm available in the GE MicroView software package.

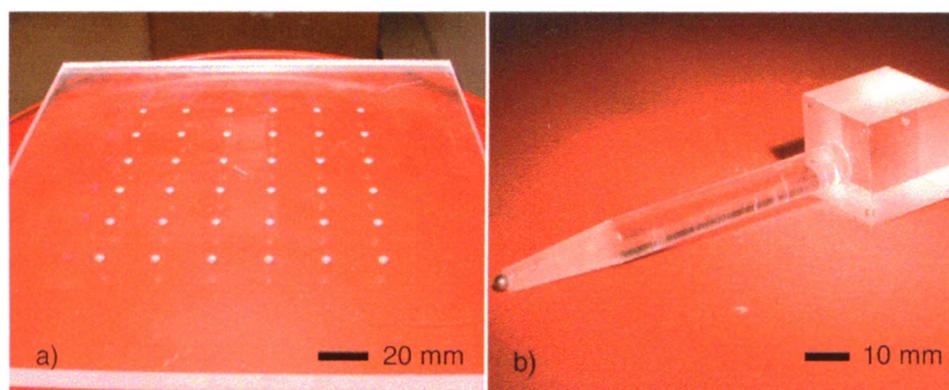


**Figure 2-5:** Phantoms manufactured for *in vitro* experiments: a) Grid phantom, manufactured from an acrylic plate, contains hemispherical divots; b) Stylus phantom, made to mimic function of a pointer tool.

### 2.2.5 Assessment of Accuracy and Precision

In image-guided procedures, it is important to measure the accuracy and precision of localizing point targets in 3D space.<sup>32,33</sup> The procedure used to assess the accuracy and precision of localizing targets, using the stylus phantom and single-perspective projections, is similar to that described by West et al.,<sup>33</sup> who applied it to optically tracked tools. A subset of divots (i.e. targets) within the acrylic grid phantom was selected for the assessment. The tool tip of the stylus phantom was placed at a random orientation in each of the selected divots, the grid phantom being kept stationary throughout the experiment. At each divot location a series of 30 measurements of the 3D location of the tool tip was obtained. Accuracy was assessed using the root-mean-square (RMS) target registration error (TRE) obtained from registering the measured tool tip locations to the known geometry of the grid phantom, which was provided by its CAD model. The registration between the measured tip locations and the CAD model of the grid phantom was performed five times using measurements selected randomly out of the thirty acquired at each divot locations. The mean result of the RMS TRE across the five trials was used to

quantify accuracy. Precision was assessed as the mean of the standard deviation (SD) of the 30 repeated measurements of the tool tip location obtained at each divot location.

This procedure was performed on both an XRII-based radiography system, and a radiography system equipped with a FP detector for comparative purposes (see sections §1.3.1 & §1.3.2). The image acquisition, measurement, and registration procedure was performed twice upon each radiography system: first with images acquired in the anterior-posterior (AP) view, and again with images acquired in the left-anterior-oblique (LAO) view. A Siemens Multistar x-ray C-arm unit, equipped with an x-ray image intensifier (XRII), and a GE Innova 4100 x-ray C-arm unit, equipped with a flat-panel (FP) detector, were the two radiography systems utilized for image acquisition purposes. The perspective geometry of the Siemens Multistar had been well characterized in previous studies that utilized this specific radiography system for computed tomography acquisitions.<sup>34,35</sup> This previous knowledge was utilized to establish the relationship between the image plane and the world coordinate system, and establish the 3D location of the x-ray focus. A 3 x 3 subset of divots was selected for the assessment performed with the Multistar. Projections were acquired on the Multistar (equipped with an XRII) using a 280 mm field of view (FOV), a potential of 90 kVp, and exposure of 1 mAs (**Figure 2-6a,b**). These acquired projection have a matrix size of 440 x 440, an isotropic pixel spacing of 0.54 mm, and a pixel depth of 10 bits. Bright-field correction and geometric distortion correction were applied to all images acquired on the Multistar to correct for the non-uniformities of the XRII.<sup>34,36</sup>

The perspective geometry of the GE Innova 4100 was reconstructed by acquiring images of a commercial Radiostereometric Analysis (RSA) calibration cage (Lund Knee

Box, RSA Biomedical, Umea, Sweden). These images were processed using commercial RSA software (UmRSA, RSA Biomedical, Umea, Sweden) to establish the transformation between the image and world coordinate systems, and to determine the 3D position of the x-ray focus (see section §1.4.4). A 4 x 4 subset of divots was selected for the assessment performed with the Innova 4100. Projections were acquired on the Innova 4100 (FP detector) using a 200 mm FOV, a potential of 50 kVp, and an exposure of 3 mAs (**Figure 2-6c,d**). These acquired projections have a matrix size of 1000 x 1000, an isotropic pixel spacing of 0.2 mm, and a pixel depth of 12 bits.

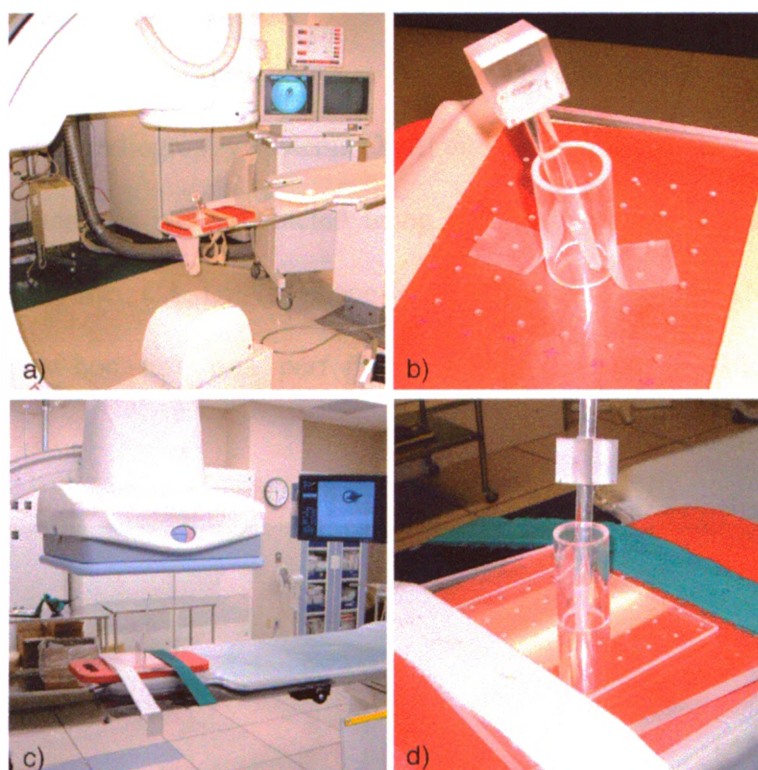


**Figure 2-6:** Experimental setup for assessment of accuracy and precision: a) Siemens Multistar C-arm equipped with x-ray image intensifier (XRII) with phantoms inside field of view (FOV). b) Close-up of phantom setup within FOV of XRII. c) GE Innova 4100 C-arm with flat-panel (FP) detector with phantoms inside the FOV. d) Close-up of phantom setup within FOV of the FP detector.

In addition to the assessments performed upon the radiography systems, an additional assessment was performed using an optical tracking system (OTS) (Polaris Vicra, Northern Digital Inc., Waterloo) to provide a standard of comparison. OTS are very robust, and are typically the preferred tracking system for computer-aided surgery suites. The Vicra has a manufacturers stated accuracy of 0.25 mm. A passive optical tracking frame was manufactured, characterized, and rigidly attached to the stylus phantom (**Figure 2-7a**). A 4 x 4 subset of divots upon the grid phantom was used for the assessment, and 30 measurements of the tool tip were obtained at each divot location using the optical tracking system (**Figure 2-7b**). Accuracy and precision were quantified in the same manner as outlined above. To compare the results of the assessments performed using the radiography systems (XRII and FP), with those performed using the OTS, statistical analysis was conducted using a statistics software package (Prism 4, GraphPad Software Inc., CA, USA). A one-way analysis of variance (ANOVA) followed by a Tukey post-hoc test was performed to identify any statistically significant differences.

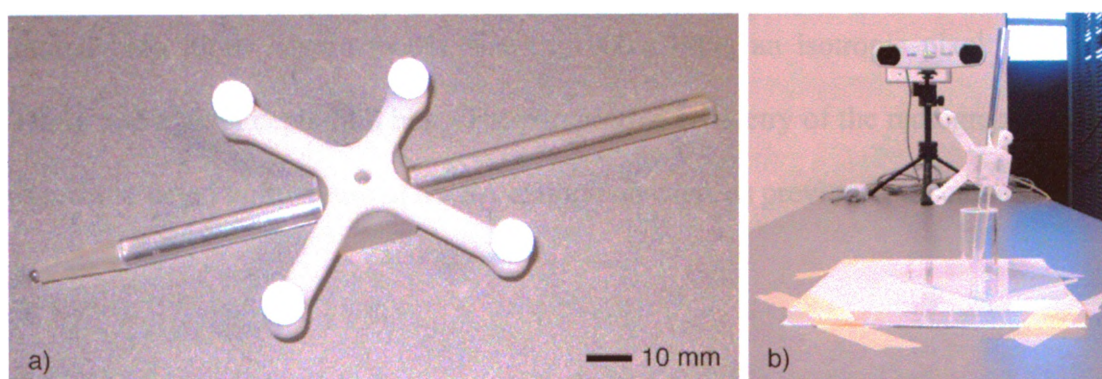


**Figure 2-7:** Assessment of accuracy and precision using an optical tracking system: a) Passive optical tracking frame rigidly attached to stylus phantom. b) Stylus phantom secured in a divot of the grid phantom. The location of the stylus is measured by the optical tracking system via the passive optical tracking frame attached to the stylus.

### 2.2.6 Dynamic Tracking Assessment

To provide a proof-of-principle demonstration of the technique and its ability to track sparse objects from single-perspective projections, a dynamic tracking assessment was performed. For the dynamic tracking experiment an anatomical skull phantom was implanted with six tantalum BBs, each 1 mm in diameter. A CT scan of this phantom was acquired on a 64 slice clinical CT scanner at 120 kVp, 400 mA, and a voxel spacing of  $0.488 \times 0.488 \times 0.625$  mm, from which the locations of the BBs were determined to sub-voxel accuracy. During the tracking experiment, several point targets within the skull phantom were localized sequentially with the tool tip of the stylus phantom while it was simultaneously tracked using single-perspective projections, acquired at a rate of 15fps using the FP radiography system (GE Innova 4100), as well an OTS (NDI Polaris Vicra) that recorded the position a rigidly attached passive optical tracking frame at a frequency of 20 Hz (**Figure 2-8**). The perspective projections were acquired using a cine acquisition (15 fps), a 200 mm FOV, an x-ray potential of 65 kVp, and a low exposure of 0.1 mAs, which was used to mimic the low dose levels of a fluoroscopic acquisition. The acquired projections have a matrix size of  $1000 \times 1000$ , an isotropic pixel spacing of 0.2 mm, and a pixel depth of 8 bits. The perspective geometry of the radiography system was reconstructed through use of a RSA calibration cage, as previously discussed.

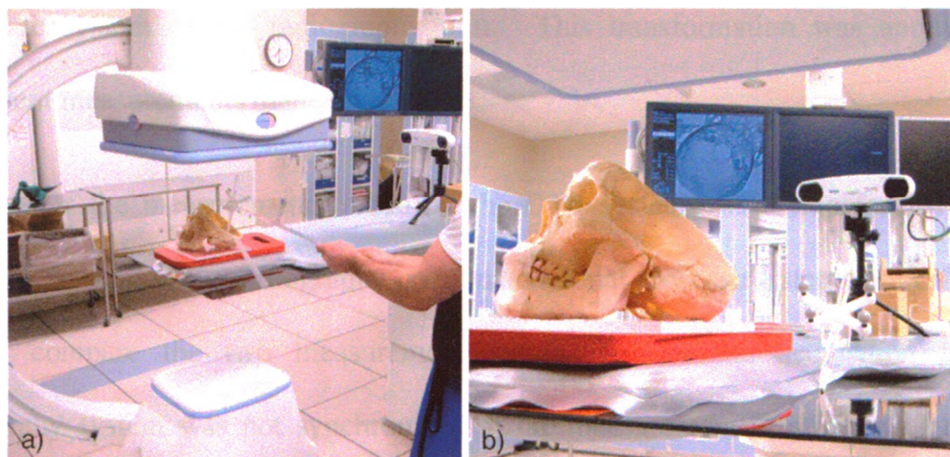


**Figure 2-8:** Setup of dynamic tracking experiment: a) localization of point targets within the skull phantom with tool tip of stylus phantom. b) Stylus phantom with rigidly attached passive optical tracking frame. Stylus was simultaneously tracked using the single-perspective projections, and optical tracking system.

In order to use the measurements made by the OTS to validate the tracking by means of single-perspective projections, it was necessary to map the 3D measurements made from both the single-perspective projections, and the OTS into a common coordinate system. To do this, the stylus was placed at five locations within the volume defined by the overlap between the FOV and tracking volume of the FP C-arm and OTS, respectively. At each location, 30 measurements of the 3D position of the tool tip of the stylus were made using both the OTS, and single perspective projections acquired on the FP radiography system. These projections were acquired using a 200 mm FOV, an x-ray potential of 50 kVp, and an exposure of 3 mAs. The mean position of the measurements obtained at each location was used to generate two point sets: one within the coordinate system of the OTS, and the other in the radiography system's frame of reference. A rigid, 3D-to-3D, point-based registration was performed between the two corresponding point sets to determine the transformation that aligned the coordinate system of the OTS to the

coordinate system of the radiography unit.<sup>27</sup> This transformation was applied to all subsequent measurements made by the OTS.

After the measurements made by the OTS systems were transformed into the coordinate system of the radiography unit, an additional processing step was performed to directly compare the two measurement sets. Because the acquisition from the radiography system was not synchronized to the measurement acquisition of the OTS, and because each system acquired data at different frequencies, it was necessary to resample each measurement set to a higher sampling frequency, and to synchronize them to common start points. To resample, and synchronize the two measurement sets, a linear interpolant was fit to each using curve fitting software (Matlab curve fitting toolbox, Mathworks Inc., MA, USA). The resulting piecewise curves were each resampled to a frequency of 60 Hz, and the time shift required to synchronize them was found by minimizing the distance between common points identified in each curve. The resampled and synchronized data were used to validate the position of the tool tip of the stylus throughout the tracking experiment, from which the RMS difference between the tracked positions of the tool tip of the stylus as measured by the OTS, and from the acquired single-perspective projections was determined.

### 2.2.7 Visualization

Visualization plays a very important role in image-guided procedures, as it is one of the primary interfaces between a patient and the interventionalist.<sup>37</sup> The purpose of visualization is to provide a realistic representation of the patient and interventional environment, and to accurately guide the interventionalist to the treatment target.<sup>37</sup> To

achieve this, visualization environments often incorporate both preprocedural and intraprocedural imaging modalities, along with tracking information. To visualize the localization of the targets within the skull phantom by the stylus during the dynamic tracking experiment, a 3D virtual environment was created to incorporate the cine projections acquired during the experiment, virtual models of the skull and stylus phantoms, and the 3D tracking data measured from the perspective projections.

The virtual environment was created using custom C++ scripts developed from open-source visualization classes<sup>38</sup> (Visualization ToolKit, Kitware Inc., NY, USA). The virtual models of the skull and stylus phantom were obtained from the CT scans that were acquired of each phantom. CT analysis software (GE MicroView) was used to extract surface models of the skull and stylus that could be uploaded into the virtual environment. The locations of the imaging plane and the x-ray source were reconstructed within the virtual environment using the data obtained from the reconstruction of the perspective geometry of the x-ray system through use of the RSA calibration cage. Because the skull phantom was implanted with tantalum BBs, its 3D pose within the world frame of reference could be determined from the acquired projection images using the above-presented algorithm (see section §2.2.2). This information was in turn used to register the surface model of the skull into the virtual environment. The surface model of the stylus phantom was registered this space using the tracking data obtained from the cine projections acquired during the dynamic tracking experiment. All of this information was combined to virtually represent the environment of the dynamic tracking experiment, and reconstruct the motion of the stylus phantom as it dynamically localized targets within the skull phantom.

## 2.3 Results

### 2.3.1 Accuracy and Precision Assessment

A summary of the results from the assessment of accuracy and precision are shown in **Figure 2-9**. Accuracy was quantified using the RMS TRE of the registrations between the measured target locations and known geometry (CAD model) of the divots upon the grid phantom. The RMS TRE associated with target measurement procedure performed using the OTS, and the XRII and FP radiography systems were better than 0.22 mm, 2.3 mm and 1.1 mm, respectively (**Figure 2-9a**). Precision was quantified using the standard deviation of repeated measures made on the 3D position of the tool tip. The precision of measurements made using the OTS, the XRII and FP radiography system were better than 0.04 mm, 0.68 mm and 0.16 mm, respectively (**Figure 2-9b**). Both the RMS TRE and the precision are plotted in terms of in-plane (i.e. measurements made parallel to the imaging plane), and out-of-plane (i.e. measurements made orthogonal to the imaging plane, in the direction joining the x-ray focal spot and detector plane).

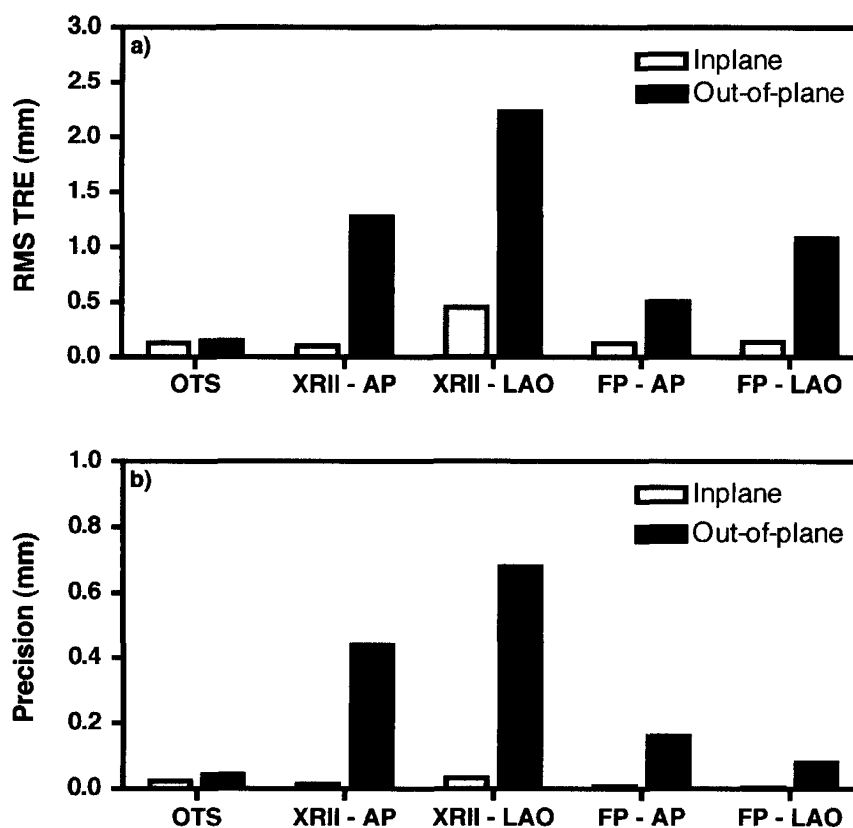


**Figure 2-9:** Summary of accuracy and precision assessment performed with the optical tracking system (OTS), and single-plane tracking using x-ray image-intensifier (XRII) and flat panel (FP), with image acquisition performed in both anterior-posterior (AP) and left anterior oblique (LAO) views. The results are reported in terms of measurements made inplane and out-of-plane. a) The root-mean-square (RMS) target registration error (TRE) of the registration between the measured tool tip locations and the known geometry of divots upon the grid phantom. b) The precision of repeated measurements made using each system. The precision was quantified using the standard deviation of repeated measurements of the location of the tool tip of the stylus.

A more detailed review of the results of the accuracy assessment is presented in **Figure 2-10**, which show the results of the statistical analysis performed to identify statistically significant differences ( $p < 0.05$ ) between the accuracy of measurements performed using the radiography systems (XRII and FP), with those performed using the OTS. The mean and standard deviation (error bars) of the TRE associated with each assessment are plotted in the in-plane (**Figure 2-10a**) and out-of-plane (**Figure 2-10b**) directions.

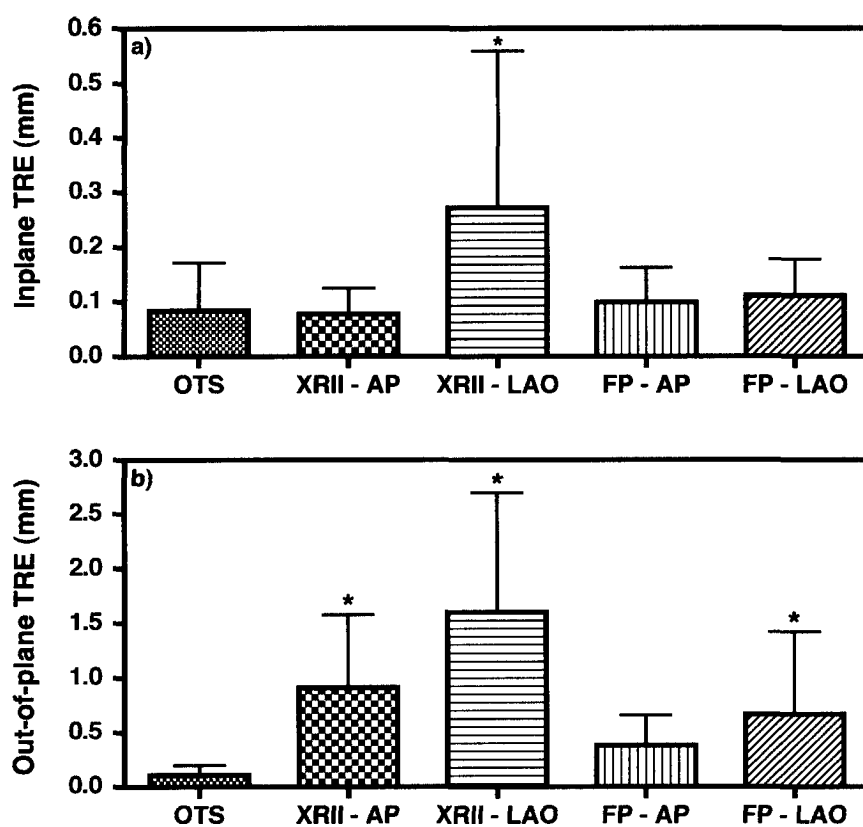


**Figure 2-10:** Statistical analysis of accuracy assessment performed on the optical tracking system (OTS), and single-plane tracking using x-ray image-intensifier (XRII) and flat panel (FP), with image acquisition performed in both anterior-posterior (AP) and left-anterior-oblique (LAO) views. Accuracy was quantified using the target registration error (TRE) of the registration between the measured tool tip locations and the known geometry of divots upon the grid phantom. a) Inplane target registration error (TRE); b) Out-of-plane TRE. \* represents a statistically significant difference ( $p < 0.05$ ) when compared to the OTS.

A more detailed review of the results of the precision assessment is presented in **Figure 2-11**, which show the results of the statistical analysis performed to identify statistically significant differences ( $p < 0.05$ ) between the precision of measurements performed using the radiography systems (XRII and FP), with those performed using the OTS. The mean and standard error (error bars) of the precision associated with each assessment are plotted in the in-plane (**Figure 2-11a**) and out-of-plane (**Figure 2-11b**) directions.

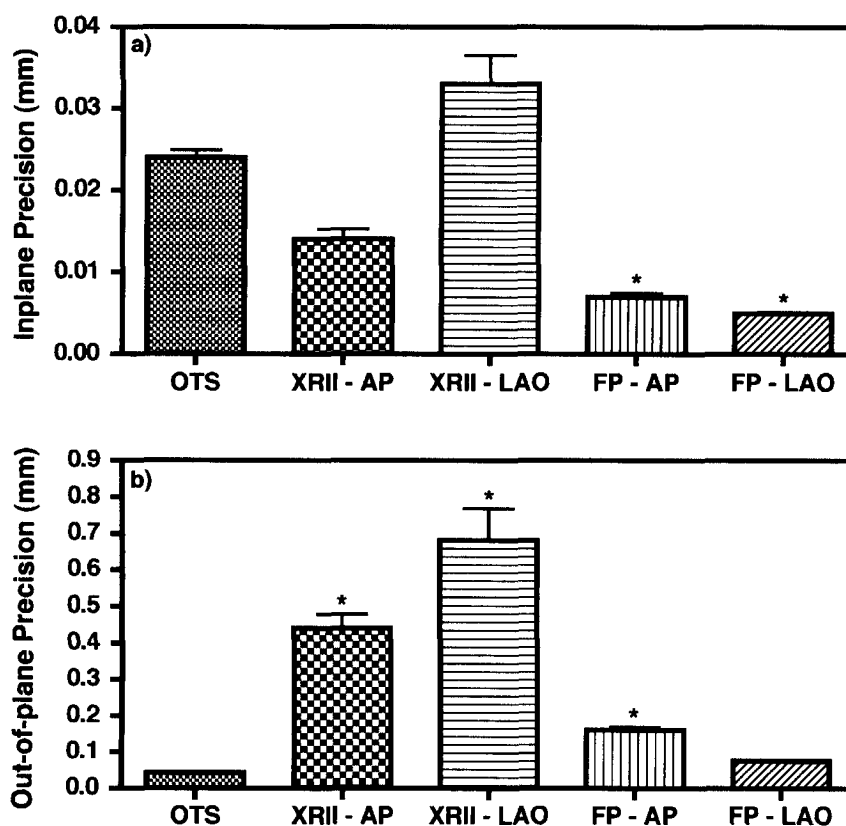


**Figure 2-11:** Statistical analysis of precision assessment performed on the optical tracking system (OTS), and single-plane tracking using x-ray image-intensifier (XRII) and flat panel (FP), with image acquisition performed in both anterior-posterior (AP) and left-anterior-oblique (LAO) views. Precision was quantified using the standard deviation of repeated measurements of the location of the tool tip of the stylus. a) Inplane precision; b) Out-of-plane precision. \* represents a statistically significant difference ( $p < 0.05$ ) when compared to the OTS.

### 2.3.2 Dynamic Tracking Assessment

The results of the dynamic tracking assessment found that the RMS tracking error, determined by comparing the trajectories of the tool tip of the stylus phantom as measured from the single-perspective projections acquired with the FP radiography system, and by the OTS (standard reference), was 2.1 mm. The trajectory of the tool tip of the stylus, as measured by both the OTS and single-plane tracking using the FP detector, is plotted as the x-translation (**Figure 2-12a**), y-translation (**Figure 2-12b**), and the z-translation (**Figure 2-12c**). The RMS error is reported for each trajectory, and was quantified using the difference between the two curves calculated at every frame.

### 2.3.3 Algorithm Performance

During the dynamic tracking experiment an image sequence, comprising approximately 450 projections, was acquired. These 2D projections were processed using the above presented algorithm (see section §2.2.2) to track the position of both the stylus and skull phantom in 3D space. The algorithm experienced a failure rate of approximately 4% (i.e. image frames in which tracking failed – see section §2.2.2) while tracking the stylus phantom from the acquired projections. A failure rate of 0% was experienced while tracking the skull phantom (which was stationary throughout). The values of the empirically set variables, as listed within the equations in section §2.2.2, employed to achieve these rates are listed in **Table 2-1**. Automatic identification of marker projections and measurement of their 2D centroids by the *marker identification and measurement module* required approximately 100 ms per frame. Calculation of the 3D pose of each phantom by the *3D-to-2D registration module* required approximately

50 ms per image frame, initialization by the users required approximately 10 seconds, and determining an initial pose of the sparse object for the first image frame by the *initial alignment module* required less than 5 seconds.

**Table 2-1:** Employed values of empirically set variables listed within the equations of section §2.2.2

Variable	Value	Description	Equation No.
$\sigma$	2.2	Gaussian standard deviation of inverted Laplacian of a Gaussian convolution kernel	5 & 6
$\gamma$	0.5	Scale factor (0 – 1) of gray level threshold	7
$w_{dist}$	0.6	Weighting factor of distance ranking	10
$w_I$	0.2	Weighting factor of intensity similarity ranking	10
$w_{area}$	0.2	Weighting factor of area similarity ranking	10

### 2.3.4 Visualization

Snapshots of the visualization of the dynamic tracking experiment are presented in **Figure 2-13** and **Figure 2-14**. **Figure 2-13** shows the reconstruction of the intra-procedural setup (i.e. projection geometry of the radiography system and location of the skull phantom) of the dynamic tracking experiment within the 3D virtual environment. The geometry of the perspective x-ray imaging system was reconstructed to include the 3D position of the 2D imaging plane, and x-ray source. The skull phantom was reconstructed using a surface model extracted from an acquired CT volume of the phantom, and its position from the tracking data determined from the single-perspective projections. **Figure 2-14** shows the localization of each of the targets within the skull phantom with the tool tip of the stylus. Frames from the acquired sequence of 2D projection images are shown within the first row of the figure, and the corresponding 3D reconstructions within the virtual environment are shown below.

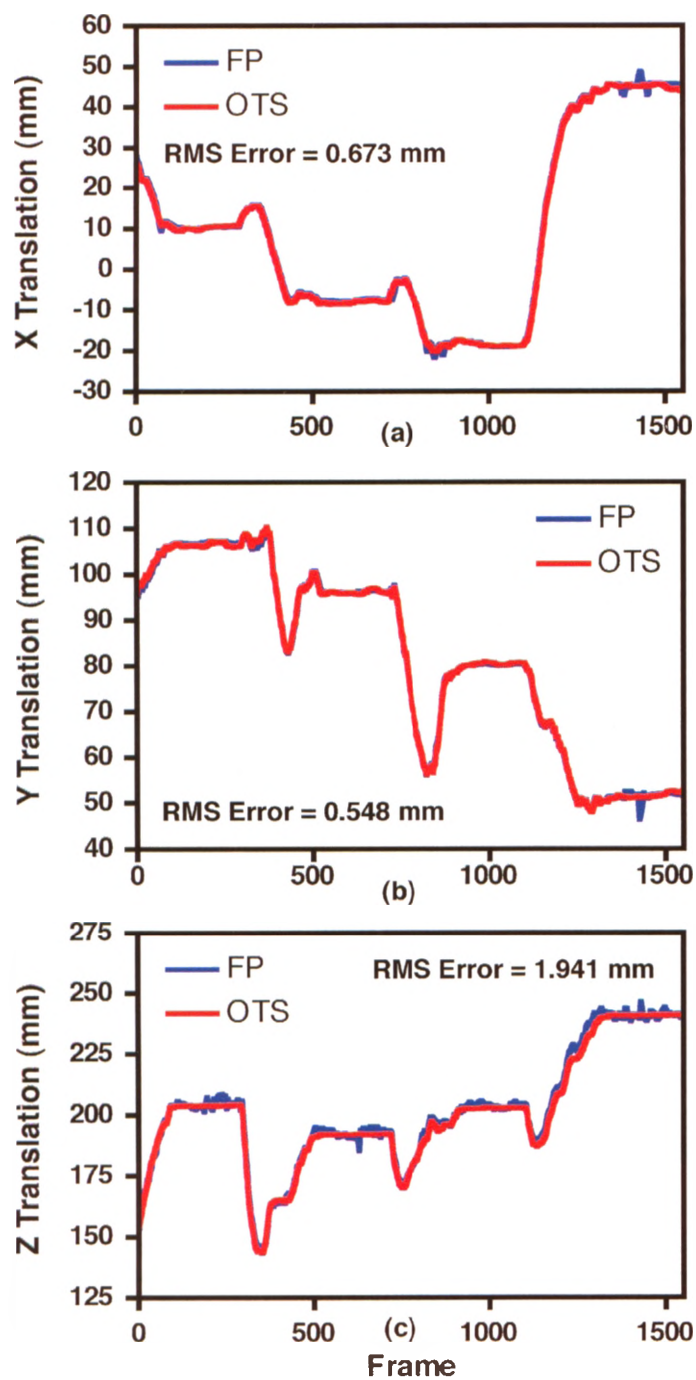


**Figure 2-12:** Assessment of dynamic tracking using optical tracking system (OTS) as standard reference to validate single-plane tracking using the flat panel (FP) detector. Comparison of the tool tip trajectory during the localization of targets within the skull phantom with the tool tip of stylus in: a) X translation, b) Y translation, c) Z translation. The root-mean-square (RMS) error is reported for each translational component. The RMS error was calculated using the differences between each curve at every frame.

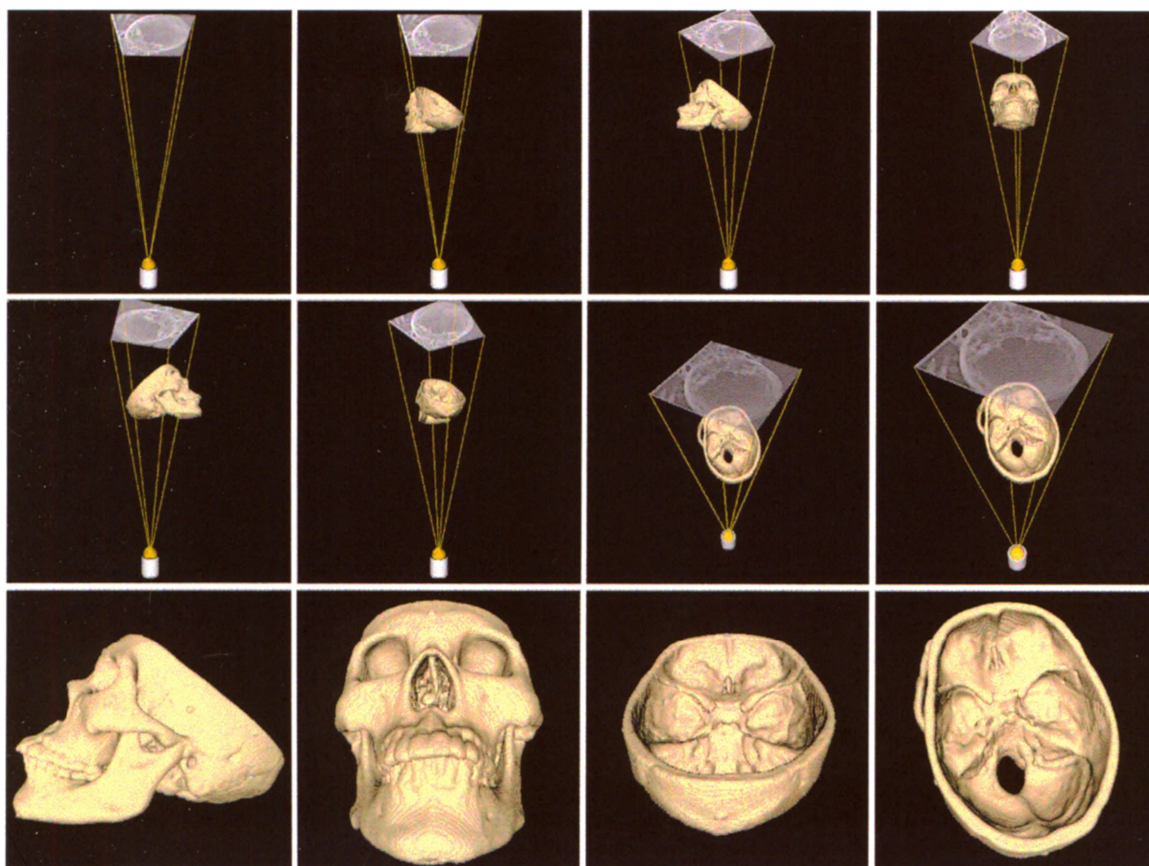


**Figure 2-13:** Snapshots of the 3D virtual environment at various camera angles, showing the projective geometry of the perspective x-ray system, respective positions of imaging plane and x-ray source, and position of skull phantom within the x-ray field of view. Several close-up views of the surface model of the skull phantom are also presented.

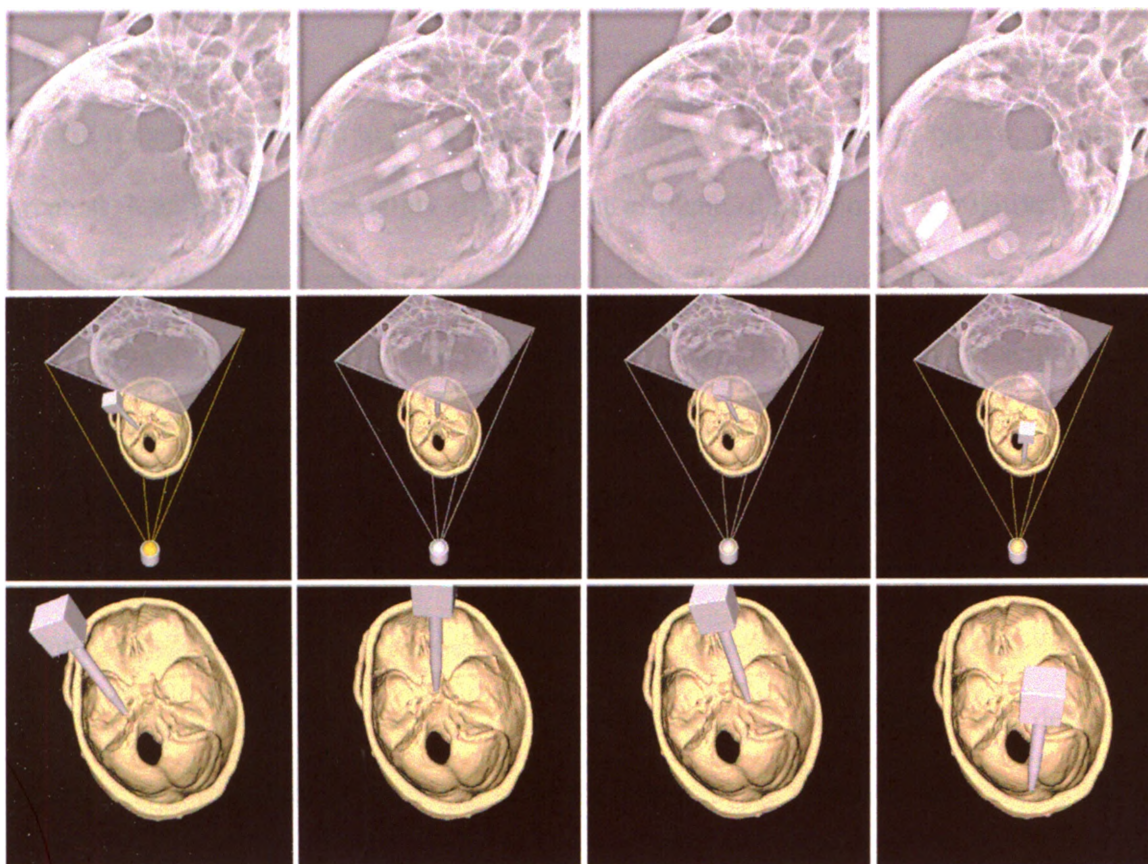


**Figure 2-14:** Two-dimensional projections acquired during dynamic tracking experiment (first row), and corresponding snapshots of the 3D virtual environment (second and third rows) during target localization.

## 2.4 Discussion

The results of the accuracy and precision assessment show several general trends. Firstly, both the accuracy and precision of target localization using single-perspective projections are significantly better in the in-plane directions compared to the out-of-plane direction (**Figure 2-9**). The decrease in accuracy and precision in the out-of-plane direction can be attributed to the perspective geometry of the imaging system, where the greatest localization uncertainty lies in out-of-plane direction. A relatively large translation (i.e. several mm) of the sparse object in the out-of-plane direction only has a small impact on the resulting change in geometry magnification within the acquired 2D perspective projections. However in the in-plane directions, translations can be measured more accurately due to the resolution of the acquired projections. All of the 2D projections acquired during the experiment had sub-millimeter pixel spacing; therefore it is intuitive to be able to localize our sparse object markers with a sub-pixel accuracy and precision in the in-plane directions, which is reflected in the results. This decreased accuracy and precision of localization in the out-of-plane direction has been noted in other studies that have utilized single-perspective projections for measurement and registration purposes.<sup>19,22,25,39,40</sup>

The second trend evident within the results of the accuracy assessment is that the TRE is significantly affected by the acquisition view; most notably with the accuracy assessment performed using the XRII (**Figure 2-10**). In general, the accuracy was significantly better when acquiring images in the AP view. This can be attributed to the anisotropic distribution of the markers of the sparse object, which causes the localization

accuracy to be dependant on the orientation of the sparse object with respect to the imaging plane. Due to the experimental setup, the sparse object was in a more favorable orientation (i.e. long axis of stylus aligned orthogonal to the image plane) during the assessments performed utilizing the AP views, which lead to a significantly better TRE.

This trend of accuracy being dependant on the sparse object orientation was not as prevalent within the results of the precision assessment (**Figure 2-11**). The measurements made using the FP detector did not show any significant difference in precision between the two viewing angles. Although there was a significant difference noted in the precision of measurements made with the XRII between the two viewing angles, the difference was less than several hundred microns, and therefore negligible. The independence of the precision of measurements and the orientation of the tool is expected and can be explained by the main factor limiting the precision. The main source of variation (or imprecision) between the repeated measurements made during the precision assessments was the noise present within the acquired projection images. Since the projections acquired in both the AP and LAO views were acquired with the same imaging parameters, it is expected that the noise levels within those images would be similar, and therefore the precision of the measurements to be consistent, irrespective of the projection view.

Also, the results show that the accuracy and precision of measurements performed using the FP detector were significantly better than those performed using the XRII (**Figure 2-9**). Although the differences in the accuracy and precision of measurements made in-plane (**Figure 2-10a** & **Figure 2-11a**) were negligible, the differences are clearly evident, and significant when comparing the accuracy and precision of measurements

made in the out-of-plane direction (**Figure 2-10b & Figure 2-11b**). The improved performance when utilizing the FP detector for image acquisition can be attributed to a number of advantageous characteristics associated with a FP detector when compared to the XRII (see section §1.4). The main advantage of the FP detector is that it is inherently free of any geometric distortions, and although the images acquired using the XRII were corrected for geometric distortions and non-uniformities, the correction is imperfect, and residual errors within the corrected images remain.<sup>34,36</sup> These residual errors degrade the accuracy and precision of single-plane tracking. Additionally, the FP detector has a higher resolution (i.e. finer pixel spacing) than the XRII. This higher resolution allows the centroids of the 2D marker projections to be measured with a higher precision, leading to an improved accuracy and precision when localizing the sparse object from a single-perspective projection.

Finally, the results verified an expected outcome: the accuracy and precision of measurement made with the OTS, the *gold standard*, were higher than those made using the single-perspective projections (**Figure 2-9**). Although there was no significant, or relevant, difference in the accuracy and precision of the measurements made in-plane (**Figure 2-10a & Figure 2-11a**), the accuracy and precision of measurements made in the out-of-plane directions were significantly higher with the OTS compared to the other methods (**Figure 2-10b & Figure 2-11b**). This reflects that the fact that the OTS localizes its optical fiducials through triangulation from two views, whereas the single-plane tracking only has one. This second view supplements the lack, or insensitivity, of information available in the out-of-plane direction thereby improving the accuracy and precision of measurements made in this direction.

The results of the dynamic tracking assessment reflect the trend previously noted from the assessment of accuracy and precision. The tracking accuracy in the in-plane directions (**Figure 2-12a,b**) is significantly better than that in the out-of-plane direction (**Figure 2-12c**). Since the results of the assessment of accuracy show that there was no significant difference in the accuracy of measurements made inplane between the OTS and single-perspective projection acquired using the FP detector (**Figure 2-10a**), the inplane RMS tracking error (**Figure 2-12a,b**) can be viewed as a combination of errors contributed equally from both tracking systems. The majority of the RMS tracking error in the out-of-plane direction is contributed by the single-plane tracking, as the OTS has significantly higher measurement accuracy in this direction (**Figure 2-10b**). The large frame-to-frame variation in the out-of-plane translation determined from the projection acquired using the FP detector (**Figure 2-12c**) can be partly attributed to the low exposure (0.1 mAs) used during image acquisition. The low exposure resulted in higher noise levels within the acquired projections, which in turn propagate into the solution of the out-of-plane translation. It would be possible to further reduce the tracking error in the out-of-plane direction through implementation of either low pass filtering, or a moving average through the sliding window technique, which would in either case act to smooth the data of the z translation by removing some of the unwanted noise from the solution.

It is important to note that both the results of the accuracy and precision assessment, and the dynamic tracking assessment, are specifically related to the design of the sparse object. Changing the number and geometric configuration of the markers within the sparse object would result in different accuracies and precision in localizing it

from a single-perspective projection.<sup>22,25</sup> This same principle applies to the optical tracking system and to the design of the optical tracking frame.<sup>41</sup>

The algorithm performed with a sufficiently low failure rate to enable seemingly continuous tracking of both the stylus and skull phantom from the projections acquired during the dynamic tracking experiment. The tracking failures that were encountered arose mainly from the occlusion of markers by higher density areas of the boney skull phantom, which prevented the 3D-to-2D registration module from calculating a transformation (requires at least 4 non-coplanar points). Therefore, optimizing the acquisition protocol, to further increase the contrast between the markers of the sparse object and higher density anatomical structures, would further reduce the failure rate. Note, that the radiography system used for the dynamic tracking experiment was installed with preset acquisition protocols (clinical protocols), and did not allow the input of custom acquisition parameters.

The algorithm also demonstrated the ability to process image frames in sub-second time. Its current implementation, on a personal computer, achieved a throughput of approximately 4 image frames per second after the initialization process. With further optimization of the source code, and implementation on dedicated hardware, real-time processing of the acquired image frames is realizable. Several commercial tracking systems exist that process stereo camera images for real-time tracking applications (MicronTracker, Claron Technologies Inc., CA).

To fully automate the algorithm, the problem of establishing correspondence between the rigid-body model of the sparse object, and the 2D marker projections within

the image frame must be addressed. In the current implementation of the algorithm the users sets the correspondence manually. This process could be automated through a combination of careful design of the sparse object (i.e. unique marker sizes and geometry), and automated algorithms that establish correspondence using unique geometric constraints.<sup>42-44</sup> However, this problem is outside the scope of the study and will be left to future work.

The snapshots of the visualizations and 3D virtual environment are an example of how intraoperative imaging can be augmented with preoperative data, such as CT volumes, and tracking data to provide 3D context and navigation in an interactive environment (**Figure 2-13 & Figure 2-14**). The process of registering the preoperative, intraoperative, and tracking data into a common coordinate system is a crucial step in providing an accurate representation of the interventional environment.<sup>37</sup> In our case, this registration was determined directly from the acquired intraoperative images (i.e. acquired 2D projections) by means of the 3D-to-2D registration algorithm presented above (see section §2.2.2). This step inherently registers both the preoperative data and tracking data into the intraoperative imaging coordinate system in one step. The use of virtual environments to augment intraoperative imaging has been explored for numerous applications including intracardiac interventions,<sup>45</sup> abdominal procedures,<sup>46</sup> neurosurgery,<sup>47</sup> and various orthopaedic procedures.<sup>48</sup>

## 2.5 Conclusions

This study has demonstrated the feasibility of tracking sparse objects in 3D space from single-perspective, 2D projections for purposes of image-guidance during interventional procedures. Better performance was achieved using the FP detector for image acquisition when compared to the XRIL. The accuracy and precision of target localization was better than 1.1 mm and 0.16 mm, respectively when using the FP detector for image acquisition, while the dynamic RMS tracking error was 2.1 mm when using an OTS as a standard reference. Most of the inaccuracies and imprecision in target localization and tracking were contributed by errors in out-of-plane localization. The OTS achieved higher levels accuracy and precision, as expected. However, the accuracy achieved using single-perspective projections are relevant for numerous applications, and could potentially be used to augment - or to replace - an OTS during procedures in which line-of-sight issues arise.

## 2.6 References

1. Peters TM. 2006. Image-guidance for surgical procedures. *Phys Med Biol* 51: R505-540.
2. Holly LT, Foley KT. 2003. Intraoperative spinal navigation. *Spine* 28: S54-61.
3. Kahler DM. 2004. Image guidance: fluoroscopic navigation. *Clin Orthop Relat Res*: 70-76.
4. Holly LT. 2006. Image-guided spinal surgery. *Int J Med Robot* 2: 7-15.
5. Laine T, Lund T, Ylikoski M, Lohikoski J, Schlenzka D. 2000. Accuracy of pedicle screw insertion with and without computer assistance: a randomised controlled clinical study in 100 consecutive patients. *Eur Spine J* 9: 235-240.
6. Hart RA, Hansen BL, Shea M, Hsu F, Anderson GJ. 2005. Pedicle screw placement in the thoracic spine: a comparison of image-guided and manual techniques in cadavers. *Spine* 30: E326-331.
7. Raabe A, Beck J, Rohde S, Berkefeld J, Seifert V. 2006. Three-dimensional rotational angiography guidance for aneurysm surgery. *J Neurosurg* 105: 406-411.
8. Mascott CR. 2006. In vivo accuracy of image guidance performed using optical tracking and optimized registration. *J Neurosurg* 105: 561-567.
9. Zhang H, Banovac F, Lin R, Glossop N, Wood BJ, Lindisch D, Levy E, Cleary K. 2006. Electromagnetic tracking for abdominal interventions in computer aided surgery. *Comput Aided Surg* 11: 127-136.
10. Hoffmann KR, Williams BB, Esthappan J, Chen SY, Carroll JD, Harauchi H, Doerr V, Kay GN, Eberhardt A, Overland M. 1997. Determination of 3D positions of pacemaker leads from biplane angiographic sequences. *Med Phys* 24: 1854-1862.
11. Jiang H, Liu H, Wang G, Chen W, Fajardo LL. 2000. A localization algorithm and error analysis for stereo x-ray image guidance. *Med Phys* 27: 885-893.
12. Jiang H, Chen WR, Wang G, Liu H. 2001. Localization error analysis for stereo X-ray image guidance with probability method. *Med Eng Phys* 23: 573-581.
13. Hummel J, Figl M, Kollmann C, Bergmann H, Birkfellner W. 2002. Evaluation of a miniature electromagnetic position tracker. *Med Phys* 29: 2205-2212.
14. Schicho K, Figl M, Donat M, Birkfellner W, Seemann R, Wagner A, Bergmann H, Ewers R. 2005. Stability of miniature electromagnetic tracking systems. *Phys Med Biol* 50: 2089-2098.

15. Hummel J, Figl M, Birkfellner W, Bax MR, Shahidi R, Maurer CR, Jr., Bergmann H. 2006. Evaluation of a new electromagnetic tracking system using a standardized assessment protocol. *Phys Med Biol* 51: N205-210.
16. Chen SY, Metz CE. 1997. Improved determination of biplane imaging geometry from two projection images and its application to three-dimensional reconstruction of coronary arterial trees. *Med Phys* 24: 633-654.
17. Hoffmann KR, Sen A, Lan L, Chua KG, Esthappan J, Mazzucco M. 2000. A system for determination of 3D vessel tree centerlines from biplane images. *Int J Card Imaging* 16: 315-330.
18. Baert SA, van de Kraats EB, van Walsum T, Viergever MA, Niessen WJ. 2003. Three-dimensional guide-wire reconstruction from biplane image sequences for integrated display in 3-D vasculature. *IEEE Trans Med Imaging* 22: 1252-1258.
19. Banks SA, Hodge WA. 1996. Accurate measurement of three-dimensional knee replacement kinematics using single-plane fluoroscopy. *IEEE Trans Biomed Eng* 43: 638-649.
20. Meyer SA, Wolf PD. 1999. Registration of three-dimensional cardiac catheter models to single-plane fluoroscopic images. *IEEE Trans Biomed Eng* 46: 1471-1479.
21. Fantozzi S, Benedetti MG, Leardini A, Banks SA, Cappello A, Assirelli D, Catani F. 2003. Fluoroscopic and gait analysis of the functional performance in stair ascent of two total knee replacement designs. *Gait Posture* 17: 225-234.
22. Hoffmann KR, Esthappan J. 1997. Determination of three-dimensional positions of known sparse objects from a single projection. *Med Phys* 24: 555-564.
23. Yuan X, Ryd L. 2000. Accuracy analysis for RSA: a computer simulation study on 3D marker reconstruction. *J Biomech* 33: 493-498.
24. Yuan X, Ryd L, Tanner KE, Lidgren L. 2002. Roentgen single-plane photogrammetric analysis (RSPA.) A new approach to the study of musculoskeletal movement. *J Bone Joint Surg Br* 84: 908-914.
25. Habets DF, Pollmann SI, Yuan X, Peters TM, Holdsworth DW. 2009. Error analysis of marker-based object localization using a single-plane XRII. *Med Phys* 36: 190-200.
26. ISO. Accuracy (trueness and precision) of measurement methods and results. International Standard. ISO 5725-1:1994(E).
27. Schonemann PH. 1966. A generalized solution of the orthogonal procrustes problem. *Psychometrika* 31.

28. Tang X, Sharp GC, Jiang SB. 2007. Fluoroscopic tracking of multiple implanted fiducial markers using multiple object tracking. *Phys Med Biol* 52: 4081-4098.
29. Sharp GC, Jiang SB, Shimizu S, Shirato H. 2004. Prediction of respiratory tumour motion for real-time image-guided radiotherapy. *Phys Med Biol* 49: 425-440.
30. Di Stefano L, Bulgarelli A. 1999. A simple and efficient connected components labeling algorithm. In, 10th International Conference on Image Analysis and Processing (ICIAP'99).
31. Wang MY, Maurer CR, Jr., Fitzpatrick JM, Maciunas RJ. 1996. An automatic technique for finding and localizing externally attached markers in CT and MR volume images of the head. *Biomedical Engineering, IEEE Transactions on* 43: 627-637.
32. Frantz DD, Wiles AD, Leis SE, Kirsch SR. 2003. Accuracy assessment protocols for electromagnetic tracking systems. *Phys Med Biol* 48: 2241-2251.
33. West JB, Maurer CR, Jr. 2004. Designing optically track instruments for image-guided surgery. *Medical Imaging, IEEE Transactions on* 23: 533-545.
34. Fahrig R, Moreau M, Holdsworth DW. 1997. Three-dimensional computed tomographic reconstruction using a C-arm mounted XRII: correction of image intensifier distortion. *Med Phys* 24: 1097-1106.
35. Fahrig R, Holdsworth DW. 2000. Three-dimensional computed tomographic reconstruction using a C-arm mounted XRII: image-based correction of gantry motion nonidealities. *Med Phys* 27: 30-38.
36. Holdsworth DW, Pollmann SI, Nikolov HN, Fahrig R. 2005. Correction of XRII geometric distortion using a liquid-filled grid and image subtraction. *Med Phys* 32: 55-64.
37. Peters T, Cleary K (editors). 2008. *Image-guided interventions - technology and applications* New York, NY: Springer.
38. Schroeder W, Martin K, Lorensen B. 2002. *The visualization toolkit: an object-oriented approach to 3D graphics*. Kitware, Inc.
39. Hoff WA, Komistek RD, Dennis DA, Gabriel SM, Walker SA. 1998. Three-dimensional determination of femoral-tibial contact positions under in vivo conditions using fluoroscopy. *Clin Biomech (Bristol, Avon)* 13: 455-472.
40. Mahfouz MR, Hoff WA, Komistek RD, Dennis DA. 2003. A robust method for registration of three-dimensional knee implant models to two-dimensional fluoroscopy images. *IEEE Trans Med Imaging* 22: 1561-1574.

41. West JB, Maurer CR, Jr. 2004. Designing optically tracked instruments for image-guided surgery. *IEEE Trans Med Imaging* 23: 533-545.
42. Pilu M. 1997. Direct method for stereo correspondence based on singular value decomposition. In. San Juan, PR, USA: IEEE, pp. 261-266.
43. Bai X, Yu H, Hancock ER. 2004. Graph matching using spectral embedding and alignment. In. Cambridge, United kingdom: Institute of Electrical and Electronics Engineers Inc., pp. 398-401.
44. Hornung A, Sar-Dessai S, Kobbelt L. 2005. Self-calibrating optical motion tracking for articulated bodies. In. Bonn, Germany: Institute of Electrical and Electronics Engineers Computer Society, pp. 75-82.
45. Linte CA, Moore J, Wiles AD, Wedlake C, Peters TM. 2008. Virtual reality-enhanced ultrasound guidance: a novel technique for intracardiac interventions. *Comput Aided Surg* 13: 82-94.
46. Das M, Sauer F, Schoepf UJ, Khamene A, Vogt SK, Schaller S, Kikinis R, vanSonnenberg E, Silverman SG. 2006. Augmented reality visualization for CT-guided interventions: system description, feasibility, and initial evaluation in an abdominal phantom. *Radiology* 240: 230-235.
47. Rosahl SK, Gharabaghi A, Hubbe U, Shahidi R, Samii M. 2006. Virtual reality augmentation in skull base surgery. *Skull Base* 16: 59-66.
48. Blackwell M, Morgan F, DiGioia AM, 3rd. 1998. Augmented reality and its future in orthopaedics. *Clin Orthop Relat Res*: 111-122.

### 3 Dynamic Measurement of Joint Kinematics using Single-perspective Projections

#### 3.1 Introduction

The ability to measure the kinematics of a joint during a dynamic activity *in vivo*, with a high degree of accuracy, has numerous orthopaedic applications. These include assessing joint function following corrective surgery,<sup>1</sup> comparing different treatment options and therapies,<sup>2</sup> and understanding the pathology of musculoskeletal disorders and injuries.<sup>3</sup> For example, abnormal motion of the knee joint has been widely accepted as the cause of chondromalacia,<sup>4</sup> and has been attributed to the cause and progression of osteoarthritis.<sup>5,6</sup> A tool with the ability to measure the kinematics of a joint during a dynamic test of its function would be invaluable in a clinical setting, for diagnosis and for evaluating treatment options. Conventional techniques that have been employed to measure *in vivo* joint kinematics involve the use of optoelectronic cameras to track the motion of markers attached to the skin.<sup>7</sup> However, the motion of these skin markers is not an accurate representation of the motion of the underlying bone structures.<sup>8</sup>

Direct measurement of the underlying bone structures is preferred when accuracy is a necessity. Numerous methods have been proposed, and used experimentally, to

directly measure the motion of bone structures of a joint. These include the use of optical tracking frames attached to the ends of intra-cortical pins implanted directly into the bone structure,<sup>9</sup> magnetic resonance imaging (MRI),<sup>10-12</sup> and biplane radiography.<sup>4,13,14</sup> Although each of these techniques can measure joint kinematics with a high degree of accuracy, each is accompanied by its own set of limitations. Implanting intra-cortical pins into the bone structures of a joint is an invasive procedure that carries risk of infection for a patient.<sup>15</sup> MRI is limited by the confines of the close-bore design, which restricts the range of motion, and require specialized apparatus to apply load to a joint.<sup>16</sup> Biplane radiography systems are relatively limited in their availability, and are subject to the technical challenge of ensuring that the joint of interest remains within the working volume defined by the intersection of the two x-ray beams throughout a specified motion.<sup>14</sup> For these reasons, the majority of these techniques currently remain as specialized research tools and have yet to be implemented inside the routine clinical environment.

Since single-plane radiography systems are widely available, they are not subject to these limitations, are routinely used in many clinics, and have an increased working volume compared to both MRI and biplane radiography systems. Several techniques have been proposed to measure kinematics of the joint during a dynamic motion using single-perspective projection images.<sup>17-20</sup> Marker-based techniques, originating from roentgen stereophotogrametric analysis<sup>21</sup> (RSA), employ 3D-to-2D registration between known models of radio-opaque markers, implanted into skeletal segments, and their corresponding projections in radiographic images to derive kinematics. This single-plane technique has been referred to by numerous names including: roentgen single-plane

photogrammetric analysis<sup>19</sup> (RSPA), marker configuration model-based roentgen fluoroscopic analysis<sup>20</sup> (MCM-based RFA), and hybrid RSA and fluoroscopy.<sup>22</sup> Previous validations of this single-plane technique have made use of computer simulations,<sup>19,20</sup> simultaneous measurements made on a static cadaver knee using both fluoroscopy and RSA,<sup>23</sup> dynamic zero-displacement phantom measurements,<sup>20</sup> and static micrometer-based anatomical phantoms of the hip and knee.<sup>22</sup> However, it remains unclear whether measurements made on a static phantom provide an acceptable representation of the dynamic case. Additionally, all previous phantom studies have employed intensifier-based radiography system.<sup>20,22,23</sup> With the recent wide-spread implementation of digital flat-panel (FP) x-ray detector technology,<sup>24</sup> several improvements over image intensifiers are realized, including: improved image quality, no inherent geometric distortion, and reduced dose. These improvements potentially increase the accuracy of single-plane kinematic measurements, making it more viable to implement in the clinic.

The purpose of this study is to validate the technique of dynamically measuring joint kinematics using single-perspective projections. The technique is validated through *in vitro* experiments to assess its accuracy and feasibility. All assessments were performed on a clinically available digital flat-panel radiography system to demonstrate the suitability of using FP detector technology to measure joint kinematics. An anatomically relevant phantom was used in both static and dynamic conditions to perform these assessments. Dosimetry was performed to estimate the effective dose of ionizing radiation imparted to the subject during the measurement procedure, to ensure it is within clinically acceptable levels. Additionally, a method to register computed tomography

(CT) volumes to the measured kinematics is presented towards the applications of estimating joint contact area, biomechanics modeling, and visualization.

## 3.2 Methods

### 3.2.1 Measurement of Kinematics from Single-perspective Projections

The algorithm implemented to measure joint kinematics from single-perspective projection is based upon the solution of the projection-Procrustes registration problem.<sup>25,26</sup> The solution of the projection-Procrustes registration problem determines the optimal 3D-to-2D registration between known sparse objects and their corresponding projections in 2D radiographs. In the case of joint kinematic measurement, the sparse object is a joint implanted with radio-opaque markers. Both the relative location of the markers, implanted into the joint, and the geometry of the perspective radiography system, must be known *a priori* to solve the registration problem. Common methods used to establish a local coordinate system describing the relative 3D locations of radio-opaque markers within a rigid body include RSA,<sup>20,22</sup> and computed tomography.<sup>27</sup> The projective geometry of a single-plane imaging system can be determined using the same procedure that is employed in RSA, which uses a calibration cage (see sections §1.4.3 and §1.4.4).<sup>21</sup> A more thorough review of the projection-Procrustes registration problem, and implementation of the algorithm that determines the 3D-to-2D registration enabling tracking of sparse objects from single-perspective projections are presented in the Chapter 2 (sections §2.2.1 & §2.2.2). All software was developed in C++ and ran on a personal computer equipped with a 2.0 GHz processor and 1 GB of memory.

### 3.2.2 Anatomical Model

An anatomical tibio-femoral model (Sawbones Model #4000-3, Pacific Research Laboratories Inc., WA, USA) was employed in all *in vitro* experiments. The model consists of two rigid plastic segments that mimic the boney structures of the knee joint. Each segment was implanted with 8 spherical, tantalum markers, each 1 mm in diameter (**Figure 3-1a**). The markers were inserted into the distal femur and proximal tibia of the knee model, in a distribution that would be encountered in human subjects recruited for a RSA clinical study. The markers were inserted such that their distribution was well conditioned.<sup>28</sup> A local coordinate system, defining the relative locations of implanted markers, was generated through a conventional RSA examination (**Figure 3-1b,c**) of the knee model using commercial RSA software (UmRSA, RSA Biomedical, Umea, Sweden). This local coordinate system was needed to produce the rigid-body file required as input to the registration algorithm.

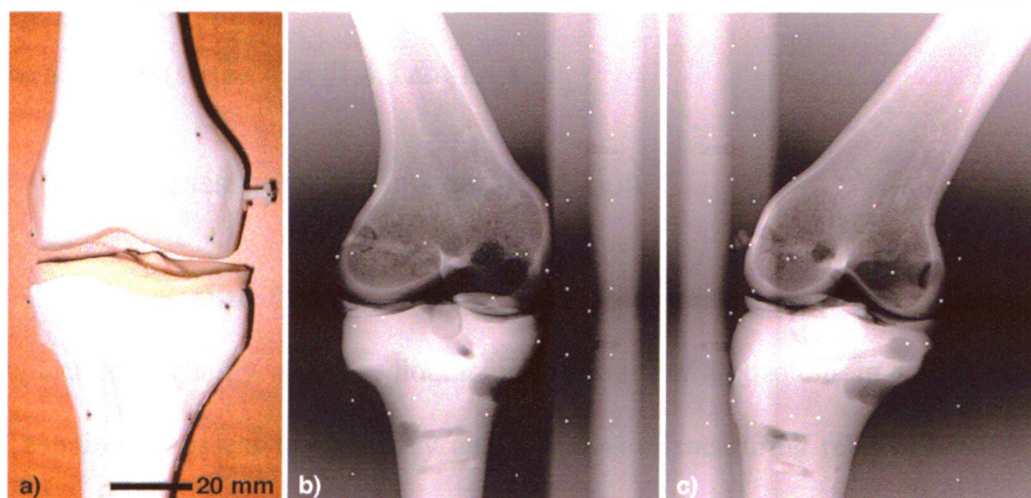


**Figure 3-1:** a) The tibio-femoral knee model used for *in vitro* experiments. Eight tantalum markers, each 1 mm in diameter, were implanted into both the distal femur and proximal tibia of the knee model. b,c) Stereo projections acquired during radiostereometric analysis (RSA) examination used to determine relative locations of the markers.

### 3.2.3 Imaging Equipment

A floor-mounted C-arm radiography system equipped with a digital flat-panel detector (Innova 4100, General Electric, WI, USA) was used throughout the study to acquire images. The viewing mode of the detector, utilized throughout the study, acquires projections of 1K x 1K pixels in dimension, over a 20 x 20 cm<sup>2</sup> field-of-view (FOV). The pixel depth of the image is dependent on the frame rate of the acquisition. Frame rates of 7.5 frames per second (fps) or less; result in projections with a 12-bit pixel depth. Frame rates of 15 fps or more; have an 8-bit pixel depth. Because digital flat panel detectors contain no inherent geometric distortion, unlike conventional XRIIs, it was not necessary to implement any additional distortion-correction algorithm. In previous single-plane studies, which employed intensifier-based radiography systems, correction of geometric distortion was very important to ensure accurate results.<sup>20,22</sup> Before each experiment, the perspective geometry of the radiographic system was determined using a commercial RSA calibration cage (Lund Knee Box, RSA Biomedical, Umea, Sweden) (see section §1.4.3 & §1.4.4).

### 3.2.4 Static Assessment of Bias and Precision

To characterize the performance of the measurement technique under optimal conditions, high-quality, single radiographic exposures of a phantom, in a static position, were acquired to assess the accuracy and precision of measuring relative motion. The static phantom was constructed using a 3-axis, micrometer-driven positioning stage (Model M4434, Parker Hannifin Corp., PA, USA) mounted upon a polymethyl methacrylate base-plate. The positioning stage has a manufacturer's reported accuracy of

2  $\mu\text{m}$ . The femur of the knee model was rigidly attached to the positioning stage, and the tibia fixed to the base-plate. The static phantom was positioned inside the FOV of the radiography system (**Figure 3-2a**), and the femur segment of the knee model was driven to 20 different locations in 50  $\mu\text{m}$  increments, in the range of 0 - 300  $\mu\text{m}$  along each axis of the positioning stage.<sup>22</sup> A projection of the static phantom was acquired (50 kVp, 76 mA, 43 ms) at each location (**Figure 3-2b**), from which the 3D pose of each joint segment was determined by processing the acquired projections with the custom developed software (see section §3.2.1). Relative motion between the femur and tibia was calculated between unique pairs of positions,<sup>28</sup> which produced 10 independent measurements of motion in six degrees-of-freedom (DOF) (i.e. three translations, and three rotations). This displacement protocol was repeated six times, resulting in a total of 60 independent measures of relative motion.

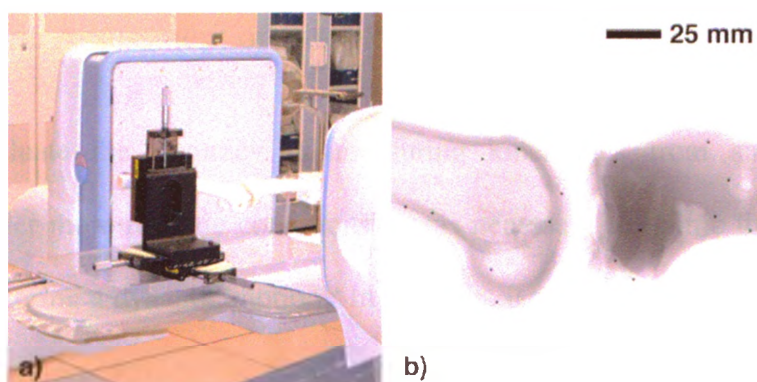


**Figure 3-2:** Experimental setup during static assessment. a) Micrometer-driven positioning stage, with knee model rigidly attached, setup inside field-of-view of radiography system. b) Sample medial-lateral projection of static phantom acquired during the static assessment.

Bias and precision were assessed using the differences between the measured and applied motion. Because the positioning stage was not capable of applying rotations, the known relative orientation between any pair of positions was assumed to be zero. The

mean value of the differences, between measured and known motion, was used to estimate the bias, and the standard deviation the precision. To provide a robust measure of accuracy, the 95% prediction interval of the differences (i.e. measurement errors) was estimated using a two-tailed t-distribution.<sup>22,29</sup> This prediction interval was calculated using the 95% percentile constant for a t-distribution with 59 DOF, which is 2.001. Statistical analysis was performed using a statistics software package (Prism 4, GraphPad Software Inc., CA, USA) to determine whether the measurement bias (mean error) was significantly different from zero, and whether the distributions of error were normal. A one-way analysis of variance (ANOVA), followed by a Tukey post-hoc test was performed to identify if the bias was significantly different from zero. A Kolmogorov-Smirnov normality test was performed to determine if the distributions of measurement errors were normal.

### 3.2.5 Dynamic Assessment of Bias, Precision and Repeatability

To evaluate the accuracy of measuring kinematics from single-perspective projections under more realistic conditions it was necessary to mimic the kinematics of the knee joint during a dynamic motion. In addition, it was important that the prescribed motion be highly repeatable. To fulfill these requirements a six-axis articulated robot (Model A465 Arm + C500C Controller, Thermo CRS Ltd., ON, CA), commonly used in process automation, with a manufacturer's stated precision of  $\pm 0.05$  mm, was used as a component of a dynamic phantom. The anatomical knee model, which was used within the static phantom, was again used within the dynamic phantom. The femur of the knee model was rigidly attached to the end-effector of the robotic arm, and the tibia was fixed to the base of the robotic arm. The robot was programmed to apply a repeated cycle of

flexion/extension motions to the knee joint to mimic the tibio-femoral kinematics of a knee during an ascent/descent activity. The robot was positioned to ensure that the joint was within the 20 cm FOV of the digital flat-panel radiography unit, throughout its prescribed flexion/extension motion (**Figure 3-3**). Six dynamic acquisitions of the dynamic knee phantom were acquired (30 frames per second, 60 kVp, 30 mA, 3 ms). During each acquisition, the knee joint was moved through approximately three flexion/extension cycles, with an average speed of approximately  $60^\circ$  per second (**Figure 3-4**).

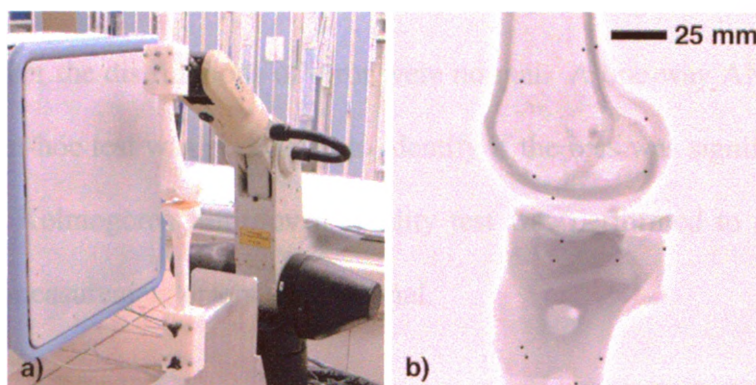


**Figure 3-3:** Experimental setup during dynamic assessment. a) Six-axis articulated robot, with knee model rigidly attached, setup inside field-of-view of the radiography system. b) A sample medial-lateral projection of the dynamic phantom acquired during the dynamic assessment.

To assess the accuracy of dynamic measurements, two rigid-body models were defined within the femur segment of the knee phantom. Four of the eight markers imbedded into the femur segment were assigned to one rigid-body, and the remaining four to the other. The 3D pose of each defined rigid-body was determined from every frame within each acquisition with the custom developed software described in section §3.2.1. Relative motion was derived between consecutive frames in each acquisition. Since there was no actual relative motion between each rigid-body (both were rigidly

attached to the femur segment of the knee phantom), any relative change in position or orientation can be attributed to measurement error.<sup>20</sup> A total of over 1200 measurements of relative motion were obtained from all six acquisitions. Bias was estimated using the mean of the measurement errors, precision using the standard deviation. A robust measure of accuracy was determined by calculating the 95% prediction interval of the measurement errors using a two-tailed t-distribution.<sup>29</sup> This interval was calculated using the 95% percentile constant for a t-distribution with over 1000 DOF, which is 1.96. Statistical analysis was performed using a statistics software package (Prism 4) to determine whether the measurement bias (mean error) was significantly different from zero, and whether the distributions of error were normal. A one-way ANOVA, followed by a Tukey post-hoc test was performed to identify if the bias was significantly different from zero. A Kolmogorov-Smirnov normality test was performed to determine if the distribution of measurement errors were normal.

Comparison of the motion derived from each acquisition assessed the repeatability of measuring the kinematics of the femur, relative to the tibia. The 3D pose of both the tibia and femur segments was determined from every frame within each acquired sequence using the custom developed software (see section §3.2.1). All eight markers implanted into each segment were utilized during pose calculation. Relative motion was derived using the resting or neutral pose of the joint ( $\sim 0^\circ$  flexion) as a reference. The standard deviation was calculated at every time point for each kinematic DOF across the six trials. The mean value of the deviations was utilized to quantify repeatability. In order to achieve this, a common point within each of the six datasets was identified to synchronize them to common start and end time.<sup>13</sup> It was necessary to perform this

synchronization because the motion of the six-axis articulated robot was not intrinsically synchronized to the acquisition timing of the imaging system. To synchronize the data, a linear interpolant was fit to each dataset using curve fitting software (Matlab curve fitting toolbox, Mathworks Inc., MA, USA). The resulting piecewise curves were resampled to a higher rate (300 Hz), and the time shift required to synchronize them was found by minimizing the distance between common points identified in each curve. Repeatability was assessed using the resampled and synchronized motion datasets.

While the bone segments tracked in this study each contained eight marker beads, this represents the upper bound of the number of markers expected to be visible in a clinical implementation. To investigate the effect of a smaller number of markers on measurement repeatability for dynamic motion, all acquired images were subsequently re-processed to mimic two additional cases: inclusion of only six of the eight markers, and inclusion of only four markers in each of the segments. Statistical analysis was performed using a statistics software package (Prism 4) to determine if the number of markers utilized for pose calculation significantly affected the repeatability of measurements. A one-way ANOVA followed by a Tukey post-hoc test was performed along each DOF (i.e. 3 translations, 3 rotations), to identify statistically significant differences.

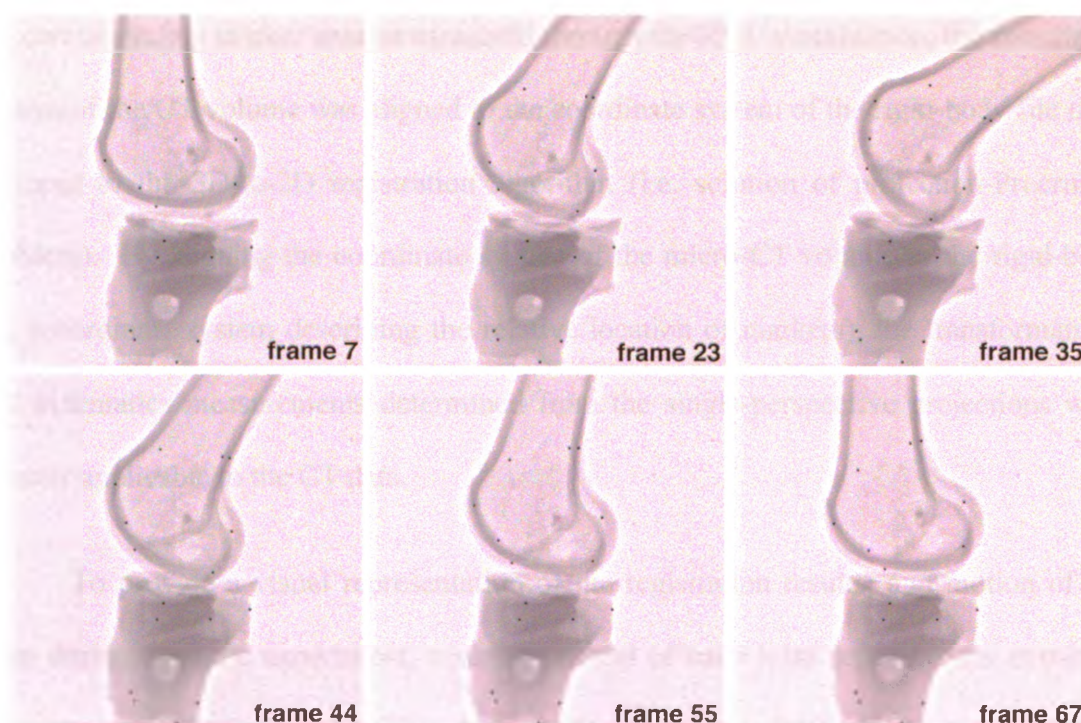


**Figure 3-4:** Sample frames acquired during the dynamic assessment and representative of the range of motion of one cycle of the dynamic phantoms programmed movement.

### 3.2.6 Registration of CT Data to Kinematic Measurements

Computed tomography (CT) scans of the knee model were acquired and registered to the kinematic measurements to demonstrate the application of single-perspective kinematic measurements towards several applications, including: estimation of joint space or contact area, biomechanics modeling, and visualization. A micro-CT scan of each segment (i.e. femur and tibia) of the knee model, implanted with the tantalum markers, was acquired using a micro-CT scanner (Locus Ultra, General Electric, WI, USA). The centroid of each tantalum marker was localized within the CT volumes using CT analysis software (MicroView, General Electric, WI, USA). Using a rigid, point-based technique<sup>30</sup> to register the marker centroids identified within the microCT volumes, and

the corresponding marker centres measured through the RSA examination, the coordinate system of the CT volume was aligned to the coordinate system of the rigid-body file used as input to the 3D-to-2D registration algorithm (i.e. solution of projection-Procrustes problem). By aligning the coordinate system of the micro-CT volume to the rigid-body file (coordinate system describing the relative location of markers), the transformations and kinematics measurements determined from the single-perspective projections were directly applicable to the CT data.

To provide a visual representation of the registration results, and motion of the knee during dynamic experiment, a surface model of each joint segment was extracted from the co-registered micro-CT volumes. Using the six DOF rigid transformations determined from the dynamic image sequences, the motion of joint was reconstructed inside a virtual environment. A custom C++ script developed using open-source visualization classes<sup>31</sup> (Visualization ToolKit, Kitware Inc., NY, USA). The transformations were sequentially applied to each surface model to reconstruct the motion of the knee during the dynamic acquisitions.

### 3.2.7 Measurement of Effective Dose

Dose measurements were performed to estimate the effective dose a patient would receive during a typical dynamic single-plane acquisition. An ion chamber (Model 96020A, Keithley Instruments Inc., OH, USA), in combination with a digital dosimeter (Model 35614, Keithley Instruments Inc., OH, USA) was used to obtain measurements of entrance exposure, from which the effective dose was determined. The ion chamber was positioned inside the FOV of the digital flat-panel radiography unit, facing the source

(Figure 3-5). Entrance exposure was measured during approximately six seconds of irradiation (30 fps, 60 kVp, 30 mA, 3 ms). Measurement of entrance exposure was repeated six times to ensure the stability and reproducibility of the measurement instruments. Absorbed dose was determined from the measured entrance exposure by using an accepted exposure-to-dose conversion coefficient<sup>32</sup> for bone of  $0.4 \text{ GyR}^{-1}$ . Effective dose was calculated using a tissue sensitivity constant applicable to the knee of  $0.9 \mu\text{SvGy}^{-1}\text{cm}^{-2}$  derived from previous dosimetry studies,<sup>32</sup> and estimating the irradiated tissue area to be  $400 \text{ cm}^2$ .

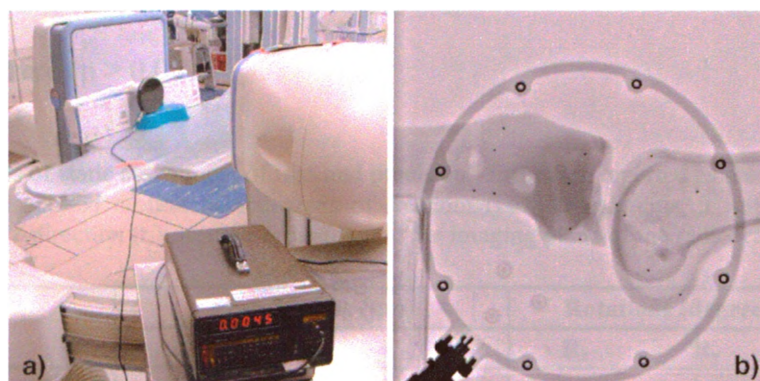


**Figure 3-5:** Experimental setup during measurement of effective dose. a) Ion chamber within field-of-view (FOV) of radiography system, and digital dosimeter used to measure entrance exposure. b) Sample projection acquired during dose measurements showing knee model and ion chamber.

### 3.3 Results

#### 3.3.1 Static Assessment of Accuracy and Precision

A summary of the results of the static assessment of accuracy and precision is presented in **Table 3-1**. Measurement errors were defined as the difference between the measured and applied motion. The accuracy of measuring translations was found to be better than 0.03 mm in-plane (i.e. parallel to the imaging plane), and 0.5 mm out-of-plane (i.e. orthogonal to the imaging plane). Rotations were measure with an accuracy of better than  $0.1^\circ$  about all axes. The results of the statistical analysis performed (ANOVA with Tukey post-hoc) did not find any statistically significant difference between the bias in each DOF and zero ( $p > 0.05$ ).

**Table 3-1:** Results of static assessment of bias and precision. Errors are reported as the difference between the measured and applied motion in 6 degrees of freedom (i.e 3 translations, 3 rotations). Note, that translations in the z-direction ( $t_z$ ) occurred orthogonal to the imaging plane of the radiography system.

	Translations ( $\mu\text{m}$ )			Rotations (degrees $\times 10^{-3}$ )		
	$t_x$	$t_y$	$t_z$	$R_x$	$R_y$	$R_z$
<b>Bias (Mean)</b>	2.4	-4.6	-13.2	0.7	4.1	0.9
<b>Precision (SD)</b>	10.6	9.1	224.5	15.9	12.3	13.8
<b>95% PI (2.001SD)</b>	21.3	18.2	449.1	32.0	24.6	27.6

The distributions of error, in each DOF, from the static assessment are presented in **Figure 3-6**. The box and whisker plots display the median (centre line), 25<sup>th</sup> and 75<sup>th</sup> percentiles (outer edges of box), and the maximum and minimum measurement errors (whiskers). The results of the Kolmogorov-Smirnov normality test showed that the distribution of error about each DOF was normal (i.e.  $p > 0.1$  – distributions are likely to be normal given the sample size).

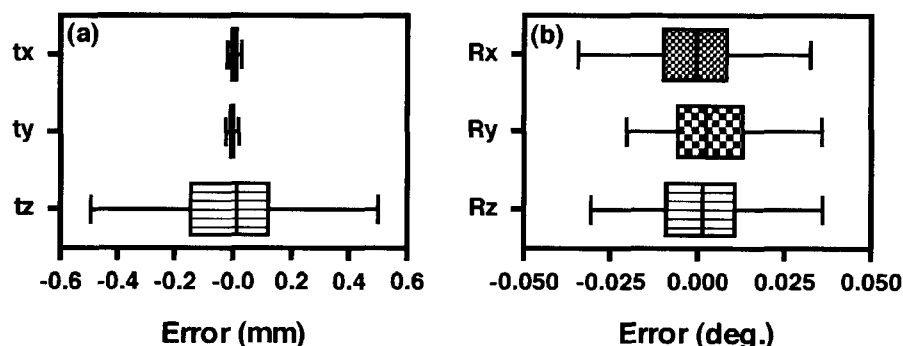


**Figure 3-6:** Box and whisker plots representing the distribution of errors (i.e. difference between measured and applied motion) in 6 degrees-of-freedom, obtained from static assessment of accuracy and precision. Note, that translations in the z-direction ( $t_z$ ) occurred orthogonal to the imaging plane.

### 3.3.2 Dynamic Assessment of Accuracy and Precision

A summary of the results of the dynamic assessment of accuracy and precision are presented in **Table 3-2**. Measurement errors were defined as the deviation of the measured motion from zero (rigid-bodies were attached to same segment of the knee model). The accuracy of measuring translations was shown to be better than 0.03 mm in-plane, and 0.9 mm out-of-plane. Rotations were measured with an accuracy of better than  $0.1^\circ$  about all axes. The results of the statistical analysis performed (ANOVA with Tukey post-hoc) did not find any statistically significant difference between the bias in each DOF and zero ( $p > 0.05$ ).

**Table 3-2:** Results of dynamic assessment of bias and precision. Errors are reported as the deviation of measured motion from zero in 6 degrees-of-freedom (i.e 3 translations, 3 rotations). Note, that translations in the z-direction ( $t_z$ ) occurred orthogonal to the imaging plane of the radiography system.

	Translations ( $\mu\text{m}$ )			Rotations (degrees $\times 10^{-3}$ )		
	$t_x$	$t_y$	$t_z$	$R_x$	$R_y$	$R_z$
<b>Bias (Mean)</b>	0.0	-0.2	0.2	0.1	0.0	0.0
<b>Precision (SD)</b>	14.5	12.9	433.3	25.9	27.0	23.8
<b>95% PI (1.96SD)</b>	28.4	25.2	849.4	50.7	52.9	46.6

The distributions of error, in each DOF, from the dynamic assessment are presented in **Figure 3-7**. The box and whisker plots display the median (centre line), 25<sup>th</sup> and 75<sup>th</sup> percentiles (outer edges of box), and the maximum and minimum errors (whiskers). The results of the Kolmogorov-Smirnov normality test showed that the distribution of error about each DOF was normal (i.e.  $p > 0.1$  – distributions are likely to be normal given the sample size).

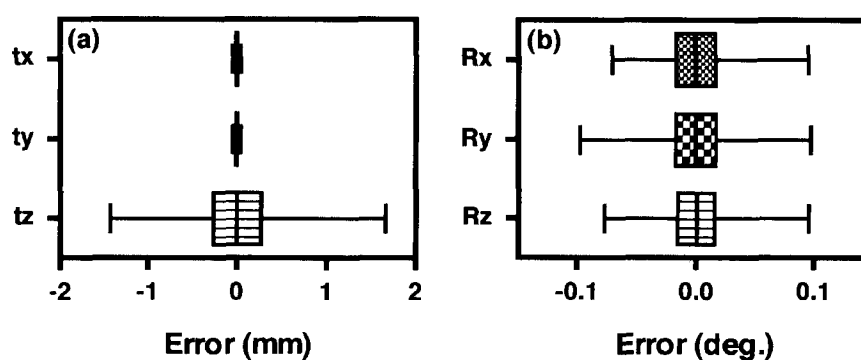


**Figure 3-7:** Box and whisker plots representing the distribution of errors (i.e. deviation of measured motion from zero) in 6 degrees-of-freedom, obtained from dynamic assessment of accuracy and precision. Note, that translations in the z-direction ( $t_z$ ) occurred orthogonal to the imaging plane.

### 3.3.3 Repeatability of Kinematic Measurements

The kinematics of a single cycle of motion of the knee model, as measured from all six trials of the dynamic assessment is presented in **Figure 3-8**. Note that although the motion is expressed in anatomically relevant terms, that these are simply ‘approximate’, and were not developed using anatomically-based methods.<sup>33,34</sup> The process of assigning an anatomically-based coordinate system to a joint has errors inherent to the selection of bony landmarks,<sup>35,36</sup> which would further contribute to the variation between the motion measured from each of the six trials. The repeatability of measuring the knee kinematics

produced by motion of the six-axis articulated robot was better than  $\pm 0.2$  mm for translations, and  $\pm 0.1^\circ$  for rotations, when using all 8 markers within both segments (**Figure 3-9**). The repeatability of measuring in-plane translations was higher than that in the out-of-plane direction. Measuring rotations were highly repeatability about all axes. The greatest variability in the measurement of rotation was seen about the axis with the largest range of motion (flexion/extension; range  $\sim 55^\circ$ ).

With respect to the repeatability in the case a of reduced number of visible markers, the results (**Figure 3-9a**) shows that the repeatability of measuring translations in the out-of-plane direction was significantly affected ( $p < 0.05$ ) by reducing the number of markers from 8 to 4, and from 6 to 4. In-plane translations showed no significant reduction in the repeatability as the number of markers were reduced ( $p > 0.05$ ). A significant difference ( $p < 0.05$ ) was observed in the repeatability of measuring rotations around the x and y axes when reducing the number of markers from 8 to 4 (**Figure 3-9b**), however these differences were very small, less than  $0.025^\circ$  in magnitude.

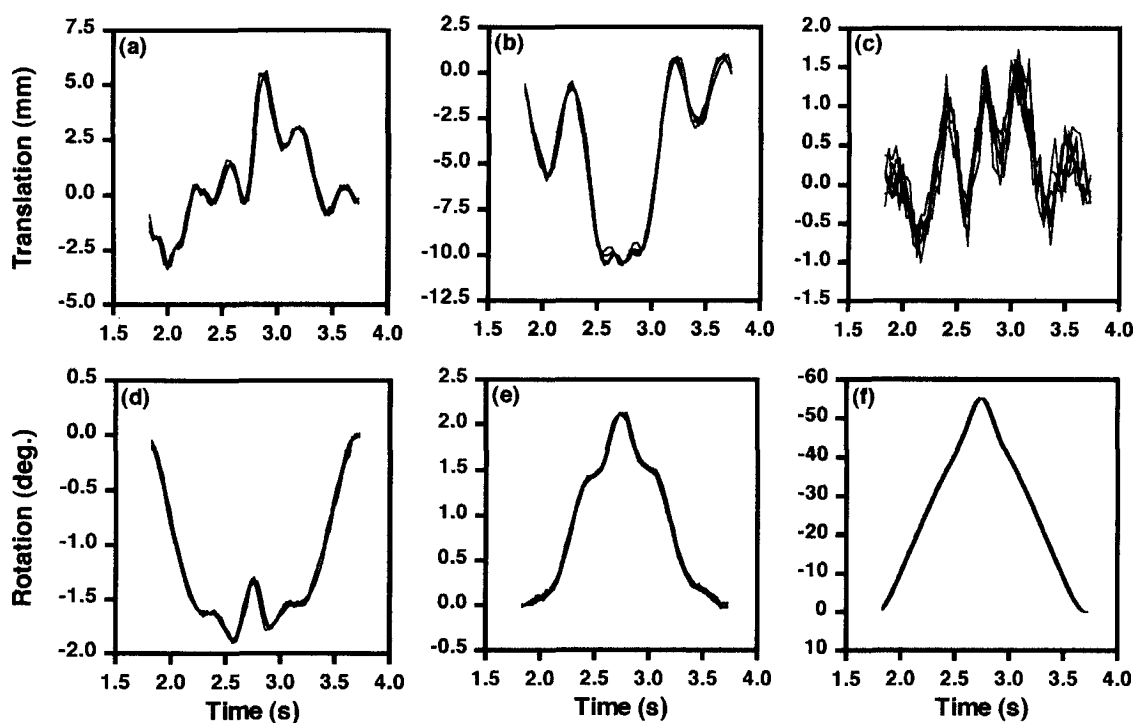


**Figure 3-8:** Kinematics of the knee model during dynamic assessment performed to assess repeatability of measurements. The kinematics measured from all six trials are plotted within the same axes, and are expressed in 6 degrees-of-freedom (i.e 3 translations and 3 rotations). Both translations and rotations are of the femur relative to the tibia. Translation are expressed as (a) Proximal/Distal ( $t_x$ ), (b) Anterior/Posterior ( $t_y$ ), and (c) Medial/Lateral ( $t_z$ ). Rotations are expressed as (d) Abduction/Adduction ( $R_x$ ), (e) Interior/Exterior ( $R_y$ ), and (f) Flexion/Extension ( $R_z$ ). Note, that translation in the Medial/Lateral direction, (c), occurred orthogonal to the imaging plane of the radiography system (out-of-plane).

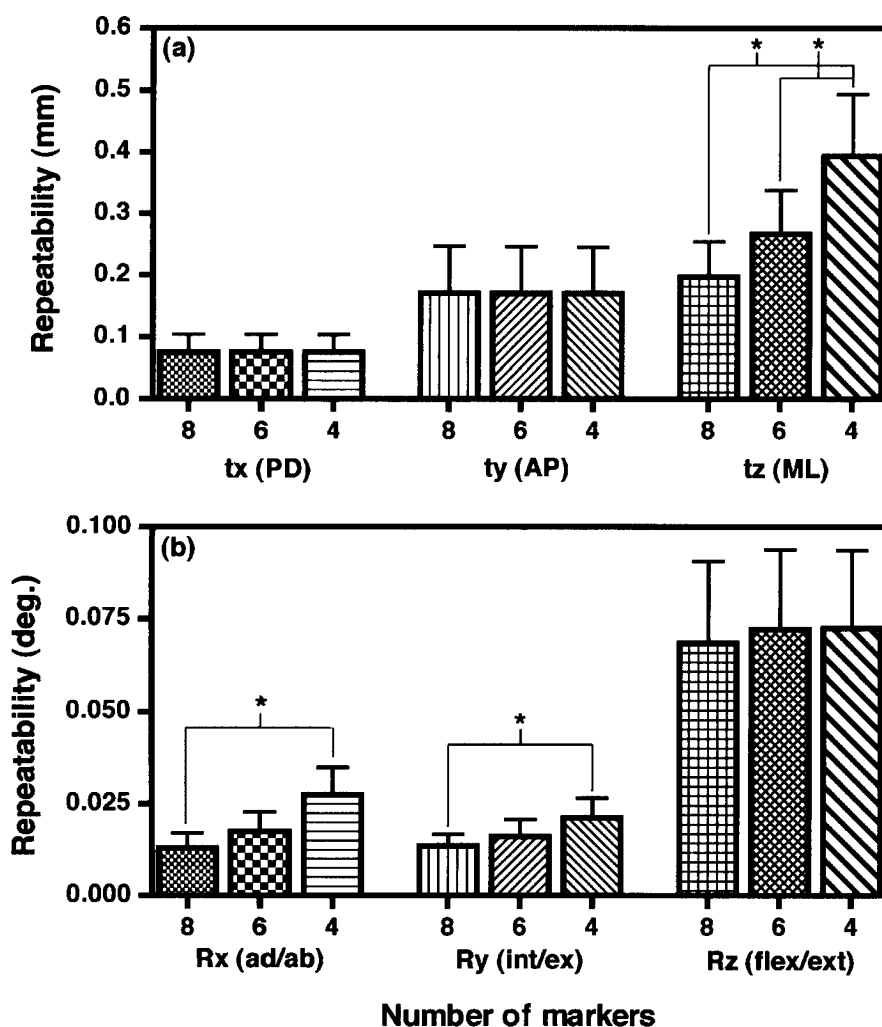


**Figure 3-9:** Repeatability of kinematic measurements vs. the number of markers used within the rigid-body to perform 3D-to-2D registration. Repeatability is expressed along each degree of freedom (i.e. 3 translations and 3 rotations). Translations, (a), are expressed as Proximal/Distal (PD or  $t_x$ ), Anterior/Posterior (AP or  $t_y$ ), and Medial/Lateral (ML or  $t_z$ ). Rotations, (b), are expressed as Abduction/Adduction (ad/ab or  $R_x$ ), Interior/Exterior (int/ex or  $R_y$ ), and Flexion/Extension (flex/ext or  $R_z$ ). Note, that \* represents a statistically significant difference ( $p < 0.05$ ).

### 3.3.4 Registration of CT Data to Kinematic Measurements

The root-mean-square (RMS) fiducial registration error<sup>37</sup> (FRE) between the corresponding markers identified both in the CT volume, and by RSA was 0.1 mm. A snapshot of the constructed virtual environment showing the registration between the 3D surface models of the knee, extracted from the acquired CT volumes, and the 2D projections, acquired during the dynamic assessment, is presented in **Figure 3-10**. The geometry of the perspective x-ray imaging system was reconstructed to include the 3D position of the 2D imaging plane, and x-ray source. The 3D position of each segment of the knee model was determined by registering the CT data to the kinematic measurements determined from the single-perspective projections.

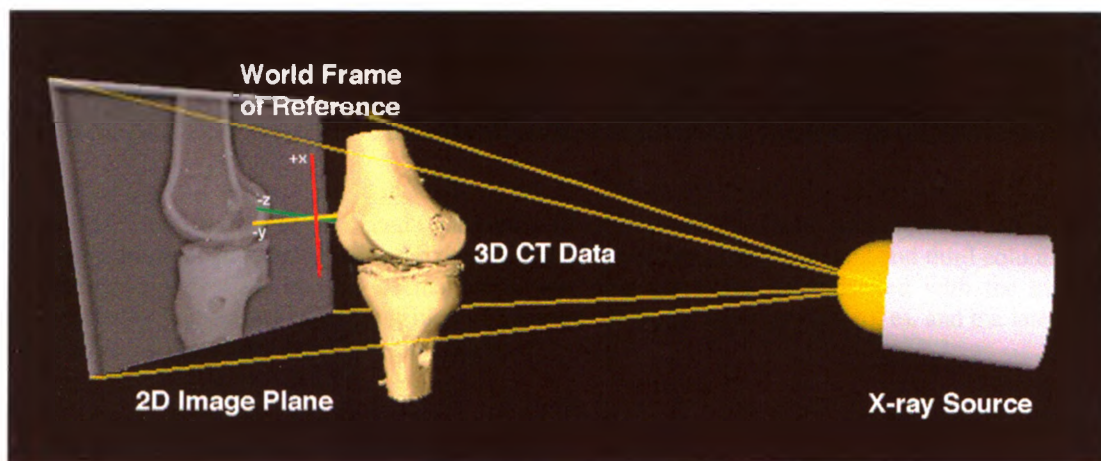


**Figure 3-10:** Registration of three-dimensional (3D) computed tomography (CT) data to two-dimensional (2D) projections. Visualization shows reconstructed position of x-ray source, imaging plane, knee joint (implanted with tantalum markers), and world frame of reference.

Further visuals of the registration between the CT data (i.e. surface models) and kinematic measurements are presented in **Figure 3-11**. Projections acquired during the dynamic assessment at 0°, and 55° flexion are presented in the first column of the figure.

The corresponding anterior, and lateral views of the 3D joint surfaces are presented in the second and third columns respectively.

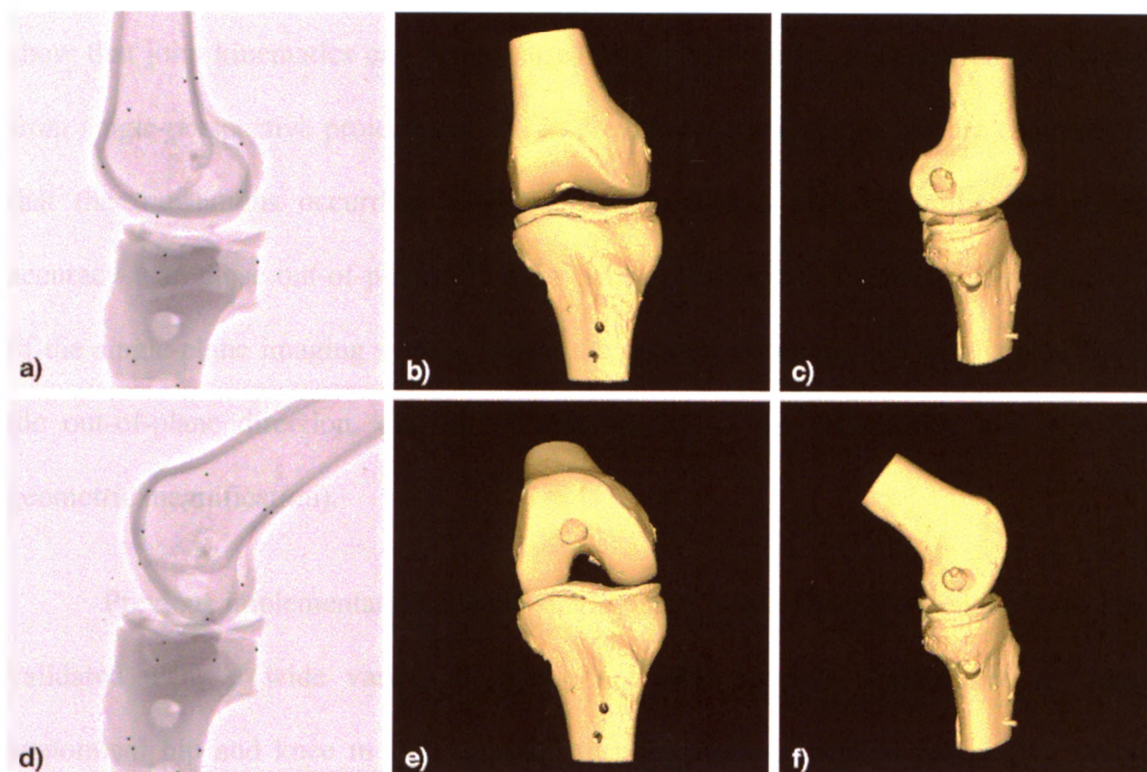


**Figure 3-11:** Registration of computed tomography (CT) data with kinematic measurements. First column shows projections acquired at 0° joint flexion a), and 55° joint flexion d). Second and third columns show the corresponding surface models of the femur and tibia segments, as registered with the kinematic measurement to reconstruct relative position of the joint. Both the anterior view b), e), and the lateral view c), f) of the joint are shown at both flexion angles.

### 3.3.5 Measurement of Effective Dose

The effective dose associated with a 180-frame dynamic acquisition of the knee was found to be less than 3  $\mu\text{Sv}$ , which corresponds to an effective dose of about 0.01  $\mu\text{Sv}$  per frame. This estimate is only applicable for lower extremities, as the conversion from absorbed dose to effective dose is dependant on the tissue sensitivity of a specific anatomical site.

### 3.4 Discussion

The results obtained from the validation experiments (**Table 3-1** & **Table 3-2**) show that joint kinematics can be measured in six DOF with a high degree of accuracy from single-perspective projections. As in previous studies, our results are consistent in that the translations occurring in-plane were measured with a significantly greater accuracy than those out-of-plane.<sup>20,22</sup> This can be attributed to the perspective geometry of the single-plane imaging system, where the greatest uncertainty of localization lies in the out-of-plane direction, due to the insensitivity of the information available (i.e. geometric magnification).

Previous implementations of the single-plane, marker-based technique have been validated using a wide variety of methods. Most recently, Ioppolo et al.<sup>22</sup> used anatomical hip and knee models attached to micrometer-controlled positioning stages, and quantified accuracy as the difference between the applied and measured motion. They found translational accuracies of 0.1 mm in-plane, and 0.7 mm out-of-plane, and a rotational accuracy of 1° at 95% confidence (note that phantoms were static). Another study, performed by Tang et al.,<sup>23</sup> utilized cadaver knees implanted with tantalum markers, and performed kinematic measurements using both a single-plane technique and biplane RSA. They established ground truth using the measurements obtained from biplane RSA. Accuracy was assessed using the mean absolute errors between the two measurement techniques. Absolute errors were found on the range of 1 to 2 mm for translations and around 1° for rotations (again this study was performed in static conditions). Finally, Garling et al.,<sup>20</sup> made use of a rigid carbon fibre phantom containing

17 markers, which were assigned to one of two rigid-body models. The phantom was connected to a pendulum that was swung in front of an image intensifier during acquisition. They assessed accuracy as the deviation of any measurements of relative motion from zero. Translational accuracy at 95% confidence was 0.15 mm, and 1.7 mm for translation in-plane and out-of-plane, respectively. The rotational accuracy was  $0.1^\circ$ .

Imprecision or bias in determining the 3D pose of a rigid-body from a single perspective projection can arise from several different sources. These sources include any inaccuracies or errors that arise during the characterization of the rigid-body, the reconstruction of the projective geometry, and the measurement of the 2D centroids of the projected marker locations within a radiograph. Garling et al.<sup>20</sup> provide thorough simulation results showing how each of these factors can affect the accuracy of 3D localization. The main difference between our methodology and previous implementations of single-plane analysis is the use of a digital flat-panel detector (as opposed to an image intensifier), and our acquisition of images in pulsed digital radiography mode (i.e. 3 ms "stroboscopic" exposures), instead of using fluoroscopy. Both of these differences contribute to the reduced errors associated with measuring the 2D centroid locations of marker projections within a radiograph.

Flat-panel detectors offer improved image quality compared to image intensifiers,<sup>38</sup> most importantly through the lack of inherent geometric distortion.<sup>24</sup> Geometric distortion correction has been widely addressed,<sup>39-41</sup> and is a very important part of the calibration process when performing sensitive measurements with image intensifier-based radiography systems. Residual distortions after the application of correction algorithms have been reported in the range of 0.01 mm to 0.07 mm,<sup>39,42</sup>

depending on the correction scheme. It has been shown through simulations and *in vitro* experiments that when using a single-plane to localize objects in 3D, in-plane errors on this range can propagate into inaccuracies of 0.2 mm to 1.5 mm in the out-of-plane direction.<sup>20,26</sup> The results from the *in vitro* experiments performed by Garling et al. showed a significant reduction in the accuracy of measuring relative motion when using a suboptimal technique to correct for the geometric distortion.<sup>20</sup> Additionally, performing the acquisition in pulsed-radiography mode results in higher quality images. Previous work<sup>26</sup> has shown the relationship between exposure and precision of measuring 2D centroid of spherical markers within radiographs. By optimizing the exposure during acquisition the inherent noise within the acquired radiographs can be reduced. Noise reduction leads to increased precision in measuring the 2D centroid of projected marker locations, which improves the performance of localizing a rigid-body in 3D from a single-perspective projection.

Comparison of the results of the accuracy assessments performed in static (**Table 3-1**) and dynamic conditions (**Table 3-2**) show that the inaccuracies associated with the measurement technique are more greatly dominated by random errors, rather than systematic errors (i.e. measurement precision is much greater than bias). Although the bias measured in the static assessment was greater than that measured in the dynamic assessment, this can be partially attributed to the sample size of the assessment. In the static assessment a sample size of 60 was used to estimate the accuracy (bias and precision), where in the dynamic assessment a sample size of over 1000 was used. Comparison of the precision values between the two assessments show that the precision of the technique in dynamic mode was consistently lower than that in static mode.

However, for translations in-plane ( $t_x$ ,  $t_y$ ) and all rotations ( $R_x$ ,  $R_y$ ,  $R_z$ ) the difference in precision values between static and dynamic conditions is negligible (less than 10  $\mu\text{m}$  for translations, and  $0.1^\circ$  for all rotations). The largest difference between the static and dynamic assessments was observed between the precisions values for the measurement of translations in the out-of-plane direction ( $t_z$ ). However, it should be noted that in the case of the dynamic assessment, each rigid-body only contained 4 markers, where as in the static assessment each contained 8. Results from the repeatability of kinematics measurements (**Figure 3-9**) show that the precision in performing measurements in the out-of-plane direction is significantly affected by the number of markers used in the rigid body, which contributes to the larger difference between the two values.

Because single-plane analysis is most likely to be employed to study the joint kinematics of dynamic movement it becomes very important to validate the technique in dynamic conditions in order to replicate the true conditions *in vivo* as closely as possible. Dynamic motion has an impact on the assessment of accuracy by introducing motion blurring artifacts within the acquired images. Even when using a very short exposure interval, such as 3 ms, motion blurring can be introduced into the images, although it may not be detectable through simple visual inspection. Blurring artifacts introduce errors in the process of measuring the 2D centroid location of marker projections within radiographs, which will in turn degrade the performance of the 3D pose determination. The dynamic assessment of repeatability was designed to mimic the motion of a knee joint during an ascent/descent activity. The kinematics of the dynamic knee phantom (**Figure 3-8**) provides a good approximation of knee kinematics during a bending activity, as the largest range of movement was observed in flexion/extension (range ~

55°). All other rotations observed were relatively small (range  $\sim 2^\circ$ ), and all translations observed were within the range of 10 mm, with the smallest range observed in medial/lateral direction.

The results show a high repeatability in measuring both translations and rotations during an active motion (**Figure 3-9**). It was observed that the repeatability of measuring translations in-plane ( $t_x$ ,  $t_y$ ) was better than that out-of-plane ( $t_z$ ). This was expected, and can be explained by the projective geometry of the single-plane system, as mentioned above. Also, it was noted that the repeatability of measuring translations in the x-direction ( $t_x$ ) was consistently higher than in the y-direction ( $t_y$ ), even though both occur in-plane (**Figure 3-9a**). This anomaly was most probably due to the mechanical vibration of the six-axis robot, which most significantly affected the motion of the joint in the y-direction ( $t_y$ ). Further dynamic trials were performed employing a reduced robot-speed to minimize vibrations, and indeed the repeatability of measuring translations in the y-direction ( $t_y$ ) was significantly increased. Rotations were measured with a high repeatability about all axes. Tashman et al. used similar methods to analyze the repeatability of measuring joint kinematics of canine subjects using a biplane radiography technique,<sup>13</sup> reporting across-trial repeatability of measurement was 0.14 mm for translations, and  $1.0^\circ$  for rotations.

Reducing the number of markers utilized in each rigid-body (femur and tibia segments) had a significant effect on the repeatability of measuring relative translations in the out-of-plane direction. However, even when using only four markers, the repeatability of measuring translations in this direction was on average better than 0.5 mm. Although statistically significant differences were observed in the repeatability

of measuring rotations when reducing the number of markers, these differences are negligible since all rotations were measured with a repeatability of better than  $0.1^\circ$ . When comparing the curve of the relative translations in the medial/lateral ( $t_z$ ) direction (**Figure 3-8**), with the motion in the other degrees of freedom, it is evident that this curve is much less smooth, or much "noisier". This reflects the decreased sensitivity of measuring translations that occur orthogonal to the imaging plane, and suggests that some type of post processing (e.g. low-pass filtering or smoothing window technique) may have the ability to smooth the measured motion such that it more accurately reflects the true motion of the phantom. This however, is outside the scope of the study and will have to be left for future work.

The registration of CT data to the kinematic measures shows the applicability of the single-plane technique towards various other research and clinical goals, beyond the measurement of kinematics. Knowledge of the relative positions of the joint surfaces throughout a dynamic test of its function allows the estimation of the joint space and contact patterns over time.<sup>43,44</sup> Changes in joint space and contact patterns can be used to quantify the progression of diseases, such as osteoarthritis.<sup>43</sup> Progressive narrowing of joint space, due to osteoarthritis, has been recommended as an indicator for 'failure' of a secondary outcome in clinical trials for osteoarthritis of the hip and knee.<sup>45</sup>

Often in biomechanics, *in vivo* data, such as geometries derived from CT, kinematics, and kinetics, are used to build and validate finite element models of joints.<sup>46,47</sup> Biomechanical modeling of joints can be used to study their normal function, as well as the function of joints following corrective surgery, such as posterior cruciate ligament reconstruction,<sup>48</sup> or total knee replacement.<sup>49</sup> By combining kinematic measurements

determined from single-perspective projection, with kinetic measurements obtained from force plates, it is possible to dynamically measure the mechanics of joints.<sup>50</sup> This kind of information is invaluable from a biomechanics aspect, as it can lead to a better understanding of both normal and pathological joint mechanics. A better understanding of joint mechanics can improve treatment strategies, and also joint replacement designs and longevity.<sup>50</sup>

Visualization of the joint kinematics derived from the single-perspective projections aides in interpretation of the measured motion. Often, it is difficult to visualize or interpret the motion of the joint directly from the kinematic plots (**Figure 3-8**). By constructing a 3D virtual environment to recreate the six DOF motion, it is possible to directly view the kinematics acting upon a 3D model. Previous studies have explored visualization techniques to animate the motion of carpal joints for the purposes of biomechanics modeling.<sup>51</sup>

It is important to note, that although the initial rigid-body model of the markers implanted into the knee model was obtained through an RSA examination, it is also possible to generate this local coordinate system directly from a CT volume. However, since RSA is considered the de facto *gold standard* for obtaining accurate measurements of markers implanted into skeletal segments,<sup>52</sup> it was deemed best-suited to generate the rigid-body model used with the accuracy assessments. Previous work performed by Garling et al.,<sup>20</sup> has shown that errors present within the rigid-body model negatively effects the accuracy of single-plane localization. The RMS FRE of the registration between corresponding point-based models generated from RSA, and micro-CT was 0.1 mm. This suggests that discrepancies (i.e. errors in measurement) exist between the

two characterization methods, which warrant further investigations to determine the relationship between the methods used to characterize the rigid body, and the accuracy of 3D measurements determined from single-perspective projections.

The effective dose of radiation for a dynamic assessment of a knee was estimated to be less than 3  $\mu\text{Sv}$  (equivalent to 0.01  $\mu\text{Sv}$  per frame). A baseline RSA knee examination is also required to establish a local coordinate system describing the relative locations of the markers. The effective dose associated with this procedures is typically around 1  $\mu\text{Sv}$ .<sup>32</sup> This can be compared to the effective dose of 50  $\mu\text{Sv}$  associated with a standard chest x-ray,<sup>53</sup> and the effective whole body dose of 3000  $\mu\text{Sv}$  associated with annual natural background exposure. Therefore, the risk to human subjects would be considered minimal, and it is expected that ethics approval could be obtained to employ the procedure of dynamically measuring joint kinematics from single-perspective projections within *in vivo* studies.

### 3.5 Conclusions

This study has demonstrated the accuracy and safety of the application of single-plane radiographic imaging to dynamically measure joint kinematics, as well as the suitability of digital flat-panel radiography system for use in this application. The flat-panel detector design offers a number of improvements over image intensifiers, which increases the accuracy of measurement and the ease of implementation. The poorest performance in measurement was observed in the out-of-plane direction, however measurement accuracy was still better than 0.5 mm, which is suitable for most medical tracking applications. The effective dose of ionizing radiation that would be imparted in a clinical examination during the acquisition of a dynamic sequence of images was estimated to be significantly lower when compared to other standard radiological examinations. This measurement technique is valuable for numerous research and clinical applications, beyond the measurement of kinematics, including: dynamic estimation of joint space or contact area, biomechanics modeling, and visualization.

### 3.6 References

1. Hanson GR, Park SE, Suggs JF, Moynihan AL, Nha KW, Freiberg AA, Li G. 2007. In vivo kneeling biomechanics after posterior stabilized total knee arthroplasty. *J Orthop Sci* 12: 476-483.
2. Suggs JF, Kwon YM, Durbhakula SM, Hanson GR, Li G. 2008. In vivo flexion and kinematics of the knee after TKA: comparison of a conventional and a high flexion cruciate-retaining TKA design. *Knee Surg Sports Traumatol Arthrosc*.
3. Defrate LE, Papannagari R, Gill TJ, Moses JM, Pathare NP, Li G. 2006. The 6 degrees of freedom kinematics of the knee after anterior cruciate ligament deficiency: an in vivo imaging analysis. *Am J Sports Med* 34: 1240-1246.
4. Bey MJ, Kline SK, Tashman S, Zauel R. 2008. Accuracy of biplane x-ray imaging combined with model-based tracking for measuring in-vivo patellofemoral joint motion. *J Orthop Surg* 3: 38.
5. von Porat A, Roos EM, Roos H. 2004. High prevalence of osteoarthritis 14 years after an anterior cruciate ligament tear in male soccer players: a study of radiographic and patient relevant outcomes. *Ann Rheum Dis* 63: 269-273.
6. Kannus P, Jarvinen M. 1989. Posttraumatic anterior cruciate ligament insufficiency as a cause of osteoarthritis in a knee joint. *Clin Rheumatol* 8: 251-260.
7. Leardini A, Chiari L, Della Croce U, Cappozzo A. 2005. Human movement analysis using stereophotogrammetry. Part 3. Soft tissue artifact assessment and compensation. *Gait Posture* 21: 212-225.
8. Benoit DL, Ramsey DK, Lamontagne M, Xu L, Wretenberg P, Renstrom P. 2006. Effect of skin movement artifact on knee kinematics during gait and cutting motions measured in vivo. *Gait Posture* 24: 152-164.
9. Ramsey DK, Lamontagne M, Wretenberg PF, Valentin A, Engstrom B, Nemeth G. 2001. Assessment of functional knee bracing: an in vivo three-dimensional kinematic analysis of the anterior cruciate deficient knee. *Clin Biomech (Bristol, Avon)* 16: 61-70.
10. Sheehan FT, Zajac FE, Drace JE. 1998. Using cine phase contrast magnetic resonance imaging to non-invasively study in vivo knee dynamics. *J Biomech* 31: 21-26.
11. Barrance PJ, Williams GN, Snyder-Mackler L, Buchanan TS. 2006. Altered knee kinematics in ACL-deficient non-copers: a comparison using dynamic MRI. *J Orthop Res* 24: 132-140.

12. Draper CE, Santos JM, Kourtis LC, Besier TF, Fredericson M, Beaupre GS, Gold GE, Delp SL. 2008. Feasibility of using real-time MRI to measure joint kinematics in 1.5T and open-bore 0.5T systems. *J Magn Reson Imaging* 28: 158-166.
13. Tashman S, Anderst W. 2003. In-vivo measurement of dynamic joint motion using high speed biplane radiography and CT: application to canine ACL deficiency. *J Biomech Eng* 125: 238-245.
14. Li G, Van de Velde SK, Bingham JT. 2008. Validation of a non-invasive fluoroscopic imaging technique for the measurement of dynamic knee joint motion. *J Biomech* 41: 1616-1622.
15. Ramsey DK, Wretenberg PF, Benoit DL, Lamontagne M, Nemeth G. 2003. Methodological concerns using intra-cortical pins to measure tibiofemoral kinematics. *Knee Surg Sports Traumatol Arthrosc* 11: 344-349.
16. Patel VV, Hall K, Ries M, Lotz J, Ozhinsky E, Lindsey C, Lu Y, Majumdar S. 2004. A three-dimensional MRI analysis of knee kinematics. *J Orthop Res* 22: 283-292.
17. Banks SA, Hodge WA. 1996. Accurate measurement of three-dimensional knee replacement kinematics using single-plane fluoroscopy. *IEEE Trans Biomed Eng* 43: 638-649.
18. Hoff WA, Komistek RD, Dennis DA, Gabriel SM, Walker SA. 1998. Three-dimensional determination of femoral-tibial contact positions under in vivo conditions using fluoroscopy. *Clin Biomech (Bristol, Avon)* 13: 455-472.
19. Yuan X, Ryd L, Tanner KE, Lidgren L. 2002. Roentgen single-plane photogrammetric analysis (RSPA.) A new approach to the study of musculoskeletal movement. *J Bone Joint Surg Br* 84: 908-914.
20. Garling EH, Kaptein BL, Geleijns K, Nelissen RG, Valstar ER. 2005. Marker Configuration Model-Based Roentgen Fluoroscopic Analysis. *J Biomech* 38: 893-901.
21. Selvik G. 1990. Roentgen stereophotogrammetric analysis. *Acta Radiol* 31: 113-126.
22. Ioppolo J, Borlin N, Bragdon C, Li M, Price R, Wood D, Malchau H, Nivbrant B. 2007. Validation of a low-dose hybrid RSA and fluoroscopy technique: Determination of accuracy, bias and precision. *J Biomech* 40: 686-692.
23. Tang TS, MacIntyre NJ, Gill HS, Fellows RA, Hill NA, Wilson DR, Ellis RE. 2004. Accurate assessment of patellar tracking using fiducial and intensity-based fluoroscopic techniques. *Med Image Anal* 8: 343-351.

24. Cowen AR, Davies AG, Sivananthan MU. 2008. The design and imaging characteristics of dynamic, solid-state, flat-panel x-ray image detectors for digital fluoroscopy and fluorography. *Clin Radiol* 63: 1073-1085.
25. Hoffmann KR, Esthappen J. 1997. Determination of three-dimensional positions of known sparse objects from a single projection. *Med Phys* 24: 555-564.
26. Habets DF, Pollmann SI, Yuan X, Peters TM, Holdsworth DW. 2009. Error analysis of marker-based object localization using a single-plane XRII. *Med Phys* 36: 190-200.
27. Tashman S, Kolowich P, Collon D, Anderson K, Anderst W. 2007. Dynamic function of the ACL-reconstructed knee during running. *Clin Orthop Relat Res* 454: 66-73.
28. Soderkvist I, Wedin PA. 1993. Determining the movements of the skeleton using well-configured markers. *J Biomech* 26: 1473-1477.
29. Ranstam J, Ryd L, Onsten I. 2000. Accurate accuracy assessment: review of basic principles. *Acta Orthop Scand* 71: 106-108.
30. Schonemann PH. 1966. A generalized solution of the orthogonal procrustes problem. *Psychometrika* 31.
31. Schroeder W, Martin K, Lorensen B. 2002. The visualization toolkit: an object-oriented approach to 3D graphics. Kitware, Inc.
32. Okkalides D, Fotakis M. 1994. Patient effective dose resulting from radiographic examinations. *Br J Radiol* 67: 564-572.
33. Cappozzo A, Catani F, Croce UD, Leardini A. 1995. Position and orientation in space of bones during movement: anatomical frame definition and determination. *Clin Biomech (Bristol, Avon)* 10: 171-178.
34. Hagemester N, Parent G, Van de Putte M, St-Onge N, Duval N, de Guise J. 2005. A reproducible method for studying three-dimensional knee kinematics. *J Biomech* 38: 1926-1931.
35. Della Croce U, Leardini A, Chiari L, Cappozzo A. 2005. Human movement analysis using stereophotogrammetry. Part 4: assessment of anatomical landmark misplacement and its effects on joint kinematics. *Gait Posture* 21: 226-237.
36. Victor J, Van Doninck D, Labey L, Innocenti B, Parizel PM, Bellemans J. 2009. How precise can bony landmarks be determined on a CT scan of the knee? *Knee*.
37. Fitzpatrick JM, West JB, Maurer CR, Jr. 1998. Predicting error in rigid-body point-based registration. *Medical Imaging, IEEE Transactions on* 17: 694-702.

38. Bogaert E, Bacher K, Lapere R, Thierens H. 2008. Does digital flat detector technology tip the scale towards better image quality or reduced patient dose in interventional cardiology? *Eur J Radiol*.
39. Fahrig R, Moreau M, Holdsworth DW. 1997. Three-dimensional computed tomographic reconstruction using a C-arm mounted XRII: correction of image intensifier distortion. *Med Phys* 24: 1097-1106.
40. Liu RR, Rudin S, Bednarek DR. 1999. Super-global distortion correction for a rotational C-arm x-ray image intensifier. *Med Phys* 26: 1802-1810.
41. Gutierrez LF, Ozturk C, McVeigh ER, Lederman RJ. 2008. A practical global distortion correction method for an image intensifier based x-ray fluoroscopy system. *Med Phys* 35: 997-1007.
42. Gronenschild E. 1997. The accuracy and reproducibility of a global method to correct for geometric image distortion in the x-ray imaging chain. *Med Phys* 24: 1875-1888.
43. Anderst WJ, Tashman S. 2003. A method to estimate in vivo dynamic articular surface interaction. *J Biomech* 36: 1291-1299.
44. Marai GE, Laidlaw DH, Demiralp C, Andrews S, Grimm CM, Crisco JJ. 2004. Estimating joint contact areas and ligament lengths from bone kinematics and surfaces. *IEEE Trans Biomed Eng* 51: 790-799.
45. Altman RD, Abadie E, Avouac B, Bouvenot G, Branco J, Bruyere O, Calvo G, Devogelaer JP, Dreiser RL, Herrero-Beaumont G, Kahan A, Kreutz G, Laslop A, Lemmel EM, Menkes CJ, Pavelka K, Van De Putte L, Vanhaelst L, Reginster JY, Group for Respect of E, Ethics in S. 2005. Total joint replacement of hip or knee as an outcome measure for structure modifying trials in osteoarthritis. *Osteoarthritis Cartilage* 13: 13-19.
46. Donahue TL, Hull ML, Rashid MM, Jacobs CR. 2002. A finite element model of the human knee joint for the study of tibio-femoral contact. *J Biomech Eng* 124: 273-280.
47. Gray HA, Taddei F, Zavatsky AB, Cristofolini L, Gill HS. 2008. Experimental validation of a finite element model of a human cadaveric tibia. *J Biomech Eng* 130: 031016.
48. Ramaniraka NA, Terrier A, Theumann N, Siegrist O. 2005. Effects of the posterior cruciate ligament reconstruction on the biomechanics of the knee joint: a finite element analysis. *Clin Biomech (Bristol, Avon)* 20: 434-442.
49. Perillo-Marcone A, Taylor M. 2007. Effect of varus/valgus malalignment on bone strains in the proximal tibia after TKR: an explicit finite element study. *J Biomech Eng* 129: 1-11.

50. Zihlmann MS, Gerber H, Stacoff A, Burckhardt K, Szekely G, Stussi E. 2006. Three-dimensional kinematics and kinetics of total knee arthroplasty during level walking using single plane video-fluoroscopy and force plates: a pilot study. *Gait Posture* 24: 475-481.
51. Green JK, Werner FW, Wang H, Weiner MM, Sacks JM, Short WH. 2004. Three-dimensional modeling and animation of two carpal bones: a technique. *J Biomech* 37: 757-762.
52. Karrholm J. 1989. Roentgen stereophotogrammetry. Review of orthopedic applications. *Acta Orthop Scand* 60: 491-503.
53. Mettler FA, Jr., Huda W, Yoshizumi TT, Mahesh M. 2008. Effective doses in radiology and diagnostic nuclear medicine: a catalog. *Radiology* 248: 254-263.

## 4 Summary and Future Directions

The overall objective of this thesis was the development and validation of novel and dynamic radiographic imaging and registration techniques to address two distinct medical applications: tracking during image-guided interventions, and the measurement of musculoskeletal joint kinematics. The following sections summarize the main findings of the thesis (section §4.1), and identify key areas of research for future work, as well as address its clinical application (section §4.2).

### 4.1 Summary and Conclusions

#### 4.1.1 Sparse Object Tracking towards Image-guided Interventions

This study was specifically designed to facilitate the clinical application of image-guidance for interventional procedures, and its main objective was to assess the feasibility of using single-perspective projections to track surgical objects in 3D space during an intervention. Several *in vitro* validation studies were performed to evaluate the accuracy of tracking sparse object in 3D space from single-perspective, 2D projections, and test the software implementation that enabled this application. Secondary objectives of the study

were the comparison of two digital radiography systems, one equipped with an XRII and the other with a FP detector, towards the tracking task.

The first validation study was performed in static conditions, and employed two phantoms: a regular grid of divots of known geometry, and a sparse object manufactured to mimic a pointer tool. Targets upon the grid (i.e. divots) were localized in 3D using the sparse pointer tool and single-perspective projections. Accuracy was quantified using the RMS TRE, of the registration between the measured locations of the targets upon the grid, and its known geometry as given by its CAD model, while precision was quantified using the standard deviation of repeated measurements. The assessment was performed on two digital radiography systems (XRII and FP) using multiple acquisition views (AP and LAO), employing an OTS to provide a *gold standard* for comparison. The results of the assessment showed that measurements made using the radiography system equipped with a FP detector outperformed those made with the XRII. The accuracy and precision of localizing targets in 3D with the sparse object was better than 1.1 mm and 0.16 mm respectively, when utilizing the FP detector for image acquisition. The OTS had the best performance, as expected, which highlighted the benefits of localization from two views, as opposed to one.

The second validation study was performed under dynamic conditions and again utilized two phantoms: the sparse pointer tool, and an anatomical skull implanted with tungsten markers. The sparse pointer tool was tracked simultaneously using both single-perspective projections, and an OTS as it was used to localize several targets within the skull. Tracking accuracy was assessed using the RMS difference in the trajectory of the pointer tool, as measured using both the single-perspective projections and the OTS. The

RMS tracking error was 2.1 mm. The sequence of projections acquired during the dynamic validation study also served as a robust test of the implemented software. The software was able to successfully track the sparse pointer tool from 96% of the acquired projections, and successfully track the anatomical skull from 100% of the acquired projections. The software achieved a throughput of approximately 4 frames per second. With further optimization and implementation on dedicated hardware, it would be possible to achieve real-time execution.

These studies demonstrated the feasibility of using single-perspective projections during an intervention for 3D tracking and localization of surgical objects. The accuracy of target localization and tracking are applicable for numerous image-guided applications. The main limitation of this tracking technique is the decreased accuracy in the measurement of the out-of-plane translation or position. However, since this limitation is well known, and affects only a single DOF, it can be overcome with careful methodological considerations, such as pre-procedural planning and equipment setup to limit the reliance on out-of-plane measurements.

#### 4.1.2 Measurement of Joint Kinematics

The main objective of the second study was to validate the technique of measuring joint kinematics from single-perspective projections. Several *in vitro* validation experiments were performed to assess the accuracy of measuring joint kinematics in six DOF from single-perspective projections, and estimate the effective dose of ionizing radiation that would be associated with the measurement procedure. Secondary objectives of the study included demonstration of the suitability of using FP detector

technology to perform the single-plane measurements, and registration of 3D CT data to the single-perspective projections and kinematics measurements.

The first experiment made use of a static phantom that incorporated an anatomical knee model, implanted with tungsten markers, and a three-axis positioning stage. Known displacements were applied to the positioning stage to move the anatomical knee model, and subsequently measured from single-perspective projections. Accuracy was assessed using differences between the measured and applied motion. The measurement accuracy was found to be better than 0.5 mm, and  $0.1^\circ$  at the 95% prediction interval for translations and rotations, respectively.

The second experiment employed a dynamic phantom that incorporated a six-axis articulated robot, and the anatomical knee model implanted with the tantalum markers. The robot was programmed to apply a flexion-extension motion to the knee model. Six repeated cine acquisitions of the moving phantom were acquired to perform several assessments. The first assessed accuracy by defining two rigid bodies from the markers implanted into the femur segment of the knee model. The motion between the two rigid-bodies was measured from the acquired projection sequences, and accuracy was assessed using the deviation of the measured motion from zero. The measurement accuracy was found to be better than 0.9 mm, and  $0.1^\circ$  at the 95% prediction interval for translations and rotations, respectively. The second assessment determined the repeatability of kinematic measurements. The motion between tibia the femur segment of the knee model was measured from the acquired projections sequences. The repeatability of kinematic measurements was assessed using the variability of the measured motion across each of the six trials in each kinematic DOF. The repeatability of kinematic measurements was

better than  $\pm 0.2$  mm and  $\pm 0.1^\circ$  for translations and rotations, respectively. The third assessment examined the effect of reduced visibility of markers on the measurement repeatability. The acquired projection sequences were re-processed using a two reduced sets of markers to measure the kinematics of the joint. It was found that reducing the number of makers had a significant affect on the measurement of translation in the out-of-plane direction. Measurements in all other DOF (i.e. in-plane translations and all rotations) were robust to reducing the number of markers.

The effective dose of ionizing radiation associated with the dynamic measurement procedure was determined using an ion chamber and a digital dosimeter. The effective dose of the procedure was estimated to be less than  $3 \mu\text{Sv}$  for an approximately 180-frame acquisition, which would be considered as a minimal risk to human subjects, and therefore acceptable for application *in vivo*.

This study validated the technique used to measure joint kinematics from single-perspective projections, and demonstrated the suitability of FP detectors for this task. The accuracy of measurement, and the effective dose of ionizing radiation are viable for numerous clinical applications. Again, the main limitation of the technique is the decreased accuracy of measuring translations in the out-of-plane direction. However, the accuracy achieved in the out-of-plane directions is sufficient for the intended application (i.e. measurement of joint kinematics).

## 4.2 Future Directions

### 4.2.1 Sparse Object Tracking towards Image-guided Interventions

#### *Future Work*

The next progression of this work is the continued development of the software such that it can be useable in the clinic. However, to achieve this goal several issues must be addressed. The first involves fully automating the algorithm so that it does not require any user interaction or input. Currently the user must establish correspondence between the markers in the sparse object and their projections within the acquired radiographs. This process should be automated to render the technique suitable for real-time tracking applications. Correspondence between point-sets is an issue that has been widely addressed in machine vision,<sup>1-3</sup> and is also a problem that has been addressed in current OTS.<sup>4</sup>

The second issue involves implementation of the software on dedicated hardware. This includes optimizing and parallelizing the algorithm to increase its processing speed, and also implementing a frame-grabber module such that the acquired projections can be processed in real-time as they are acquired by the radiography system. During the reported studies, images were acquired on the radiography system, and then transferred to a personal computer for all subsequent processing steps.

Finally, the design of the sparse object (i.e. geometry, marker placement, and size) should be optimized for intended application. The sparse object employed during the study was a simple phantom manufactured to mimic a generic pointer tool, and to

demonstrate the ability to localize very compact and sparsely distributed markers. However, specific clinical applications will require specialized sparse objects that must be carefully designed to ensure they meet accuracy requirements, and are robust. Additional assessments must also be performed to characterize the accuracy with which newly designed sparse objects can be localized and tracked, since the accuracy is dependant on the design. These same principles apply to OTS and any specialized optical tracking frames that are designed for image-guided applications.<sup>5</sup>

### *Clinical Applications*

With further refinement and optimization, the technique of tracking sparse objects from single-perspective projections has the potential to be used within the clinic during interventional procedures. While this is a very broad category, several specific clinical interventions have been preemptively examined for potential application of this technique. One potential clinical application is in spinal surgery. Insertion of pedicle screws into the spine is an interventional procedure that commonly relies on fluoroscopy for image-guidance.<sup>6</sup> Numerous studies have concluded that 3D image-guidance improves the safety and accuracy of spinal interventions.<sup>7-9</sup> The fluoroscopic acquisitions that are commonly performed during this interventional procedure could be further utilized to provide 3D image-guidance, provided a sparse tool or device is incorporated into the intervention.

Another potential clinical application is in cardiac surgery. A novel, emerging technique for cardiac valve repair and replacement uses a transcatheter approach.<sup>10</sup> Often image-guidance during the procedure is provided through a combination of fluoroscopy

and transesophageal echocardiography (TEE).<sup>11,12</sup> This combination is used because of the strengths and limitations of each imaging modality. Fluoroscopy can provide excellent delineation of the catheter, but has poor soft tissue contrast, where as ultrasound can provide excellent soft-tissue contrast, but poor visualization of the catheter. Currently, there is no way to fuse or register these two imaging modalities into a common coordinate system. OTS cannot be utilized because the lack of line-of-sight, and EMTS are unreliable because of the presence of the fluoroscopy unit.<sup>13</sup> By designing a sparse rigid-body that can be incorporated into the ultrasound probe, registration of these two imaging modalities could be achieved. This would facilitate fusion of the images from the two modalities, and also provide a form of 3D guidance.

#### 4.2.2 Measurement of Joint Kinematics

##### *Future Work*

The study has shown that the technique of measuring joint kinematics from single-perspective projections is ready for use within the clinic. However, to optimize some aspects of the procedure, and gain a deeper understanding of some of its limiting factors, several additional studies should be performed. The first involves understanding the relationship between the characterization process used to establish the local coordinate system, describing the relative location of the implanted markers, and the accuracy of the corresponding kinematic measurements. Previous computer simulations have noted the negative effects of errors on measurement accuracy during the characterization process.<sup>14</sup> In the validation studies performed in this thesis, the local coordinate system was generated through an RSA examination (**Figure 4-1a,b**), which is considered the *gold*

*standard* for this task.<sup>15</sup> However, in some applications, acquisition of a CT scan is also a requirement.<sup>16</sup> Therefore, it should be determined whether the accuracy of kinematic measurements, determined using the relative marker locations characterized from an acquired CT (**Figure 4-1c,d**), is sufficiently high for clinical use. Some of the ultimate factors affecting accuracy of the CT characterization process include the voxel spacing, reconstructed resolution, and the algorithms used to segment and measure the marker locations within the CT volume.



**Figure 4-1:** Several methods can be used to characterize the relative locations of the markers implanted into the joint, including: a radiostereometric analysis (RSA) examination, acquisition of a micro-computed tomography (microCT) scan, and acquisition of a clinical CT scan. a) and b) show stereo images of a knee phantom, implanted with tantalum markers, acquired during a RSA examination. c) and d) show maximum intensity projections (MIPs) of a micro-CT and CT scan, respectively of the same knee phantom. Note the bean-like shape of the markers within the CT volume (d); an image artefact due to the anisotropic voxel spacing of the CT volume.

The second study should determine optimized sampling rates (i.e. fps of acquisition) with which to measure the kinematics of joints moving at various speeds. Previous studies employing radiological-based techniques to measure joint kinematics have employed sampling rates ranging from 25 fps,<sup>17</sup> all the way up to 250 fps.<sup>18</sup> The problem is further compounded by the relationship between the sampling rate and x-ray pulse width, which differs during pulsed, synchronous acquisition, and continuous

acquisition. All of these factors must be examined in order to determine the optimized sampling rates. This is important because these factors affect the resulting dose of ionizing radiation associated with the measurement procedure, and also are a limiting factor of the overall accuracy of the measurements.

Finally, the process involved in determining the projective parameters of radiography system should be further refined. This process is a very important step of the overall measurement technique, and is accomplished through the use of a calibration cage. In the validation studies performed, the perspective geometry of the radiography system was determined using a commercial calibration cage manufactured specifically for RSA examinations of the knee. Previous work has shown improvements in the accuracy of RSA measurements by optimizing the design of the calibration cage used to determine the perspective parameters of the radiography systems.<sup>19</sup> By designing a calibration cage specifically for the task at hand (i.e. measurement of kinematics from single-perspective projections), it is possible to improve accuracy of the calibration procedure, which would lead to an improvement in the accuracy of the overall kinematic measurements.<sup>14</sup>

### *Clinical Application*

The obvious application of this work is the measurement of joint kinematics *in vivo*. Measurement of kinematics is very important in understanding both normal joint function, and also pathologies associated with musculoskeletal disorder and trauma.<sup>20</sup> Additionally, this measurement tool can be used to aid in quantifying the outcomes of interventional procedures and therapy, and also aide in the design of new joint implants that better mimic physiological conditions.<sup>21</sup> One limit to clinical application of this work

is the need for tantalum markers to be implanted into skeletal segments of the joint interested in being examined. Since this procedure is invasive, the technique may be restricted to studying subjects that are currently undergoing surgery, where the implantation procedure can easily be incorporated into a pre-existing plan of intervention.

One of the significant contributions of this work is that it demonstrated the ease of implementation of the measurement technique using clinically available FP detector technology. Since current trends point towards FP detectors eventually replacing XRIIs altogether, this measurement technique has the potential to be implemented in any clinic with access to this growing technology. This is an important factor, since previous work in the area of measuring joint kinematics has relied on highly specialized equipment that is not commonly available in the typically clinical or hospital setting.<sup>18,22</sup>

### 4.3 References

1. Scott GL, Longuet-Higgins HC. 1991. An algorithm for associating the features of two images. *Proc Biol Sci* 244: 21-26.
2. Pilu M. 1997. Direct method for stereo correspondence based on singular value decomposition. In. San Juan, PR, USA: IEEE, pp. 261-266.
3. Bai X, Yu H, Hancock ER. 2004. Graph matching using spectral embedding and alignment. In. Cambridge, United kingdom: Institute of Electrical and Electronics Engineers Inc., pp. 398-401.
4. Hornung A, Sar-Dessai S, Kobbelt L. 2005. Self-calibrating optical motion tracking for articulated bodies. In. Bonn, Germany: Institute of Electrical and Electronics Engineers Computer Society, pp. 75-82.
5. West JB, Maurer CR, Jr. 2004. Designing optically track instruments for image-guided surgery. *Medical Imaging, IEEE Transactions on* 23: 533-545.
6. Holly LT, Foley KT. 2007. Image guidance in spine surgery. *Orthop Clin North Am* 38: 451-461; abstract viii.
7. Ondra SL, Marzouk S, Ganju A, Morrison T, Koski T. 2006. Safety and efficacy of C2 pedicle screws placed with anatomic and lateral C-arm guidance. *Spine* 31: E263-267.
8. Marshman LA, Friesem T, Rampersaud YR, Le Huec JC, Krishna M, Reddy GR. 2007. Significantly improved lumbar arthroplasty placement using image guidance: technical note. *Spine* 32: 2027-2030.
9. Nottmeier EW, Seemer W, Young PM. 2009. Placement of thoracolumbar pedicle screws using three-dimensional image guidance: experience in a large patient cohort. *J Neurosurg Spine* 10: 33-39.
10. Webb JG, Altwegg L, Boone RH, Cheung A, Ye J, Lichtenstein S, Lee M, Masson JB, Thompson C, Moss R, Carere R, Munt B, Nietlispach F, Humphries K. 2009. Transcatheter Aortic Valve Implantation. Impact on Clinical and Valve-Related Outcomes. *Circulation*.
11. Naqvi TZ, Buchbinder M, Zarbatany D, Logan J, Molloy M, Balke G, Ainsworth R, Webb JG, Alfieri O, Maisano F. 2007. Beating-heart percutaneous mitral valve repair using a transcatheter endovascular suturing device in an animal model. *Catheter Cardiovasc Interv* 69: 525-531.
12. Moss RR, Ivens E, Pasupati S, Humphries K, Thompson CR, Munt B, Sinhal A, Webb JG. 2008. Role of echocardiography in percutaneous aortic valve implantation. *JACC Cardiovasc Imaging* 1: 15-24.

13. Hummel J, Figl M, Kollmann C, Bergmann H, Birkfellner W. 2002. Evaluation of a miniature electromagnetic position tracker. *Med Phys* 29: 2205-2212.
14. Garling EH, Kaptein BL, Geleijns K, Nelissen RG, Valstar ER. 2005. Marker Configuration Model-Based Roentgen Fluoroscopic Analysis. *J Biomech* 38: 893-901.
15. Karrholm J. 1989. Roentgen stereophotogrammetry. Review of orthopedic applications. *Acta Orthop Scand* 60: 491-503.
16. Anderst WJ, Tashman S. 2003. A method to estimate in vivo dynamic articular surface interaction. *J Biomech* 36: 1291-1299.
17. Zihlmann MS, Gerber H, Stacoff A, Burckhardt K, Szekely G, Stussi E. 2006. Three-dimensional kinematics and kinetics of total knee arthroplasty during level walking using single plane video-fluoroscopy and force plates: a pilot study. *Gait Posture* 24: 475-481.
18. Tashman S, Anderst W. 2003. In-vivo measurement of dynamic joint motion using high speed biplane radiography and CT: application to canine ACL deficiency. *J Biomech Eng* 125: 238-245.
19. Cai R, Yuan X, Rorabeck C, Bourne RB, Holdsworth DW. 2008. Development of an RSA calibration system with improved accuracy and precision. *J Biomech* 41: 907-911.
20. Defrate LE, Papannagari R, Gill TJ, Moses JM, Pathare NP, Li G. 2006. The 6 degrees of freedom kinematics of the knee after anterior cruciate ligament deficiency: an in vivo imaging analysis. *Am J Sports Med* 34: 1240-1246.
21. Suggs JF, Kwon YM, Durbhakula SM, Hanson GR, Li G. 2008. In vivo flexion and kinematics of the knee after TKA: comparison of a conventional and a high flexion cruciate-retaining TKA design. *Knee Surg Sports Traumatol Arthrosc*.
22. Anderst W, Zauel R, Bishop J, Demps E, Tashman S. 2008. Validation of three-dimensional model-based tibio-femoral tracking during running. *Med Eng Phys*.